UNIVERSITÄT
DES
SAARLANDES

Modeling and Self-Sensing of Soft Robotic Structures based on Dielectric Elastomers

Dissertation

zur Erlangung des Grades
des Doktors der Ingenieurwissenschaften
der Naturwissenschaftlich-Technischen Fakultät
der Universität des Saarlandes

von

Johannes Marcus Prechtl

Saarbrücken
2025

Tag des Kolloquiums: 26.03.2026

Dekan:	Prof. Dr.-Ing. Dirk Bähre
Berichterstatter:	Prof. Dr. Gianluca Rizzello Prof. Dr.-Ing. Matthias Nienhaus
Vorsitz:	Prof. Dr.-Ing. Georg Frey
Akad. Mitglied:	Dr.-Ing. Daniel Bruch

We shall see what we shall see. We have the start now; the developments will follow in time.

- W. C. Röntgen

Acknowledgements

I am deeply grateful to my mentor and doctoral supervisor Jun.-Prof. Dr. Gianluca Rizzello, for the opportunity to work on this topic and for his constant guidance and moral support during my PhD journey. I would also like to thank Prof. Dr.-Ing. Stefan Seelecke and Prof. Dr.-Ing. Paul Motzki, for creating a fruitful research environment at the Intelligent Material Systems Lab (iMSL) and for the good scientific collaboration during my time there. I am also grateful to Prof. Dr. Kathrin Flaßkamp, for the opportunity to work at the Chair of Systems Modeling and Simulation (SMS) and for her scientific mentorship.

Furthermore, I gratefully acknowledge the financial support of the Deutsche Forschungsgemeinschaft (DFG), who funded the starting phase of my PhD work through priority program SPP 2100 "Soft Material Robotic Systems" (Project: RI3030/1-1).

This work would not have been possible without my project collaborators. Specifically, I would like to acknowledge the contributions of Julian Kunze, who performed the manufacturing of RDEA specimens, conducted tensile tests and performed capacitance measurements. Furthermore, I recognize the contributions of Giacomo Moretti and Daniel Bruch, who provided valuable insights and helped to refine assumptions and argumentation. I also wish to thank Matthias Baltes for his work in building the physical T-Platform prototypes and performing characterization experiments. Thank you all for a cherished time spent together in the lab and the good discussions, both during our formal meetings and in the lab kitchen.

On a similar note, big thanks, professionally and personally, belong to my former colleagues at iMSL and at SMS, for the good discussions, for their advice and for their friendship. Finally, I want to thank the people in my personal life: my girlfriend Lisa, my friends and my family – for the spirited discussions at dinnertime, for their patience, encouragement and never-ending support.

Abstract

In recent years, soft robots have seen growing interest, as new challenges are increasingly difficult to resolve with rigid robots. Truly soft robots require different actuators, sensors and algorithms and can thus benefit from the intrinsically soft Dielectric Elastomers (DEs), which can operate as actuators and sensors simultaneously. Therefore, this work unites the fields of DE and soft robotics research, by developing models and algorithms for DE-based soft robots.

The first part of this dissertation introduces a physics-based model for rolled DE actuators (RDEAs), which in soft robots could serve as artificial muscle fibres that elongate and contract depending on electrical voltage. The model accurately predicts the actuator force at given voltage and length while considering material properties and actuator geometry.

In the second part, a physical model of a soft robotic system based on RDEAs (named "T-Platform") is developed. Its bistability property is investigated in depth and utilized for increased actuation performance. It is shown in experiments that the static and dynamic behaviour under the influence of physical parameters is accurately captured.

The third part is dedicated to a system-level self-sensing algorithm for the T-Platform. By estimating the RDEA lengths through electrical measurements during actuation and considering the physics-based RDEA model, a state observer is derived, showing robust and accurate state estimates of physical prototypes.

Kurzfassung

Seit längerem erfahren weiche Roboter zunehmende Aufmerksamkeit, da neue Herausforderungen mit starren Robotern immer schwieriger zu bewältigen sind. Sie erfordern andere Aktoren, Sensoren und Algorithmen und können daher von den vollständig weichen Dielektrische Elastomeren (DEs) profitieren, welche gleichzeitig als Aktuatoren und Sensoren fungieren können. Diese Arbeit vereint daher die Forschungsfelder der DEs und der Soft-Robotik durch die Entwicklung von Modellen und Algorithmen für Soft-Roboter auf DE-Basis.

Der erste Teil führt ein Modell für gerollte DE-Aktoren (RDEAs) ein, welche sich in Abhängigkeit von einer elektrischen Spannung ausdehnen und kontrahieren. Das Modell sagt die Aktuatorkraft in Abhängigkeit der Spannung und der Aktuatorlänge unter Berücksichtigung von Materialeigenschaften und Aktuatorgeometrie präzise voraus.

Im zweiten Teil wird ein Modell eines weichen Robotersystems mit RDEAs (genannt „T-Plattform“) entwickelt. Die Bistabilität des Systems wird eingehend untersucht und zur Steigerung der Aktuationsleistung genutzt. Es wird experimentell gezeigt, dass das Systemverhalten unter dem Einfluss von physikalischen Parametern korrekt erfasst wird.

Der dritte und letzte Teil widmet sich einem Selfsensing-Algorithmus für die T-Plattform. Durch Längenschätzung der RDEAs anhand elektrischer Messungen und mit Hilfe des RDEA-Modells wird ein robuster und präziser Zustandsbeobachter abgeleitet und experimentell validiert.

Contents

1. Introduction

1.1. Motivation

Many societies are facing the challenge of an aging population, leading to less available labour and therefore increasing demand on productivity (Marois et al. 2020). One possible approach to this challenge is introducing more automation - a costly and in some areas still impractical task. At the same time, the digitalization of public administrations, industry and everyday life calls for bridges between the digital and the physical realm, among them: sensors, actuators and robots. Commonly cited advantages of classical robots are their precision, repeatability, speed and strength, which are achieved by making the robots as rigid as possible (Verl et al. 2015). This makes them well-suited in areas like manufacturing of mass-produced goods, but at the same time necessitates safety mechanisms such as fences and cages, in order to protect humans from harm. The mechanical rigidity as well as the resulting safety concerns precludes classical robots from certain tasks. This has given rise to a new paradigm of purposefully embedding compliant elements into the mechanical structure of robots, thus opening up the field of soft robotics (Della Santina et al. 2020).

Soft robots have potential applications in the fields of human-robot interaction and inspection or rescue tasks in confined spaces. At the same time, their low mechanical stiffness poses significant challenges for the sensing and control of their shape, both from a mechanical and an algorithmic viewpoint. To this end, dielectric elastomers (DEs) are a promising class of materials, since they are soft, cheap and can operate as actuators and sensors simultaneously. The latter capability is known as self-sensing and could potentially help in solving two significant challenges in soft robotics at the same time.

While the potential of DEs for soft robotics has been recognized (El-Atab et al. 2020; Guo et al. 2021), practical implementations are still in their infancy. At the same time, few advanced concepts known in the field of dielectric elastomer research have been applied to the soft robotics domain. Specifically, there is a noticeable lack of physics-based models and algorithms of DE-based soft robots, even though this approach has proven successful both in classical robotics and in DE research. Therefore, this dissertation aims to bridge the gap between those fields and answer the following main research questions:

1. Is it possible to build better soft robot models in a bottom-up sense, by starting at DE actuator models?

2. How can soft robots benefit from the DE self-sensing capability?

The results presented in this thesis have also been reported in the author's main- and coauthored conference papers (Baltes et al. 2022a; Kunze et al. 2020; Massenio et al. 2022; Prechtl et al. 2021b, 2023, 2022, 2020, 2021c; Soleti et al. 2023) and peer-reviewed journal publications (Prechtl et al. 2021a; Kunze et al. 2021; Baltes et al. 2022b; Prechtl et al. 2024).

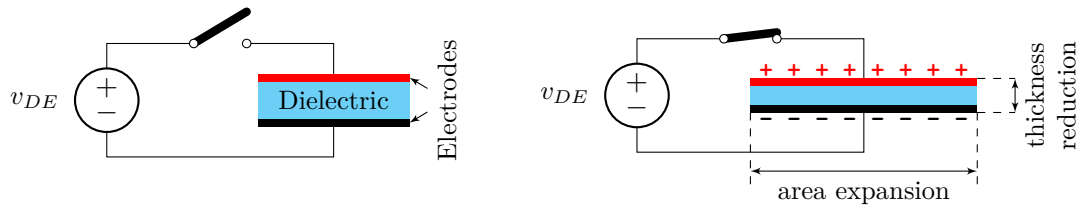

(a) Voltage Off (b) Voltage On

Figure 1.1.: DE actuation principle.

(a) Undeformed state. (b) Mechanical deformation causes a change of capacitance.

Figure 1.2.: DE sensor principle.

1.2. Background and Literature

Much research is available on the topics of Dielectric Elastomers and Soft Robotics. This section aims to provide a comprehensive literature review of relevant topics and to identify open challenges.

1.2.1. Dielectric Elastomer (DEs)

Dielectric Elastomers (DEs) are a class of smart materials with actuation, sensing and generator capabilities (Carpi et al. 2011). At a basic level, they can be understood as flexible capacitors, consisting of a thin polymeric film between two flexible electrodes (see Figure 1.1). At application of a voltage v_{DE}, opposing electric charges appear on both sides of the polymer. The resulting Coulomb forces generate a pressure known as *Maxwell stress*, whereby the polymer film is squeezed together, resulting in an expansion of the surface area and a reduction of thickness (Kofod et al. 2001).

Many compounds can be used as dielectric elastomers, such as the commercially available polyisoprenes (synthetic rubber), silicones (usually PDMS - polydimethylsiloxanes), polyurethanes and polyacrylates. Considering their overall performance characteristics, silicones and polyacrylates are the most popular materials, and are used in most applications and studies. Of the two materials, silicones are generally preferred for higher speeds and better temperature tolerance, while acrylics offer higher actuation strain and higher energy density (Carpi et al. 2011).

In addition to the dielectric, careful consideration must be given to the electrodes as well. The electrodes should be compliant so they don't impede the deformation, but they should also provide good electrical conductivity. Typical choices are either conductive particles (e.g. carbon-black) embedded in a flexible silicone matrix, or corrugated metal electrodes (Carpi et al. 2011). The former typically offers lower conductivity and longer

lifetimes compared to the latter, although recent results on thin film metal electrodes show potential to overcome these limitations (Hubertus 2022).

The discovery of DEs is often attributed to Wilhelm Conrad Röntgen (Röntgen 1880), who in 1880 published experiments he had conducted on natural rubber. Renewed interest in DEs as an actuator technology arose in the early 1990s and has been growing ever since (R. Pelrine et al. 1992; R. E. Pelrine et al. 1998; Carpi et al. 2011). Commonly cited advantages of DEs are high work density, large actuation strains, low cost and the large number of conceivable form factors (Carpi et al. 2011; Guo et al. 2021). As an actuation technology, DEs are often compared to human / mammalian skeletal muscle, as they share similar characteristics (Carpi et al. 2011). In addition, DEs are also considered as sensing technology for shape and strain, by exploiting the direct coupling between geometry and capacitance (Carpi et al. 2011). The principle is illustrated in Figure 1.2. An often-cited advantage of DE-based sensors is the large strain of more than 100 % along with the common properties of DE-based transducers such as softness and flexible formfactors, leading to a large variety of proposed DE sensing devices (Ni et al. 2017; Böse et al. 2023; Gratz-Kelly et al. 2024). In past years, the combination of actuation and sensing modes has led to a new class of so-called *self-sensing* DE actuators (O'Brien et al. 2007; Jung et al. 2008; Rizzello et al. 2018; Gratz-Kelly et al. 2022), allowing to eliminate dedicated sensors from the design of mechatronic systems. Because of their inherent softness combined with the stated advantages, DEs are of major interest to the field of soft robotics (Gupta et al. 2019; Guo et al. 2021).

DE Actuators

DE Actuators (DEAs) can generally be divided according to their operating modes, depending on whether they exploit the area expansion (e.g. membrane actuators) or the thickness reduction effects (e.g. stack actuators). Membrane DEAs are usually paired with a mechanical biasing element in order to provide a restoring force to the actuator, as the choice and design of bias is crucial to their performance. On the other hand, stack actuators contract due to the Maxwell stress only (Hodgins 2016). In the following, only membrane actuators will be considered.

For actuators with one degree of freedom (DoF), a force equilibrium analysis can be carried out graphically (assuming quasistatic conditions). The starting point of actuator design is given by force-displacement curves of the DE at different voltages (usually zero voltage and maximum voltage), obtained in a tensile testing setup. The area between those curves denotes the working area of the DE. In general, the force equilibrium between DE actuator and mechanical bias in the single-DoF case is given as

$$F_{DE}(l_{DE}, v_{DE}) + F_{Bias}(l_{DE}) = 0, \tag{1.1}$$

where F_{DE} represents the recorded DE force at different actuator lengths l_{DE} and different voltages v_{DE}, while F_{Bias} represents the reaction force of the mechanical bias. A graphical solution to (1.1) can be found as the intersection between the left- and right-hand sides of

$$\begin{aligned} F_{DE}(l_{DE}, 0\,\mathrm{V}) &= -F_{Bias}(l_{DE}), \\ F_{DE}(l_{DE}, v_{DE,max}) &= -F_{Bias}(l_{DE}). \end{aligned} \tag{1.2}$$

In Figure 1.3, this method is shown on several types of mechanical biases. The blue and red curves represent the given zero- and high-voltage DE characteristics, while the solid

black lines depict the opposing force from the mechanical bias. Therefore, intersection points between blue and black as well as red and black denote the equilibrium positions of the actuator at corresponding voltages, as they represent graphical solutions to (1.2).

Simple masses and linear springs represent the most conventional types of bias for DEAs (H.-m. Wang et al. 2009; Kovacs et al. 2007; Hodgins et al. 2013). The biasing concepts are illustrated in Figure 1.3a (simple mass) and Figure 1.3b (linear spring). In both cases, the resulting stroke is comparably low, as the bias type is not well adapted to the material characteristics. Note that different DE materials and actuator geometries will produce different force over stretch curves, and in specific cases a linear spring could produce a larger stroke, depending on the shape of the DE working area. Furthermore, a mass bias is often infeasible for practical reasons, since it can cause oscillations due to inertia and since the actuation direction must be parallel to the direction of gravity.

It has been shown (Hodgins et al. 2013; Heim et al. 2009) that nonlinear bistable springs / negative-rate biasing springs (NBS) with regions of negative stiffness are well suited to provide a biasing force to DE actuators. Examples of mechanisms which exhibit the desired negative stiffness feature include nonlinear bistable beams (Hau et al. 2018), attracting permanent magnets (Loew et al. 2018), or more complex types of structures (Berselli et al. 2011). This type of biasing is shown in Figure 1.3c. By carefully tuning the characteristics, the stroke of the DEA can be effectively increased up to 1 order of magnitude compared to linear biasing elements.

Since this idea has been successful in the case of single-DoF actuators and leads to a significantly larger actuator stroke, this work aims to apply it to the case of multiple degrees of freedom (Multi-DoF) actuation. This case is shown in Figure 1.3d. In general, the biasing mechanism can not be designed using the graphical method shown here, as there are several additional factors that determine the effective biasing force, such as the second actuator and the nonlinear kinematics. Therefore, in this example a specific trajectory of the effective biasing force exerted on the left actuator (DE1) is shown for realistic system parameters and input voltages. Among the actuator design examples shown in Figure 1.3, this configuration produces the largest stroke relative to the actuator length, indicating a good match between actuator and backbone structure. During the course of this dissertation, an in-depth analysis of this type of biasing is carried out.

Modeling of DE Actuators

While DEs have significant potential for actuation and sensing applications, they also pose some challenges related to their design and optimization. Therefore, accurate models are required. Applications that benefit from such models are model-based control (predict and compensate material nonlinearities for fast and accurate positioning), model-based design optimization, energy consumption minimization as well as self-sensing and self-monitoring actuator systems (Rizzello 2016).

An accurate DE actuator model establishes the mathematical relationship between the length (or displacement) and the force exhibited by the DEA, and how it is influenced by the application of high voltage. For sensing and applications, the relationship between capacitance and displacement can be included as well. In the case of physics-based models, the effect of design parameters such as actuator geometry and material characteristics on the actuation and sensing performance is naturally included and can be used for design optimization, energy consumption minimization and similar applications.

Type	Sketch	Design of Actuation Stroke	Stroke
(a) Mass	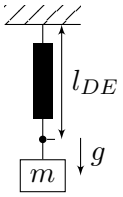	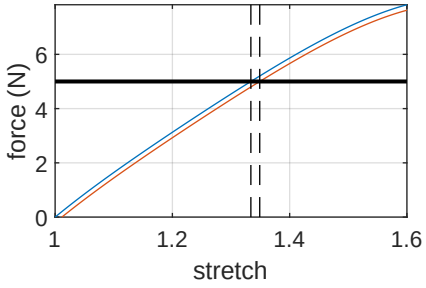	1.51 %
(b) Spring	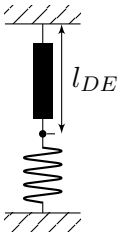	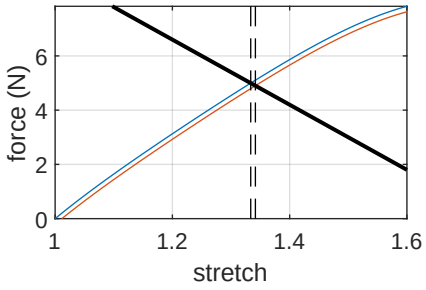	0.80 %
(c) Bistable Nonlinear Spring	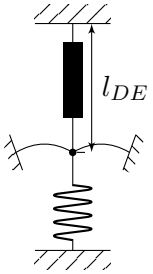	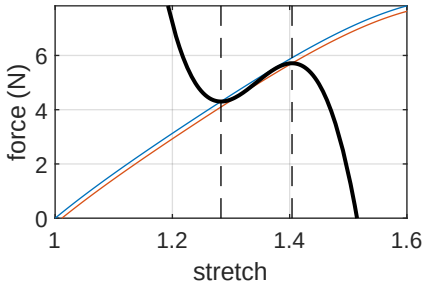	12.73 %
(d) Multi-DoF antagonistic	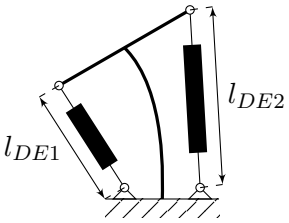	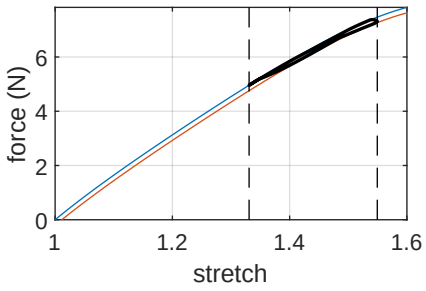	21.86 %
	stretch = $\frac{l_{DE}}{L_1}$ (actuator length relative to relaxed length)	DE 0 V DE 3 kV -F_{bias}	

Figure 1.3.: RDEA biasing mechanisms.

Naturally, many works on DE modeling have been published in the last decades (Lu et al. 2020). The family of tensorial models allows for a detailed description of the complex material behaviour and accounts for local phenomena (T. Wissler 2007), although these models are typically too detailed and computationally expensive for control applications. On the other hand, energy-based models lend themselves to more compact formulations at the expense of less-detailed, holistic descriptions (Suo 2010).

This work is specifically concerned with the modeling of rolled DE actuators (RDEAs). In the last few years, a number of authors have investigated modeling and simulation of such transducers. In R. Zhang et al. 2006, an acrylic RDEA with a spring core is investigated. A set of geometrical simplifications (fixed inner diameter, layers volume conservation) allowed the authors to find an algebraic relation for the distribution of radial strain inside the roll. The authors, however, did not develop an explicit mechanical model for the actuator. An analytical model for an acrylic RDEA with elastic core is discussed in M. Wissler et al. 2007. In this paper, the authors focused on modeling and characterizing the blocking force behavior only. In Rajamani et al. 2008, an axial-symmetric finite element model for an acrylic RDEA with an elastic core is presented. The developed model permits to predict the actuator displacement in response to an applied electromechanical load. Nonetheless, such a finite element formalism is unsuitable for real-time simulations and control application. In J. Li et al. 2019, the authors analyze the behavior of a bending-type acrylic RDEA with an elastic core. Also in this case, a finite element framework is adopted to describe the complex core motion. A further example of bending RDEA based on an acrylic elastomer is analyzed in Pei et al. 2004. In the paper, mathematical equations are derived to correlate the bending angle and lateral force of multiple-degree-of-freedom RDEAs with segmented electrodes. Modeling and simulation of core-free RDEA configurations has also received some attention in literature. Carpi and De Rossi presented in Carpi et al. 2004 an electromechanical model for a silicone-based DEA, shaped as a single-layer hollow cylinder. Their model permits to accurately predict the low-strain behavior of the transducer. In Jones et al. 2012, Jones and Sarban presented a model for a coreless silicone-based RDEA. The actuator is described by means of a grey-box model, by assuming a second order stress-strain dynamics whose parameters are identified experimentally. In H. Zhao et al. 2018, the authors developed a finite element model for a core-free RDEA. The work aimed at evaluating the effects due to electrode-free roll area, and using them as a reference to develop a simplified analytical model. Nonlinear effects due to large deformation were neglected.

A further area of concern in DEA modeling is a complex hysteretic response which reflects the material dissipation process. The topic of hysteresis modeling and compensation for elastomers has been identified in the literature as an important task. Most works focus on the rate-dependent hysteresis observed in the DEA stress-stretch response, which can be well described by means of viscoelasticity theory (Wineman et al. 2000; Foo et al. 2012; T. Nguyen et al. 2021). A far less studied topic in the DEA modeling literature concerns the rate-independent hysteretic effects, which are experimentally observed when deforming some materials (e.g., silicone) in the sub-Hz regime (Kunze et al. 2021), and cannot be described by means of commonly adopted viscoelastic models. In this context, some authors investigated phenomenological models for rate-independent hysteretic effects observed in the voltage-displacement characteristics of DEA devices (Zou et al. 2018; Huang et al. 2022; Z. Li et al. 2023; Xu et al. 2021), while few others focused on the physics-based description of stress-stretch hysteresis of elastomers, e.g. Lion 1997; Sause et al. 2007, or

dielectric elastomers specifically (De Tommasi et al. 2014).

On the one hand, phenomenological modeling approaches provide a description of the DEA system based on an input-output black box perspective. While high accuracy can be achieved in terms of hysteresis modeling and compensation, it is unclear how well those results translate to changes in system parameters and environmental conditions. One would expect different hysteresis shapes in the case of a DE membrane biased with various mass-spring systems, or even a nonlinear biasing element such as a bistable spring.

On the other hand, physics-based hysteresis models are able to accurately describe the stress-stretch relationship of the elastomer material, and thus should be capable of adapting to different biasing elements external to the modeled hysteretic system. At the same time, for real-time control, a balance must be kept regarding computational complexity and the identifiability of required parameters. The model proposed in Lion 1997 fits the stated requirements, but does not account for Maxwell stress occurring in dielectric elastomers, as well as the geometric nonlinearities and constraints which are present in many DEA layouts.

In Mertens et al. 2022, the authors similarly combine classical lumped-parameter elastomer models with Maxwell and Prandtl elements to achieve a model exhibiting both rate-dependent and rate-independent hysteresis effects, although they focus on the electrode material and don't consider the full actuator. As a result, the proposed dynamic model is only discussed at small strains and without considering electromechanical coupling during high-voltage actuation. Furthermore, the constitutive equations can not be fully expressed as ordinary differential equations in continuous time, therefore an iterative method is needed to solve for the total mechanical stress.

From the above discussion, it can be noted that the currently available approaches for RDEA modeling lack a general and uniform methodology, and are rather focused on the specific issues of the system under investigation. This is possibly due to the wide spectrum of RDEA configurations which have been investigated in the literature, which may differ in terms of material (acrylic, silicone), rolling geometry (cylinder, spiral), and core (elastic, hollow). Clearly, for many types of RDEA configurations, the development of accurate mathematical models capable of accounting for their specific features still represents an open problem. In addition to that, the development of model-based control and self-sensing strategies for RDEAs is still a largely unexplored research area, especially in the context of soft robotics applications.

1.2.2. Soft Robotics

In recent years, making robots soft(er) has emerged as a new paradigm in the field of robotics (Verl et al. 2015). The definition is as simple as it is consequential:

> "Soft robots are robotic systems with purposefully designed compliant elements embedded into their mechanical structure." (Della Santina et al. 2020)

Enabled by technological advancements and driven by the need for better human-robot interaction (Albu-Schaffer et al. 2008), this trend brings opportunities as well as new technological challenges ranging from manufacturing to modeling and control (Della Santina et al. 2023). Among the commonly cited advantages of soft robots are the strong adaptability and capability to work in unstructured environments, thanks to their mechanical compliance (Gupta et al. 2019; Guo et al. 2021). At the same time, this mechanical compliance

calls for actuators and sensors to be integrated into the soft robot which are themselves compliant. In addition, soft robots benefit from lightweight components and a high level of integration of components and functionality inside the soft robot body (El-Atab et al. 2020).

In this regard, many actuation technologies are being explored for soft robots. Among them are conventional technologies such as cable-driven systems, electrical motors, pneumatics and hydraulics. These usually provide the desired actuation forces and speeds with ease, but involve rigid and bulky components either inside the robot itself or nearby, limiting the achievable performance characteristics of the soft robot in terms of softness, mobility, lightweightness and low-cost. To overcome these limitations, many types of active materials are being explored, responding to electrical, thermal, magnetic or light-based stimuli (El-Atab et al. 2020).

DE Soft Robots

Among the active materials which are being explored for soft robots, dielectric elastomers stand out with a unique combination of benefits: DEs are themselves soft and lightweight, offer large-strain actuation and sensing, can be used as actuators and sensors simultaneously, and they can be deeply integrated into any surrounding structure thanks to the wide range of possible form factors, all while being manufactured at low cost (cf. Section 1.2.1). In fact, DEs have seen continuous interest in the field of soft robotics (Gupta et al. 2019; Guo et al. 2021; El-Atab et al. 2020). Some soft robotic applications based on DE actuators which have been presented in recent years include soft grippers (Imamura et al. 2017), manipulators (Xing et al. 2020), flying microrobots (Chen et al. 2019), fish-like robots (Shintake et al. 2018), and hexapod crawling robots (C. T. Nguyen et al. 2017), to mention a few.

When considering DE actuators for soft robotic applications, one significant challenge known from single-degree-of-freedom actuation reappears. As reviewed Section 1.2.1, a DEA membrane needs to be preloaded with a mechanical biasing system in order to effectively work as an actuator. Such a biasing mechanism heavily influences the overall DEA performance, in terms of both stroke and force. It is remarked how, up to now, the optimization of the DEA biasing mechanisms has mostly been conducted in the context of simple one-dimensional actuators, possibly for two reasons. On the one hand, biasing system optimization methods are normally based on design graphical criteria. Therefore, it is intrinsically difficult to transfer them to systems driven by multiple DEAs, in which the graphical intuition is unavoidably lost. On the other hand, the design of multi-DoF biasing mechanisms which exhibit a controlled (possibly negative) stiffness along different axes represents a technologically challenging task. If the integration of bistable concepts within multi-DoF DEA systems is addressed, novel soft robots capable of large displacements and/or lower energy consumption can be effectively designed.

Modeling of DE Soft Robots

While a significant amount of research has been conducted on the modeling of soft continuum robots (Burgner-Kahrs et al. 2015), fewer works have considered the modeling of DE-based soft robots. In DE literature, the conceptually similar multi-DoF DE actuators are also noted to largely lack accurate analytical modeling tools (Nalbach et al. 2020).

To this end, our research group proposed a soft robotic module based on rolled DE actuators, named "T-Platform", serving as an example for the development of advanced modeling and self-sensing methods in the course of this dissertation. In anticipation of a more thorough introduction in Chapter 2 and detailed modeling and analysis performed in Chapter 4, a brief review of related works in the literature is given here.

Follador et al. 2014, 2015 presented an interesting bending actuator similar to the T-Platform. Two strip-shaped DEAs are used in an antagonistic configuration to compress a beam element so that it buckles, creating a bistable bending actuator. The authors used an assumed-shape beam model to analyze the potential energy landscape of the structure as a function of bending angle and actuator voltage. In this way, they were able to demonstrate and theoretically retrace both large-angle bending by switching between the two equilibria and continuous transitions in between by means of simultaneous activation of the DEAs. The modeling approach is somewhat limited by pre-assuming the buckling shape and only considering a single degree of freedom (pure bending). This has several consequences. Firstly, the onset of buckling by means of the backbone compression is not explicitly captured, limiting the model to system configurations that exhibit this specific bistable bending mode. On the other hand, the T-Platform model can transition between mono- and bistable behavior seamlessly, since the effect of the compressive forces is explicitly considered in the beam potential energy. Secondly, by only considering pure bending motions, the influence of lateral motion on the beam potential energy is neglected. In the T-Platform, lateral movement in addition to the bending motion is observed and accounted for by the model, especially when the placement of actuator mounting positions favors the occurrence of resulting lateral forces on the backbone.

Masoud et al. 2022 presented a general modeling approach to DE systems interacting with elastic structures. They use the Rayleigh-Ritz method to derive an assumed-shape beam model tailored to the specific boundary conditions present in an actuator system. Inspired by our previous work (Prechtl et al. 2021c), they also briefly discuss how their approach could, in principle, be applied to a multi-DoF T-shaped structure which can be considered identical to the here-proposed T-Platform. For the scope of the paper, the authors focus on an "inverse" T-Platform consisting of a single central DEA and two beams on each side. An energy-based single-DoF stability analysis is carried out, qualitatively agreeing with the results of our previously published study on the energy landscape of bistable T-Platforms (Prechtl et al. 2021b), noting the significantly improved actuation performance thanks to the bistable buckled beam. As no experimental validation is performed, it remains an open question how the approach fares in practice.

Self-Sensing of DE Soft Robots

Several surveys have recently emphasized the need for soft robot proprioception, i.e., the capability of a soft robot to sense its own shape in real time, so as to enable closed-loop motion control (Lin et al. 2023; Dou et al. 2021; H. Wang et al. 2018; Della Santina et al. 2023). It is remarked, however, that achieving this goal still remains an open challenge in soft robotics (S. Wang et al. 2023). The main challenge of shape sensing for soft robots arises from the fact that a large number (up to infinity) of degrees of freedom (DoF) must be estimated from a limited number of measurements (Della Santina et al. 2023). To practically address this issue, a possible solution consists of using many sensors distributed over the robot body. As an example, the local curvature of long and slen-

der robots can be reconstructed using strain gauges, and the overall shape estimated by means of interpolation (Cianchetti et al. 2012; Q. Zhao et al. 2022). A disadvantage of this method is the larger number of measured signals, which require electrical connections, dedicated electronics, and significant processing power. Alternatively, model-based or machine learning approaches can be used to infer missing information based on a restricted number of measurements. In Lunni et al. 2018, a state observer relying on an optical curvature sensor was used for shape estimation but, due to the adoption of a simplified modeling approach, the method only provided a steady-state result. The authors of Shu et al. 2022 used measurements from flexible resistive sensors as input to a neural network for posture perception. The approach was effective in avoiding complex modeling efforts for the highly nonlinear and hysteretic sensor behavior, but had to rely on a comparatively large number of feedback variables to estimate a single bending angle. In general, using external sensors leads to an increase in system stiffness and overall size, due to the lack of tight integration between sensors and actuators. In some cases, like in cable-driven soft robots, the sensing feature can be directly integrated within the same component performing actuation (Pustina et al. 2023). For instance, in Liu et al. 2023 the configuration and tension of a cable-driven soft robot were estimated via the actuator lengths, reconstructed through motor-level sensors. The approach produces accurate sensing, but requires detailed nonlinear modeling and calibration of friction and hysteresis, as well as a custom and rather complex real-time numerical solving strategy.

All methods discussed so far are either sensor-based, and thus agnostic to the actuation mechanism, or specifically tailored to pneumatically- and cable-driven soft robots. These mechanisms allow for soft and compact designs, but lack intrinsic self-sensing features and have to rely on external hardware such as cable-driving motors or air compressors. Some of those shortcomings are addressed in Preechayasomboon et al. 2021, where the authors utilized the actuation fluid as an integrated resistive sensor, or in Yang et al. 2022, where currently unused actuators can serve as sensors. Those approaches rely either on additional wiring or on alternating between actuation and sensing functions, thus leaving room for technologies offering even tighter integration. To this end, dielectric elastomer (DE) transducers may represent an interesting alternative technology for soft robotics (Shintake et al. 2018; Gupta et al. 2019; Guo et al. 2021; Yasa et al. 2023). A DE actuator (DEA) consists of a polymeric membrane (e.g., silicone) sandwiched between compliant electrodes, whose in-plane expansion can be controlled via an external voltage signal. Other than exhibiting high stretchability, inherent softness, smooth controllability, and ease of integration, DEs can also work as *artificial muscles* and *artificial nerves* at the same time, exploiting a so-called self-sensing operating mode. More specifically, changes in DEA electrical capacitance can be detected in real time during high voltage actuation, and used to reconstruct the deformation (Gisby et al. 2013; Hoffstadt et al. 2014) and/or the force (Rizzello et al. 2020b) of the transducer, thus allowing to implement *sensorless* position (Rosset et al. 2013; Rizzello et al. 2016; Cao et al. 2018) and compliance (Rizzello et al. 2020b) control loops. The term sensorless, widely used in the literature on electric motors, here refers to architectures in which mechanical quantities are estimated without including additional electromechanical sensors into the system, but instead relying on available electrical measurements (e.g., voltage, current) performed on already existing transducers (i.e., the actuators themselves). Similar techniques have been applied to other smart transducers such as piezoelectric positioning devices (Ivan et al. 2009b,a; Rakotondrabe 2013) to obtain real-time estimation of displacement, force, and system state. It

is remarked that the existing DE literature solely focused on *actuator-level self-sensing*, i.e., techniques to reconstruct the deformation and/or force of a simple, single-degree-of-freedom (DoF) DE component. In case of multi-DoF structures actuated by several DE transducers, a more advanced concept referred to as *system-level self-sensing* can be implemented, in which different actuator-level estimations are combined to reconstruct some global system information. In case of DE soft robots, this approach allows reconstructing the full configuration of the system during an actuation task based on DEA voltage and current signals only, without the need to embed extra mechanical or electrical sensors in the structure. This concept will open up the possibility of implementing integrated proprioception and sensorless closed loop control for DE soft robots. To the author's best knowledge, no previous work has investigated similar concepts for DEA-driven multi-DoF systems. Factors which contribute to making this problem challenging, compared to the single-DoF case, include underactuation as well as several system nonlinearities.

1.3. Contributions and Outline of this Thesis

Chapter 2 introduces the physical prototypes serving as examples for the methods developed in this dissertation. Specifically, the rolled DE actuators (RDEAs) and the soft robotic module named "T-Platform" are introduced and their physical operating principle is discussed. The challenges related to hardware design, control and sensing are elaborated in order to set the stage for the following chapters.

Chapter 3 focuses on the development of a physics-based model for rolled dielectric elastomer actuators (RDEAs). The model is able to predict the actuator force given the actuator voltage and length in static and dynamic loading conditions, while considering the influence of parameters such as material properties and actuator geometry. Three different variants of an actuator model are derived and analyzed, before choosing the most appropriate variant for practical use. The first variant will be called the three-ring model (3R), and considers the internal structure of a rolled DE actuator, allowing us to study the influence of roll composition on actuation behavior. The second and third variants are derived by introducing additional assumptions on the 3R model, and provide fast and accurate approximations under suitable conditions on geometric parameters. Finally, the effects of rate-dependent and rate-independent hysteresis are considered by introducing a rheological model based on Maxwell-Lion elements. The theoretical results are validated in experimental campaigns.

In **Chapter 4**, a physics-based model of a soft robotic system based on RDEAs (named "T-Platform") is developed and analyzed. An interesting property of the system under consideration is its bistability, which is investigated in depth and utilized for increased actuation performance. In an experimental campaign, it is shown that the static and dynamic behaviour is accurately captured, and trends regarding the influence of physical parameters are predicted correctly.

Chapter 5 is dedicated to a system-level self-sensing algorithm for the aforementioned T-Platform. The algorithm is able to estimate the mechanical state of the structure without requiring additional electro-mechanical sensors, solely relying on electrical measurements performed on the DEs during high voltage actuation. Based on the estimated length of the rolled DE actuators obtained using an actuator-level self-sensing algorithm and the physics-based model from Chapter 4, an observer based on an Extended Kalman

Filter (EKF) is derived to estimate the system configuration and velocity. Experimental validation shows that the scheme accurately estimates the state of the physical prototype while staying robust to external disturbances.

Chapter 6 summarizes the results and discusses possible directions of further research.

The **Appendices** provide supplementary information such as identified parameter values.

2. Fundamentals of DE-based Soft Robotics

This chapter introduces the physical devices studied in this dissertation: rolled DE actuators (RDEAs) and a soft robotic demonstrator platform based on the same ("T-Platform"). The problems of modeling and estimation are introduced at a conceptual level.

2.1. Rolled DE Actuators (RDEAs)

This work focuses on rolled DE actuators (RDEAs) and their application to soft robots. Figure 2.1 shows the basic principle, which is largely similar to the basic operating principle of all DE actuators: a polymeric film sandwiched between flexible electrodes is rolled into a dense spiral shape. When high voltage is applied, a reduction in diameter and an axial elongation is observed.

The design, manufacturing and characterization of the RDEAs used in this work is described in detail by Kunze et al. 2021. They are manufactured from the silicone-based, commercially available Elastosil™ 2030 (Wacker 2023) and use carbon-black-based screen-printed electrodes suspended in PDMS. In Section 3.1, a detailed physics-based model of rolled DE actuation behavior will be developed. In subsequent chapters, the RDEAs will be considered as part of a soft robotic structure, serving as a framework for the development of effective biasing methods and a system-level self-sensing method based on actuator-level capacitance measurements.

Figure 2.2 shows the repsonse of different physical RDEA specimens during tensile testing. Here, the actuator force is recorded while controlling the displacement according to a presribed trajectory. The actuator is therefore stretched in several cycles with increasing amplitude. It becomes apparent that the actuator response is defined by several factors, among them actuator geometry (specimens have different lengths and thicknesses), actuation voltage ("HV" indicates high voltage actuation) and loading conditions (force depends

(a) Voltage off (b) Voltage on

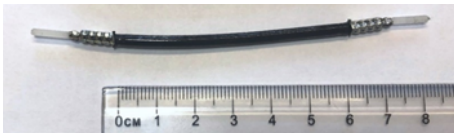

(c) Physical RDEA Specimen (Kunze et al. 2021)

Figure 2.1.: Design and functioning of the RDEA.

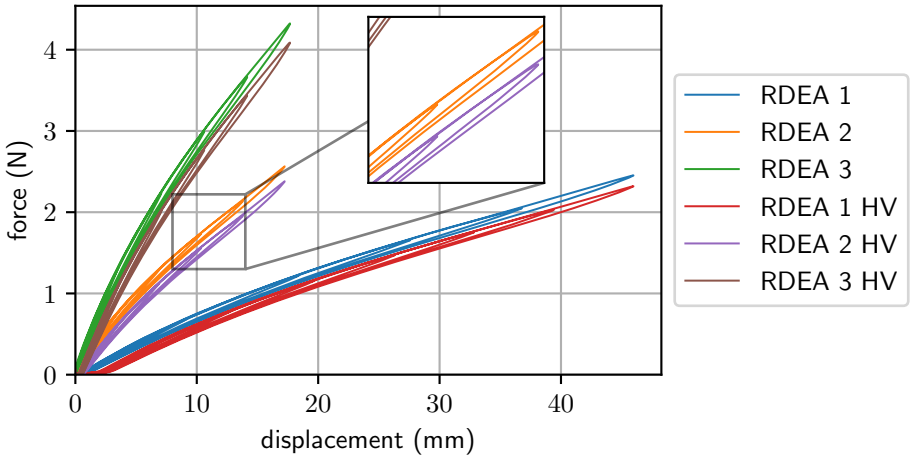

Figure 2.2.: Tensile tests of different RDEAs exhibiting complex nonlinear response depending on actuator geometry, loading rate and applied voltage.

on loading history, resulting in an obsevered hysteresis). Predicting this behaviour precisely will be a major contribution of this work (cf. Chapter 3).

2.2. Modular Soft Robotic Platform (T-Platform)

The T-Platform arose out of the search of an effective concept how to combine DE actuators and soft robots. The design should be modular, so that in principle many possible robot designs can emerge from assembling some basic building blocks. In this way, for example a soft robotic tentacle arm could be built up from gradually smaller modules stacked on top of each other. In previous work, the double-cone concept was investigated as a candidate building block, but proved to be limited in terms of actuation performance (Nalbach et al. 2020). This dissertation started with the investigation of a second concept later called the T-Platform, which will be described in detail hereafter. The basic idea is a generalization of previous linear DE actuation principles, which is to combine pretensioned DEs with a suitable mechanical biasing element to yield large actuation strokes that optimally utilize the electromechanical potential of DE materials.

Figure 2.3a shows the essential T-Platform components, consisting of two rolled DE actuators (introduced in Section 2.1), a flexible backbone and a rigid top plate. The RDEAs are pretensioned and connected to the backbone in such a way that the backbone is compressed axially. Figures 2.3b and 2.3c show two physical prototypes of the T-Platform used throughout this work. They represent different stages of development differing mainly in size, actuator mounting technique and backbone material. Both allow to adjust the mounting positions and to exchange backbone and actuators. For further details, the reader is referred to Section 4.3.

The vision for future works is to create a tentacle-like soft robotic arm composed of stacked T-Platforms, as shown in Figure 2.4. For the scope of this dissertation, only planar movement of a single module was considered, while further research will focus on developing a three-dimensional modular soft robot as shown on the right.

Assuming a symmetric configuration, without any voltage applied the structure would

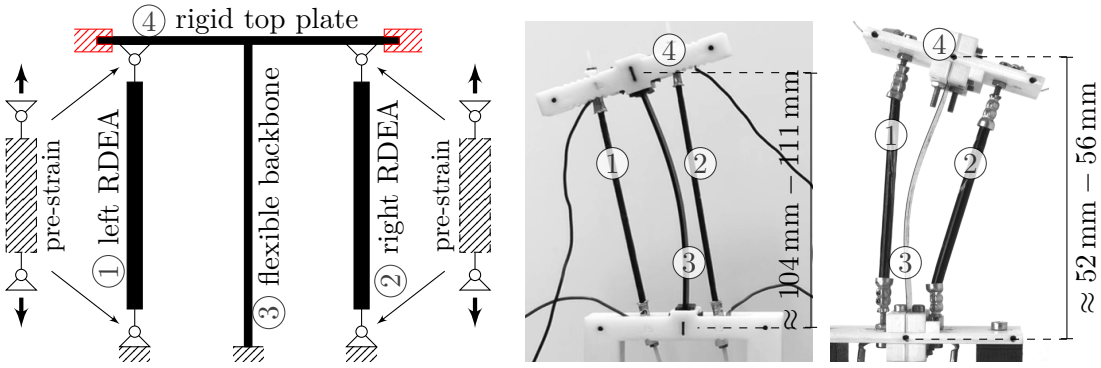

(a) Assembly using pre-strain. (b) Gen. A prototype (c) Gen. B prototype

Figure 2.3.: T-Platform assembly and physical prototypes

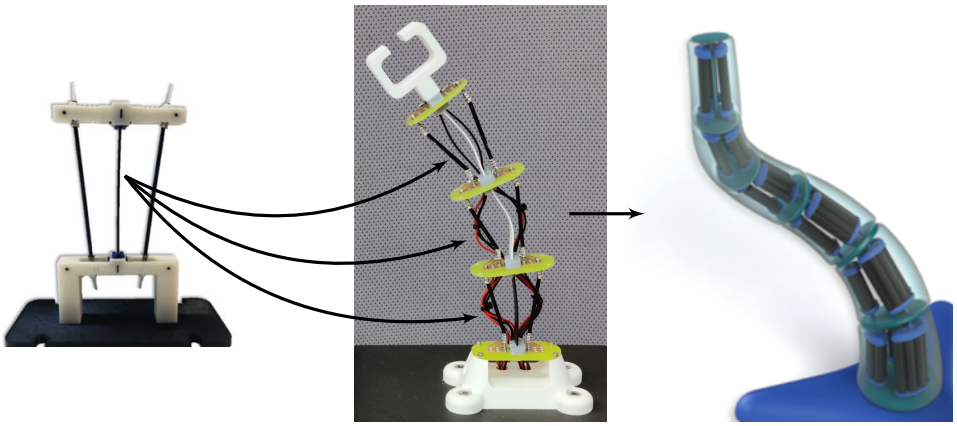

Figure 2.4.: Stacking Concept: from single T-Platform (left, Baltes et al. 2022b) to planar manipulator (center) to three-dimensional tentacle arm (right).

assume a neutral position such as ② in Figure 2.5. If one of the actuators is activated using high voltage, its stiffness and in turn the resulting tensile force is lowered. Therefore, the whole structure shifts towards the passive actuator, which exhibits a larger force on the structure. This is shown in Figure 2.5, positions ① (bending to the left when the right actuator is active) and ③ (bending to the right when the left actuator is active).

A more complex actuation pattern exhibited by the T-Platform is bistable actuation. If the compressive force seen by the backbone is large enough, buckling occurs, resulting in either a bent-left or bent-right configuration, even without high-voltage actuation. The neutral configuration ② becomes unstable. This actuation pattern is desirable because it leads to significantly enhanced actuation performance. As will be shown in this work, this is an instance of negative-stiffness biasing, an idea known from linear DE actuator designs. In this work, a theoretical framework is developed to understand, predict and systematically exploit this effect.

Another interesting problem is posed by underactuation, since the platform has fewer actuators than degrees of freedom. The top-plate of the T-Platform can rotate and is moving in two planar directions, but only two DE actuators are available to control the movement. This creates challenges in control as well as in sensing. In this work, a method

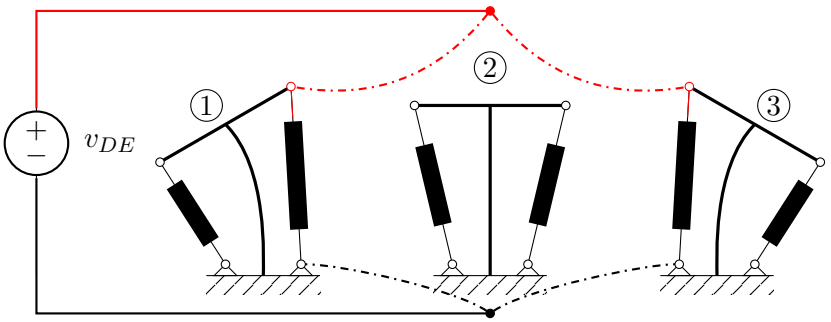

Figure 2.5.: Actuation modes of the T-Platform: (1) right actuator active – (2) neutral position – (3) left actuator active.

is developed to overcome the sensing challenge, enabling real-time pose estimation just from voltage and current measurements in the actuators.

3. Modeling of Rolled Dielectric Elastomer Actuators

This chapter is concerned with the mathematical modeling of rolled dielectric elastomer actuators as the fundamental actuation and sensing components in the "T-Platform" soft robotic system. The goal is to create a tool for design and performance optimization both of the actuators themselves and also for the actuation systems they are part of, hence a physics-based approach is chosen. In addition, the model should be suitable for the development of closed-loop control and self-sensing algorithms, posing certain requirements on numerical performance and therefore on the model structure.

The chapter starts with a general introduction to energy-based DE modeling, before proceeding with the development of three different variants of an actuator model. The first variant will be called the three-ring model (3R), and considers the internal structure of a rolled DE actuator, allowing us to study the influence of roll composition on actuation behavior. The second and third variants are derived by introducing additional assumptions on the 3R model, and provide fast and accurate approximations under suitable conditions on geometric parameters. Finally, the effects of rate-dependent and rate-independent hysteresis are considered by introducing a rheological model based on Maxwell-Lion elements. The theoretical results are validated in experimental campaigns.

The results discussed here have also been reported in publications Prechtl et al. 2021a and Prechtl et al. 2023 – they are presented here in consolidated form, partly verbatim.

3.1. Physics-based RDEA Model

In this section, a lumped-parameter model for RDEAs is developed. Starting from a general free-energy framework, a detailed quasi-static model capable of describing the RDEA electromechanical response is first developed and used as a reference. Subsequently, suitable approximations of this model are derived, which are capable of capturing the main features of the RDEA response in a more simple and computationally efficient way. Comparative studies are then conducted in simulation, in order to understand the operating ranges in which the developed approximations are capable of tightly matching the reference model. To account for both rate-dependent and rate-independent hysteretic effects, an extension making use of a Maxwell-Lion description of the hysteretic behavior is introduced. In this way, it is possible to capture both rate-dependent and rate-independent hysteresis effects, as well as electromechanical coupling, in a thermodynamically consistent way.

3.1.1. DE Modeling Framework based on Free-Energy

In this section, we start by introducing the general DE modeling framework proposed by Suo 2010, before applying it to the case of rolled DE actuators. Generally, there are two

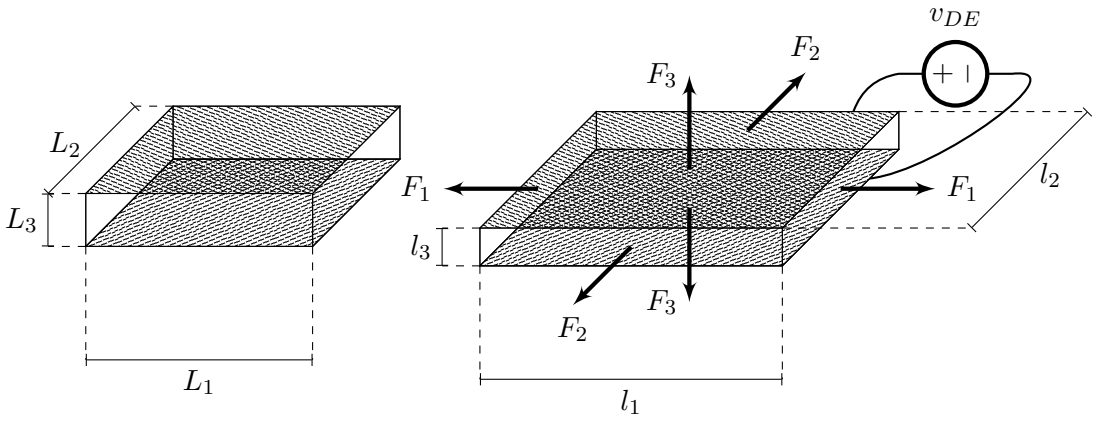

(a) Undeformed configuration. (b) Deformed configuration.

Figure 3.1.: Sketch of a cubic sheet of DE material.

dominant approaches to modeling DEs, namely the tensorial (T. Wissler 2007) and the free-energy based approach (Suo 2010). In this work, we focus on the latter, since an energy-based description of the actuator is advantageous for modeling the total system energy in a soft robot and subsequently, allow a whole toolbox of energy based methods to be applied.

A fundamental assumption of the theory presented in this section is that the material undergoes homogeneous deformations, so that the behaviour can be described in terms of average quantities such as stress, strain, and electric field strength. This assumption keeps the resulting models mathematically tractable and thus suitable for real-time control and self-sensing applications. In order to simplify the initial treatment, the discussion of dissipative effects is postponed to Section 3.1.7.

Consider a cubic sheet of DE material of dimensions L_1, L_2 and L_3 as shown in Figure 3.1a. The upper and lower surfaces are covered by compliant electrodes, so that the body becomes a flexible capacitor. A voltage v is applied, resulting in a stored charge q. Furthermore, we consider forces acting along the three dimensions F_1, F_2 and F_3. Correspondingly, L_1, L_2, L_3 shall refer to the initial dimensions of the body without external forces applied, while l_1, l_2, l_3 refer to the size of the deformed body (cf. Figure 3.1b).

The first important step in free-energy modeling is to postulate a functional Ψ describing the (Helmholtz) free-energy stored in the system, i.e. in loose terms, energy that is available to perform work. This energy functional depends on variables that describe the state of the system, in our case it will be l_1, l_2, l_3 and q. Now, the principle of virtual work dictates that for a conservative and isothermal system, the internal virtual work, given as the increase of the Helmholtz free-energy $\delta\Psi$, is equal to the external virtual work δW performed on the system:

$$\delta\Psi = \delta W = F_1\delta l_1 + F_2\delta l_2 + F_3\delta l_3 + v\delta q. \tag{3.1}$$

In other words, we postulate that the work performed by external forces leads to a corresponding increase in free-energy and vice versa. In the case of DE modeling, the external virtual work is performed by mechanical forces F_1, F_2, F_3 and electrical forces v (the elec-

trical voltage can be viewed as an electrical force acting on a charge, normalized by the charge).

In order to simplify the mathematical treatment, we first perform a change of variables in order to move from absolute quantities to normalized ones. We introduce

$$\psi = \frac{\Psi}{l_1 l_2 l_3}, \tag{3.2}$$

$$\sigma_1 = \frac{F_1}{l_2 l_3}, \sigma_2 = \frac{F_2}{l_1 l_3}, \sigma_3 = \frac{F_3}{l_1 l_2}, \tag{3.3}$$

$$\lambda_1 = \frac{l_1}{L_1}, \lambda_2 = \frac{l_2}{L_2}, \lambda_3 = \frac{l_3}{l_3}, \tag{3.4}$$

$$E = \frac{v}{l_3}, \tag{3.5}$$

$$D = \frac{q}{l_1 l_2}, \tag{3.6}$$

where ψ is the free-energy density, $\sigma_{1,2,3}$ denote the stresses in each direction (given as force divided by cross-sectional area), and the stretches $\lambda_{1,2,3}$ are given as the actual length divided by the reference length. In addition, we have the electrical field strength E and the electrical displacement D (charge divided by cross-sectional area).

By substituting into (3.1), we obtain

$$\delta\left(\lambda_1\lambda_2\lambda_3\psi\right) = \sigma_1\lambda_2\lambda_3\delta\lambda_1 + \sigma_2\lambda_1\lambda_3\delta\lambda_2 + \sigma_3\lambda_1\lambda_2\delta\lambda_3 + E\lambda_3\delta\left(D\lambda_1\lambda_2\right), \tag{3.7}$$

which can be written as

$$\delta\psi = \frac{1}{\lambda_1}\left(\sigma_1 - \psi + ED\right)\delta\lambda_1 + \frac{1}{\lambda_2}\left(\sigma_2 - \psi + ED\right)\delta\lambda_2 + \frac{1}{\lambda_3}\left(\sigma_3 - \psi\right)\delta\lambda_3 + E\delta D. \tag{3.8}$$

The free-energy density ψ models the material behaviour in dependence of the system variables $\lambda_1, \lambda_2, \lambda_3, D$. By considering this functional relationship, the variation of $\psi(\lambda_1, \lambda_2, \lambda_3, D)$ is given as

$$\delta\psi(\lambda_1, \lambda_2, \lambda_3, D) = \frac{\partial\psi}{\partial\lambda_1}\delta\lambda_1 + \frac{\partial\psi}{\partial\lambda_2}\delta\lambda_2 + \frac{\partial\psi}{\partial\lambda_3}\delta\lambda_3 + \frac{\partial\psi}{\partial D}\delta D. \tag{3.9}$$

Therefore, (3.8) becomes:

$$\begin{aligned} 0 = &\left(\frac{\sigma_1 - \psi + ED}{\lambda_1} - \frac{\partial\psi}{\partial\lambda_1}\right)\delta\lambda_1 \\ &+ \left(\frac{\sigma_2 - \psi + ED}{\lambda_2} - \frac{\partial\psi}{\partial\lambda_2}\right)\delta\lambda_2 \\ &+ \left(\frac{\sigma_3 - \psi}{\lambda_3} - \frac{\partial\psi}{\partial\lambda_3}\right)\delta\lambda_3 \\ &+ \left(E - \frac{\partial\psi}{\partial D}\right)\delta D. \end{aligned} \tag{3.10}$$

If the material model ψ and $\lambda_1, \lambda_2, \lambda_3, D$ are given, the stresses $\sigma_1, \sigma_2, \sigma_3$ and the electrical field strength E can be found by the method of equating the coefficients:

$$\begin{cases} \sigma_1 = \lambda_1 \dfrac{\partial \psi}{\partial \lambda_1} + \psi - ED \\ \sigma_2 = \lambda_2 \dfrac{\partial \psi}{\partial \lambda_2} + \psi - ED \\ \sigma_3 = \lambda_3 \dfrac{\partial \psi}{\partial \lambda_3} + \psi \\ E = \dfrac{\partial \psi}{\partial D} \end{cases} \tag{3.11}$$

Next, a model of the free-energy density ψ is chosen, i.e. the relationship between the variables $\lambda_1, \lambda_2, \lambda_3, D$ and the free-energy density ψ is defined. Generally, ψ is partitioned as

$$\psi(\lambda_1, \lambda_2, \lambda_3, D) = \psi_m(\lambda_1, \lambda_2, \lambda_3) + \psi_e(D, \lambda_1, \lambda_2, \lambda_3) \tag{3.12}$$

into a mechanical contribution ψ_m and an electrical contribution ψ_e. The first component ψ_m models the hyperelastic behaviour of the polymer. Many energy functionals have been proposed, differing in the number of parameters and method of derivation (phenomenological or micromechanical) as well as computational complexity (Melly et al. 2021). The most common choices are the Neo-Hookean (Rivlin et al. 1948b), the Mooney-Rivlin (Mooney 1940; Rivlin et al. 1948a), Ogden (Ogden 1997), Yeoh (Yeoh 1993), Gent (Gent 1996) and Arruda-Boyce (Arruda et al. 1993) models. The actuator models derived in this work are based on the Yeoh free-energy density:

$$\psi_m(\lambda_1, \lambda_2, \lambda_3) = \sum_{i=1}^{3} C_{i0} \left(\lambda_1^2 + \lambda_2^2 + \lambda_3^2 - 3 \right)^i, \quad j \in \{a, b, c\}, \tag{3.13}$$

where C_{i0}, $i \in \{1, 2, 3\}$, represent constitutive material parameters.

The second contribution to the overall free-energy density, given be ψ_e, models the dielectric properties of the material. According to Suo 2010; Rizzello 2016, several possible choices exist. The most common model is the *Ideal DE*

$$\psi_e(D) = \frac{D^2}{2\epsilon_0 \epsilon_r}, \tag{3.14}$$

which assumes that the DE behaves as an ideal capacitor: the relative electrical permittivity ϵ_r is constant and the field strength E is proportional to the electrical displacement D. Another choice is the *DE with electrostriction* with

$$\psi_e(D, \lambda_1, \lambda_2, \lambda_3) = \frac{D^2}{2\varepsilon_0 \varepsilon_r(\lambda_1, \lambda_2, \lambda_3)}, \tag{3.15}$$

where the relative permittivity depends on the stretches. Finally, the *DE with polarization saturation* model

$$\psi_e(D) = \frac{D_s}{\varepsilon_0 \varepsilon_r} \left(\frac{D_s}{2} \ln(D_s^2 - D^2) + D \tanh^{-1}\left(\frac{D}{D_s} \right) \right) \tag{3.16}$$

accounts for the possibility that the electrical displacement D converges to a saturation value D_s for high field strengths. Note that in (3.14) to (3.16), ϵ_0 is the vacuum permittivity. Throughout this work, the *ideal DE* model is adopted for the electrical free-energy density.

The presented model of a cubic sheet of DE material serves to illustrate the general method employed within this chapter. Typically, more assumptions are introduced in order to specialize the model to a specific scenario and in order to eliminate degrees of freedom from the model. A very common assumption is incompressibility, i.e. the volume of the material is constant ($L_1L_2L_3 \equiv l_1l_2l_3$ or equivalently $\lambda_1\lambda_2\lambda_3 \equiv 1$). Further constraints on the model depend on the specific layout of a DE transducer and will be introduced in the following for the case of rolled DE actuators.

3.1.2. RDEA Lumped-Parameter Model 1: Three-Ring (3R)

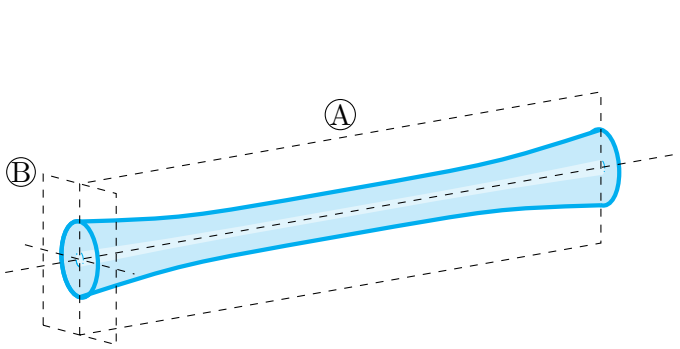

(a) 3D sketch of a deformed RDEA.

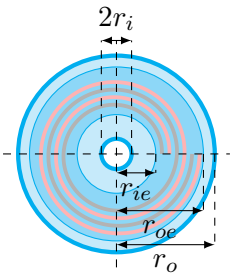

(b) Cross-section Ⓑ perpendicular to the actuation direction.

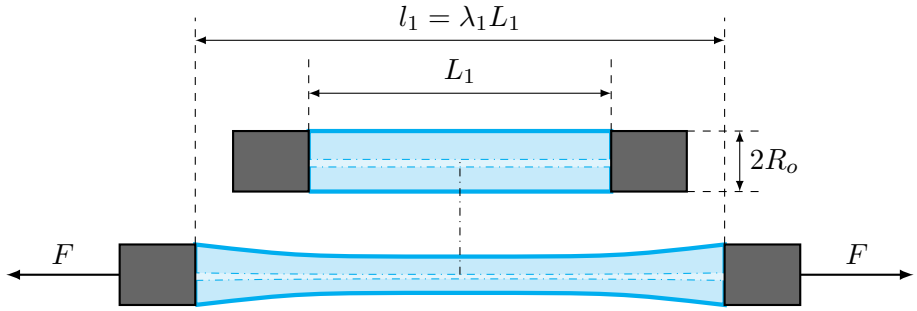

(c) Cross-section Ⓐ of a RDEA along the actuation direction (upper part: unloaded; lower part: axially loaded).

Figure 3.2.: Sketch of a RDEA cross-section deforming under an axial load (Prechtl et al. 2021a).

The goal of this section is the development of a general quasi-static model for the actuator shown in Figure 3.2, accounting for different stress distributions for the material regions where electrodes are or are not present. When no load is applied to the roll, its undeformed length along the main axis equals L_1. If an electromechanical load consisting of an axial force F and a voltage v is applied to the roll, its axial length changes to l_1 (cf. Figure 3.2c).

It shall be noted that the roll is subject to complex deformation patterns and inhomogeneities which are normally absent in conventional strip-shaped DEA membranes (Rizzello et al. 2020a). A relevant example is represented by the electric field within the rolled membrane, which possesses an inhomogeneous distribution along the cross-section due to the spiral-shaped geometry as well as due to the presence of electrode-free regions,

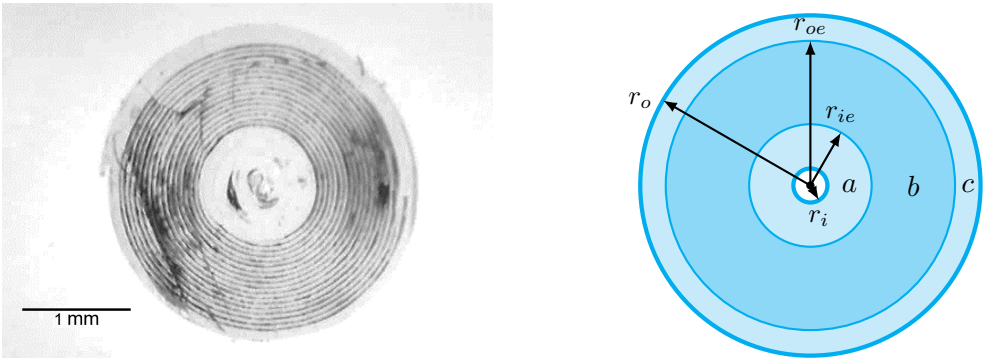

(a) Microscope picture of a RDEA specimen. (b) Sketch for the concentric cylinder model.

Figure 3.3.: Side-by-side comparison of an actual RDEA specimen with the corresponding model geometry (Prechtl et al. 2021a).

see Figure 3.3a. To simplify the mathematical treatment, we introduce the following assumptions:

Assumption 1. The roll is always under tension, i.e., $F \geq 0$ and $l_1 \geq L_1$.

Assumption 2. Because of the friction among the elastomeric layers, when the roll is axially stretched, no slipping occurs between the adjacent DE layers.

Assumption 3. Edge effects due to the clamps and electrode-free edges are assumed negligible, and thus the strain is considered as uniform along the RDEA axis.

Assumption 4. Geometrical asymmetries due to the spiral shape are assumed as negligible. As a result, the geometry of the RDEA cross-section can be well approximated by a combination of three hollow circles, as shown in Figure 3.3b. More specifically, the inner and outer hollow circles (denoted as a and c in Figure 3.3b) describe passive insulation regions, where no electrodes are present, while the intermediate hollow cylinder (denoted as b in Figure 3.3b) represents the electrically active material part.

Assumption 5. When the RDEA is activated via high voltage, it is assumed that an electric field E, directed along the radial direction, permeates the volume occupied by region b only.

Assumption 6. Passive regions a and c are modeled as three-dimensional hyperelastic solids, while active region b is modeled as a three-dimensional and electromechanically coupled hyperelastic body. The electromechanical state in each one of the three regions is modeled in a lumped-parameter way, and described through the mean values of the stress, stretch, and electric field. Radial gradients within the single regions are neglected, whereas different mean stretches and stresses are used for each region.

Assumptions 1-5 reasonably hold true for thin and slender RDEAs, obtained from a tightly rolled membrane with an unwound thickness much smaller than the roll radius. Assumption 6 allows developing the model within a lumped-parameter, rather than a finite element, mathematical framework. On the one hand, this is highly desirable for numerically efficient dynamic simulations and real-time control applications. On the other hand, the fact that we are considering three separate regions still permits to account, at least at a first order, for the effects of radial inhomogeneities within the material due to the non-negligible passive regions.

Based on Figure 3.3b, we define the following quantities: R_i (r_i) is the inner radius of

passive region a in undeformed (deformed) state; R_{ie} (r_{ie}) represents the inner radius of region b in undeformed (deformed) state; R_{oe} (r_{oe}) describes the outer radius of region b in undeformed (deformed) state; R_o (r_o) defines the outer radius of region c in undeformed (deformed) state. Note that capital letters are used to represent RDEA geometrical quantities in the undeformed configuration, while lowercase letters denote the geometry in the current configuration, respectively.

The state of deformation of each hollow cylinder is described by three principal stretches, i.e., an axial stretch λ_{1j} directed along the membrane thickness direction, a circumferential stretch λ_{2j}, and a radial stretch λ_{3j}, $j \in \{a, b, c\}$. Such principal stretches can be expressed as functions of the above defined geometric parameters, as follows:

$$\lambda_{1a} = \frac{l_1}{L_1} \qquad \lambda_{2a} = \frac{r_{ie} + r_i}{R_{ie} + R_i} \qquad \lambda_{3a} = \frac{r_{ie} - r_i}{R_{ie} - R_i} \tag{3.17}$$

$$\lambda_{1b} = \frac{l_1}{L_1} \qquad \lambda_{2b} = \frac{r_{oe} + r_{ie}}{R_{oe} + R_{ie}} \qquad \lambda_{3b} = \frac{r_{oe} - r_{ie}}{R_{oe} - R_{ie}} \tag{3.18}$$

$$\lambda_{1c} = \frac{l_1}{L_1} \qquad \lambda_{2c} = \frac{r_o + r_{oe}}{R_o + R_{oe}} \qquad \lambda_{3c} = \frac{r_o - r_{oe}}{R_o - R_{oe}}. \tag{3.19}$$

Note that stretches (3.17)-(3.19) represent averaged material quantities, and thus are independent of a specific spatial location.

In the following, we identify a number of relationships among the stretches in (3.17)-(3.19), and we impose kinematic constraints dictated by the physical problem, hence reducing the number of independent stretches needed for a complete description of the RDEA configuration.

Because the cylinders undergo the same axial elongation, the axial stretches are equal and can be represented through a single variable λ_1:

$$\lambda_{1a} = \lambda_{1b} = \lambda_{1c} = \lambda_1 = \frac{l_1}{L_1}. \tag{3.20}$$

Furthermore, the stretches defined in (3.17)-(3.19) must be such that the volumes Ω_a, Ω_b and Ω_c of the three cylinders stay constant upon stretching. Such volume preservation assumption is generally considered to hold true for elastomers, including DEs (Carpi et al. 2011). Prescribing volume preservation of the hollow cylinders leads to the following constraints:

$$\Omega_a = \pi(R_{ie}^2 - R_i^2)L_1 = \pi(r_{ie}^2 - r_i^2)l_1 \qquad \Rightarrow \qquad \lambda_{3a} = \frac{1}{\lambda_{1a}\lambda_{2a}}, \tag{3.21}$$

$$\Omega_b = \pi(R_{oe}^2 - R_{ie}^2)L_1 = \pi(r_{oe}^2 - r_{ie}^2)l_1 \qquad \Rightarrow \qquad \lambda_{3b} = \frac{1}{\lambda_{1b}\lambda_{2b}}, \tag{3.22}$$

$$\Omega_c = \pi(R_o^2 - R_{oe}^2)L_1 = \pi(r_o^2 - r_{oe}^2)l_1 \qquad \Rightarrow \qquad \lambda_{3c} = \frac{1}{\lambda_{1c}\lambda_{2c}}. \tag{3.23}$$

Finally, two additional conditions hold, which account for the fact that neighbouring regions remain in contact upon deformation. In particular, the following condition holds, which ensures that the outer radius of cylinder a coincides with the inner radius of cylinder b:

$$(R_{ie} + R_i)\lambda_{2a} + (R_{ie} - R_i)\lambda_{3a} - (R_{oe} + R_{ie})\lambda_{2b} + (R_{oe} - R_{ie})\lambda_{3b} = 0. \tag{3.24}$$

Equation (3.24) is obtained by extracting the values of r_{ie} (as a function of the stretches and the initial dimensions) for cylinder a and b respectively from (3.17) and (3.18), and equating them.

Similarly, the following relation holds, which guarantees the outer radius of b and the inner radius of c be equal:

$$(R_{oe} + R_{ie})\lambda_{2b} + (R_{oe} - R_{ie})\lambda_{3b} - (R_o + R_{oe})\lambda_{2c} + (R_o - R_{oe})\lambda_{3c} = 0. \tag{3.25}$$

In analogy to the previous case, equation (3.25) is obtained by extracting the values of r_{oe} for cylinder b and c respectively from (3.18) and (3.19), and equating them.

By collecting (3.20)-(3.25), a total of 7 conditions is obtained among the 9 stretches defined in (3.17)-(3.19). Note how (3.20)-(3.23) can be directly used to eliminate 5 out of the 9 free stretches. However, (3.24) and (3.25) cannot be uniquely solved in an analytic way, once λ_{3a}, λ_{3b}, and λ_{3c} are replaced. As a result, we treat them as independent constraints in the subsequent free-energy formulation.

For future convenience, we hereby introduce the volume ratios of the single cylinders over the total material volume:

$$\eta_a = \frac{\Omega_a}{\Omega} = \frac{\pi(R_{ie}^2 - R_i^2)L_1}{\pi(R_o^2 - R_i^2)L_1} = \frac{R_{ie}^2 - R_i^2}{R_o^2 - R_i^2} \tag{3.26}$$

$$\eta_b = \frac{\Omega_b}{\Omega} = \frac{\pi(R_{oe}^2 - R_{ie}^2)L_1}{\pi(R_o^2 - R_i^2)L_1} = \frac{R_{oe}^2 - R_{ie}^2}{R_o^2 - R_i^2} \tag{3.27}$$

$$\eta_c = \frac{\Omega_c}{\Omega} = \frac{\pi(R_o^2 - R_{oe}^2)L_1}{\pi(R_o^2 - R_i^2)L_1} = \frac{R_o^2 - R_{oe}^2}{R_o^2 - R_i^2}. \tag{3.28}$$

From (3.26)-(3.28), it directly follows that $\eta_a + \eta_b + \eta_c = 1$. Additionally, we define the electrical correction factor α_{e1} as follows

$$\alpha_{e1} = \frac{L_{1e}}{L_1}, \tag{3.29}$$

where L_{1e} represents the unstretched length of the DE electrode along the axis, with $L_{1e} \leq L_1$. Quantity α_{e1} describes the relative portion of roll axis which is covered by the electrodes.

In the following, we derive the model constitutive equations using a free-energy approach. For simplicity, we start by neglecting irreversible phenomena which are due to losses in the DE material (a more in-depth discussion on this aspect is postponed to Section 3.1.7). For a conservative and isothermal system, the internal virtual work given as the variation of the Helmholtz free-energy $\delta\Psi$ is equal to the external virtual work δW performed on the system:

$$\delta\Psi = \delta W = F\delta l_1 + v\delta q. \tag{3.30}$$

The total external work, described by the right hand-side of (3.30), consists of the sum of mechanical (first term) and electrostatic (second term) contributions. The considered generalized external forces are the force F, directed along the actuation (i.e., axial) direction, and the voltage v applied to the RDEA electrodes. The corresponding conjugated virtual displacements are the virtual actuator length variation δl_1 and the virtual charge displacement δq.

Next, we introduce the following normalized quantities:

$$\psi = \frac{\Psi}{\Omega} = \frac{\Psi}{\pi(R_o^2 - R_i^2)L_1}, \tag{3.31}$$

$$\sigma_1 = \frac{F}{\pi\left(r_o^2 - r_i^2\right)} = \frac{\lambda_1}{\pi\left(R_o^2 - R_i^2\right)}F, \tag{3.32}$$

$$N = \frac{r_{oe} - r_{ie}}{l_3} = \frac{R_{oe} - R_{ie}}{L_3}, \tag{3.33}$$

$$E = \frac{v}{l_3} = \frac{\lambda_1\lambda_{2b}N}{R_{oe} - R_{ie}}v, \tag{3.34}$$

$$D = \frac{q}{NA_{avg}} = \frac{1}{N\alpha_{e1}L_1\pi(R_{oe} + R_{ie})\lambda_1\lambda_{2b}}q, \tag{3.35}$$

where: ψ is the Helmholtz free-energy density; σ_1 is an average stress (or, more appropriately, an average force density) along the axial direction; N is the number of turns in the region b of the roll, and L_3 and l_3 are the nominal and actual thickness of a single layer (note how Assumption 2 implies that N is constant and uniquely defined, regardless of the considered configuration); E is the current averaged field strength inside the active region b, directed along the radial direction; D is the average electrical displacement, computed as the total charge on the electrodes divided by the product between number of active layers N in region b and average electrode surface area A_{avg}.

By replacing (3.20), (3.26)-(3.28), and (3.31)-(3.35) in (3.30), we obtain the following normalized version of the principle of virtual work:

$$\delta\psi = \left(\frac{\sigma_1 + \alpha_{e1}\eta_b ED}{\lambda_1}\right)\delta\lambda_1 + \alpha_{e1}\eta_b\frac{ED}{\lambda_{2b}}\delta\lambda_{2b} + \alpha_{e1}\eta_b E\delta D. \tag{3.36}$$

The Helmholtz free-energy density is modeled as follows:

$$\begin{aligned}\psi(\lambda_1, \lambda_{2a}, \lambda_{2b}, \lambda_{2c}, D, p_1, p_2) = {} & \eta_a\psi_m(\lambda_1, \lambda_{2a}) + \eta_b\psi_m(\lambda_1, \lambda_{2b}) + \eta_c\psi_m(\lambda_1, \lambda_{2c}) \\ & + \alpha_{e1}\eta_b\psi_e(D) + p_1c_1(\lambda_1, \lambda_{2a}, \lambda_{2b}) + p_2c_2(\lambda_1, \lambda_{2b}, \lambda_{2c}).\end{aligned} \tag{3.37}$$

In principle, ψ shall explicitly depend on the independent order parameters of the system only, i.e., a minimum set of stretches together with the electrical displacement. As remarked above, five out of the nine stretches defined by (3.17)-(3.19) can be eliminated by solving (3.20)-(3.23). However, since (3.24)-(3.25) cannot be solved unambiguously, we let ψ explicitly depend on the remaining four stretches λ_1, λ_{2a}, λ_{2b}, and λ_{2c}, and account for constraints (3.24)-(3.25) by introducing Lagrange multipliers p_1 and p_2 as further variables of ψ. Clearly, the electrical displacement D also represents a further independent variable on which ψ must depend.

The meaning of the different contributions to the right-hand side of (3.37) is discussed in the following. First, ψ_m denotes a generic hyperelastic free-energy density function, which depends on stretches λ_1 and λ_{2j}, $j \in \{a, b, c\}$. Therefore, the first three terms on the right-hand side of (3.37) can be interpreted as the elastic energy stored in the hollow cylinders a, b, and c, respectively. Different hyperelastic models are available from the literature to characterize ψ_m (M. Wissler et al. 2005; Suo 2010; He et al. 2009). In this work, we describe ψ_m by means of a Yeoh free-energy density (Rizzello et al. 2020a):

$$\psi_m(\lambda_1, \lambda_{2j}) = \sum_{i=1}^{3} C_{i0}\left(\lambda_1^2 + \lambda_{2j}^2 + \lambda_1^{-2}\lambda_{2j}^{-2} - 3\right)^i, \quad j \in \{a, b, c\}, \tag{3.38}$$

where C_{i0}, $i \in \{1,2,3\}$, represent constitutive material parameters. Function ψ_e models the electrostatic free-energy density of the RDEA, associated with the electric field E within active region b (Suo 2010; Rizzello et al. 2020a):

$$\psi_e(D) = \frac{D^2}{2\epsilon_0\epsilon_r}, \tag{3.39}$$

where ϵ_0 and ϵ_r are the vacuum and DE relative permittivities, respectively. The last two terms are introduced in the energy to model constraints (3.24) and (3.25), where:

$$c_1(\lambda_1,\lambda_{2a},\lambda_{2b}) = (R_{ie}+R_i)\lambda_{2a} + (R_{ie}-R_i)\frac{1}{\lambda_1\lambda_{2a}} - (R_{oe}+R_{ie})\lambda_{2b} + (R_{oe}-R_{ie})\frac{1}{\lambda_1\lambda_{2b}} = 0 \tag{3.40}$$

and

$$c_2(\lambda_1,\lambda_{2b},\lambda_{2c}) = (R_{oe}+R_{ie})\lambda_{2b} + (R_{oe}-R_{ie})\frac{1}{\lambda_1\lambda_{2b}} - (R_e+R_{oe})\lambda_{2c} + (R_e-R_{oe})\frac{1}{\lambda_1\lambda_{2c}} = 0. \tag{3.41}$$

The variation of ψ is given by

$$\begin{aligned}
&\delta\psi(\lambda_1,\lambda_{2a},\lambda_{2b},\lambda_{2c},D,p_1,p_2) \\
&\quad= \left(\eta_a\frac{\partial\psi_m(\lambda_1,\lambda_{2a})}{\partial\lambda_1} + \eta_b\frac{\partial\psi_m(\lambda_1,\lambda_{2b})}{\partial\lambda_1} + \eta_c\frac{\partial\psi_m(\lambda_1,\lambda_{2c})}{\partial\lambda_1}\right. \\
&\qquad\left. + p_1\frac{\partial c_1(\lambda_1,\lambda_{2a},\lambda_{2b})}{\partial\lambda_1} + p_2\frac{\partial c_2(\lambda_1,\lambda_{2b},\lambda_{2c})}{\partial\lambda_1}\right)\delta\lambda_1 \\
&\qquad + \left(\eta_a\frac{\partial\psi_m(\lambda_1,\lambda_{2a})}{\partial\lambda_{2a}} + p_1\frac{\partial c_1(\lambda_1,\lambda_{2a},\lambda_{2b})}{\partial\lambda_{2a}}\right)\delta\lambda_{2a} \\
&\quad + \left(\eta_b\frac{\partial\psi_m(\lambda_1,\lambda_{2b})}{\partial\lambda_{2b}} + p_1\frac{\partial c_1(\lambda_1,\lambda_{2a},\lambda_{2c})}{\partial\lambda_{2b}} + p_2\frac{\partial c_2(\lambda_1,\lambda_{2b},\lambda_{2c})}{\partial\lambda_{2b}}\right)\delta\lambda_{2b} \\
&\qquad + \left(\eta_c\frac{\partial\psi_m(\lambda_1,\lambda_{2c})}{\partial\lambda_{2c}} + p_2\frac{\partial c_2(\lambda_1,\lambda_{2b},\lambda_{2c})}{\partial\lambda_{2c}}\right)\delta\lambda_{2c} \\
&\quad + \left(\alpha_{e1}\eta_b\frac{D}{\epsilon_0\epsilon_r}\right)\delta D + c_1(\lambda_1,\lambda_{2a},\lambda_{2b})\delta p_1 + c_2(\lambda_1,\lambda_{2b},\lambda_{2c})\delta p_2.
\end{aligned} \tag{3.42}$$

The analytical expression of the partial derivatives of ψ_m, c_1, and c_2 is omitted from (3.42) for conciseness. By replacing (3.36) in (3.42), and equating the terms multiplying the same virtual displacements, we obtain the following model:

$$\begin{cases}
\sigma_1 = \eta_a\dfrac{\partial\psi_m(\lambda_1,\lambda_{2a})}{\partial\lambda_1} + \eta_b\dfrac{\partial\psi_m(\lambda_1,\lambda_{2b})}{\partial\lambda_1} + \eta_c\dfrac{\partial\psi_m(\lambda_1,\lambda_{2c})}{\partial\lambda_1} \\
\qquad + p_1\dfrac{\partial c_1(\lambda_1,\lambda_{2a},\lambda_{2b})}{\partial\lambda_1} + p_2\dfrac{\partial c_2(\lambda_1,\lambda_{2b},\lambda_{2c})}{\partial\lambda_1} - \alpha_{e1}\eta_b\epsilon_0\epsilon_r E^2 \\
0 = \eta_a\dfrac{\partial\psi_m(\lambda_1,\lambda_{2a})}{\partial\lambda_{2a}} + p_1\dfrac{\partial c_1(\lambda_1,\lambda_{2a},\lambda_{2b})}{\partial\lambda_{2a}} \\
0 = \eta_b\dfrac{\partial\psi_m(\lambda_1,\lambda_{2b})}{\partial\lambda_{2b}} + p_1\dfrac{\partial c_1(\lambda_1,\lambda_{2a},\lambda_{2c})}{\partial\lambda_{2b}} + p_2\dfrac{\partial c_2(\lambda_1,\lambda_{2b},\lambda_{2c})}{\partial\lambda_{2b}} - \alpha_{e1}\eta_b\epsilon_0\epsilon_r E^2 \\
0 = \eta_c\dfrac{\partial\psi_m(\lambda_1,\lambda_{2c})}{\partial\lambda_{2c}} + p_2\dfrac{\partial c_2(\lambda_1,\lambda_{2b},\lambda_{2c})}{\partial\lambda_{2c}} \\
0 = c_1(\lambda_1,\lambda_{2a},\lambda_{2b}) \\
0 = c_2(\lambda_1,\lambda_{2b},\lambda_{2c})
\end{cases}. \tag{3.43}$$

Model (3.43) consists of a set of 6 independent algebraic equations. Given λ_1 and E, the system can be solved for variables σ_1, λ_{2a}, λ_{2b}, λ_{2C}, p_1, and p_2. Once a solution for (3.43) is obtained, l_1, F, v can be calculated from the corresponding λ_1, σ_1, E by means of equations (3.20), (3.32), and (3.34).

To complement model (3.43), a consistent expression for the electrical capacitance of the RDEA can be found. We first express v from Ψ as follows:

$$v = \frac{\partial \Psi}{\partial q} = \Omega \frac{\partial \psi}{\partial D}\frac{\partial D}{\partial q} = \frac{L_3^2}{\epsilon_0 \epsilon_r \alpha_{e1} L_1 \pi \left({R_{oe}}^2 - {R_{ie}}^2\right)} \frac{1}{\lambda_1^2 \lambda_{2b}^2} q. \tag{3.44}$$

Based on (3.44), the electrical capacitance can be computed as follows:

$$C(\lambda_1, \lambda_{2b}) = \frac{\partial q}{\partial v} = \epsilon_0 \epsilon_r \alpha_{e1} \frac{L_1 \pi \left({R_{oe}}^2 - {R_{ie}}^2\right)}{{L_3}^2} \lambda_1^2 \lambda_{2b}^2 = C_0 \lambda_1^2 \lambda_{2b}^2, \tag{3.45}$$

where C_0 denotes the capacitance of the undeformed RDEA. Since it is mainly constructed starting from the three-ring assumption, the RDEA model described by (3.43) and (3.45) will be hereafter referred to as 3R (three-ring) model.

The presented 3R model permits to effectively describe the behavior of a slender and tightly rolled RDEA in a lumped-parameter fashion. Nonetheless, because it comes in the form of a nonlinear system of six algebraic equations (cf. (3.43)), its practical solution may turn out to be numerically expensive, especially for real-time control applications. To overcome this issue, in the following we propose two simplified versions of the RDEA model, which might suitably and conveniently replace the 3R model under specific assumptions.

3.1.3. RDEA Lumped-Parameter Model 2: One-Ring (1R)

A first possible way to simplify the 3R model comes in the form of the following additional assumption.

Assumption 7. Each one of the three rings describing the RDEA cross-section in Figure 3.3b is characterized by the same amount of circumferential stretch.

The above assumption prescribes a further degree of homogeneity within the material, whose validity might depend on several factors (a more in-depth analysis will be presented in Section 3.1.5). When considered all together, Assumptions 1-7 imply that the three rings of material can be described by a unique set of principal stretches, i.e., the RDEA uniformly deforms as a single hollow cylinder. Mathematically, Assumption 7 implies that continuity constraints (3.24)-(3.25) are replaced with the following one

$$\lambda_{2a} = \lambda_{2b} = \lambda_{2c} = \lambda_2. \tag{3.46}$$

Note that (3.46), in conjunction with relationship (3.20)-(3.23), permits to directly eliminate 7 of the 9 principal stretches, and express all of them as functions of λ_1 and λ_2 explicitly.

By repeating the energy treatment of Section 3.1.2, and replacing constraints (3.24)-(3.25) with the new condition (3.46), the normalized version of the principle of virtual work (3.30) becomes:

$$\delta\psi = \left(\frac{\sigma_1 + \alpha_{e1}\eta_b E D}{\lambda_1}\right)\delta\lambda_1 + \alpha_{e1}\eta_b \frac{E D}{\lambda_2}\delta\lambda_2 + \alpha_{e1}\eta_b E \delta D. \tag{3.47}$$

Based on (3.46), we can further reformulate the Helmholtz free-energy density in (3.37) through the following expression:

$$\psi(\lambda_1, \lambda_2, D) = \psi_m(\lambda_1, \lambda_2) + \alpha_{e1}\eta_b\psi_e(D). \tag{3.48}$$

Since in this case it is possible to solve constraints (3.46) analytically, the free-energy density can be directly expressed as a function of the independent stretches λ_1 and λ_2 only, alongside with D. Consequently, the Lagrange multipliers do no longer need to be introduced.

By differentiating (3.48), replacing it into (3.47), and repeating the steps previously outlined in Section 3.1.2, the constitutive equations of the resulting model can be computed as follows:

$$\begin{cases} \sigma_1 = \lambda_1 \dfrac{\partial \psi_m(\lambda_1, \lambda_2)}{\partial \lambda_1} - \alpha_{e1}\eta_b\epsilon_0\epsilon_r E^2 \\ 0 = \lambda_2 \dfrac{\partial \psi_m(\lambda_1, \lambda_2)}{\partial \lambda_2} - \alpha_{e1}\eta_b\epsilon_0\epsilon_r E^2. \end{cases} \tag{3.49}$$

Note that (3.49) consists of a set of two nonlinear equations, which can be uniquely solved for σ_1 and λ_2 once λ_1 and E are given as inputs. The resulting system turn out to be significantly simpler to tackle numerically, compared to (3.43).

Finally, the capacitance equation for this model can be easily derived by replacing (3.46) in (3.45), leading to:

$$C(\lambda_1, \lambda_2) = \epsilon_0\epsilon_r\alpha_{e1}\frac{L_1\pi\left({R_{oe}}^2 - {R_{ie}}^2\right)}{{L_3}^2}\lambda_1^2\lambda_2^2 = C_0\lambda_1^2\lambda_2^2. \tag{3.50}$$

By using an argument similar to the one in Section 3.1.4, the model described by (3.49) and (3.50) will be referred to as one-ring (1R) model (since this time the three rings deform as a single hollow cylinder, whose behavior follows equation (3.49)). Note how model (3.49) is formally identical to the one for strip-shaped DE membranes previously derived in Rizzello et al. 2020a.

3.1.4. RDEA Lumped-Parameter Model 3: Strongly Uniaxial (SU)

A potential way to further simplify the 3R model is outlined in the following. For a homogeneous hollow cylinder, such as the one used to approximate the shape of the RDEA, the inner and outer radii (i.e., r_i and r_o) are allowed to change independently upon loading. In contrast, if we consider a solid cylinder, its inner radius would remain unchanged, i.e., $r_i = R_i = 0$ all the time. If this is the case, it can readily be verified that the principal stretches of the resulting cylinder would also satisfy the following symmetry condition

$$\lambda_2 = \lambda_3. \tag{3.51}$$

Following this reasoning, we can assume that, if the inner passive region of the RDEA a is sufficiently thick in comparison to the active one, it will contrast changes in r_i. As a result, it can be assumed that the RDEA will deform in a similar fashion to a solid cylinder, rather than an unconstrained hollow one. This fact can be formalized with the following additional assumption.

Assumption 8. The RDEA deforms in such a way that the circumferential and radial stretches are always equal, regardless of the applied electromechanical load.

While this assumption adds on to the previous assumptions of the 1R model, and reduces the number of degrees of freedom of the problem, it provides a means for implicitly taking into account the constraint to radial electrically-induced expansions created by the passive regions. By describing the RDEA as an equivalent unconstrained DE strip, the 1R model fails to account for the large radial stiffness generated by thick inner passive regions, which expectedly leads towards a response similar to that of a full cylinder.

By considering Assumption 8 alongside with Assumptions 1-7 and incompressibility conditions (3.21)-(3.23), the following additional constraints are obtained

$$\lambda_{2a} = \lambda_{2b} = \lambda_{2c} = \lambda_2 = \frac{1}{\sqrt{\lambda_1}}. \tag{3.52}$$

Collecting together (3.20)-(3.23) and (3.52), all the 9 principal stretches can be analytically expressed as a function of λ_1 only.

By considering the new set of constraints for the stretches, we can rewrite the normalized version of the principle of virtual work (3.30) as follows:

$$\delta\psi = \left(\frac{\sigma_1 + 0.5\alpha_{e1}\eta_b E D}{\lambda_1}\right)\delta\lambda_1 + \alpha_{e1}\eta_b E \delta D, \tag{3.53}$$

while the Helmholtz free-energy density (3.37) becomes

$$\psi(\lambda_1, D) = \psi_m(\lambda_1, \lambda_2(\lambda_1)) + \alpha_{e1}\eta_b\psi_e(D), \tag{3.54}$$

where $\lambda_2(\lambda_1)$ is given by (3.52). Note that, in this case, it is possible to let the free-energy density (3.54) explicitly depend on the only independent stretch λ_1 and on D, without using additional Lagrange multipliers.

The differentiation of (3.54), together with the subsequent comparison with (3.53), allows us to obtain the following constitutive equation:

$$\sigma_1 = \lambda_1\left(\frac{\partial\psi_m(\lambda_1, \lambda_2(\lambda_1))}{\partial\lambda_1} + \frac{\partial\psi_m(\lambda_1, \lambda_2(\lambda_1))}{\partial\lambda_2(\lambda_1)}\frac{\partial\lambda_2(\lambda_1)}{\partial\lambda_1}\right) - 0.5\alpha_{e1}\eta_b\epsilon_0\epsilon_r E^2, \tag{3.55}$$

where λ_2 depends on λ_1 according to (3.52), and

$$\frac{\partial\lambda_2(\lambda_1)}{\partial\lambda_1} = -\frac{1}{2\lambda_1\sqrt{\lambda_1}}. \tag{3.56}$$

Note that λ_1 and $\lambda_2(\lambda_1)$ must be treated as independent variables when computing the partial derivatives of ψ_m in (3.55). Equation (3.55) can be readily solved for σ_1, once λ_1 and E are known. A remarkable difference between (3.55) and models (3.43) and (3.49) (i.e., 3R and 1R, respectively) is the factor 0.5 which multiplies the E-dependent Maxwell stress. This is a direct consequence of the additional kinematic constraint given by (3.52).

The capacitance can be then computed by simply replacing (3.52) into (3.45), leading to

$$C(\lambda_1) = \epsilon_0\epsilon_r\alpha_{e1}\frac{L_1\pi\left({R_{oe}}^2 - {R_{ie}}^2\right)}{{L_3}^2}\lambda_1 = C_0\lambda_1. \tag{3.57}$$

Remarkably, a linear dependency between axial stretch and capacitance is observed in this case.

Note that (3.52) is generally referred to as uniaxial condition in the literature (Rizzello et al. 2020a; M. Wissler et al. 2005). It is also simple to prove that the 1R model (3.49) satisfies condition (3.52) only when $E = 0$. In contrast, model (3.55) enforces (3.52) by construction, regardless of the applied electric field. For this reason, model (3.55) will be henceforth referred to as strongly uniaxial (SU) model.

3.1.5. Model Comparison

The main differences among the three models introduced in Sections 3.1.2-3.1.4 can be summarized as follows:

- *3R model*: it is described by equations (3.43) and (3.45), and is based on Assumptions 1-6. It is constructed by considering that the RDEA behaves as the combination of three different hollow cylinders;
- *1R model*: it is described by equations (3.49) and (3.50), and is based on Assumptions 1-7. It is constructed by considering that the RDEA behaves as a single, lumped hollow cylinder;
- *SU model*: it is described by equations (3.55) and (3.57), and is based on Assumptions 1-8. It is constructed by considering that the RDEA behaves as a single, lumped full cylinder.

In this section, we conduct a comparative study between the three models, based on realistic material and geometric parameters. The aim is to understand the conditions for which the simpler models (1R and SU) tightly approximate the behavior of the more complex one (3R). Such analysis will play a critical role for the selection of the best RDEA model, which accounts for an optimal trade-off between complexity and numerical accuracy.

To perform the above mentioned comparison, the following case study is considered. The material parameters are chosen according to the experimental investigation in Rizzello et al. 2020a, namely $C_{10} = 241\,\text{kPa}, C_{20} = -33.2\,\text{kPa}, C_{30} = 20.1\,\text{kPa}$, and $\epsilon_r = 2.8$, while $L_3 = 48\ \mu\text{m}$ and $\alpha_{e1} = 1$ for simplicity. Three different rolls are considered in this study, each one of them representing different extreme cases, by properly selecting the values of the radii as follows: hollow inner core, corresponding to $R_i = 0.86\,\text{mm}$, $R_{ie} = 0.88\,\text{mm}$, $R_{oe} = 1.76\,\text{mm}$, and $R_o = 1.8\,\text{mm}$; active inner core, corresponding to $R_i = 0\,\text{mm}$, $R_{ie} = 0.088\,\text{mm}$, $R_{oe} = 1.76\,\text{mm}$, and $R_o = 1.8\,\text{mm}$; passive inner core, corresponding to $R_i = 0\,\text{mm}$, $R_{ie} = 0.81\,\text{mm}$, $R_{oe} = 1.76\,\text{mm}$, and $R_o = 1.8\,\text{mm}$. By analyzing those configurations, we can understand the role of the inner core in determining the RDEA electromechanical response.

The response of each one of those cases is first simulated by means of the 3R model. The results are shown in Figure 3.4a for the hollow core RDEA, in Figure 3.4b for the active core RDEA, and in Figure 3.4c for the passive core RDEA, respectively. Each picture shows the simulated cross-section in three different situations, i.e., unloaded ($\lambda_1 = 1$, $v = 0\,\text{V}$) on the left-hand side, mechanically loaded ($\lambda_1 = 1.75$, $v = 0$ V) on the upper-right hand side, and electromechanically loaded ($\lambda_1 = 1.75$, $v = 3.5\,\text{kV}$) on the lower-right hand side. In the case of the RDEA with hollow core, shown in Figure 3.4a, the mechanical loading

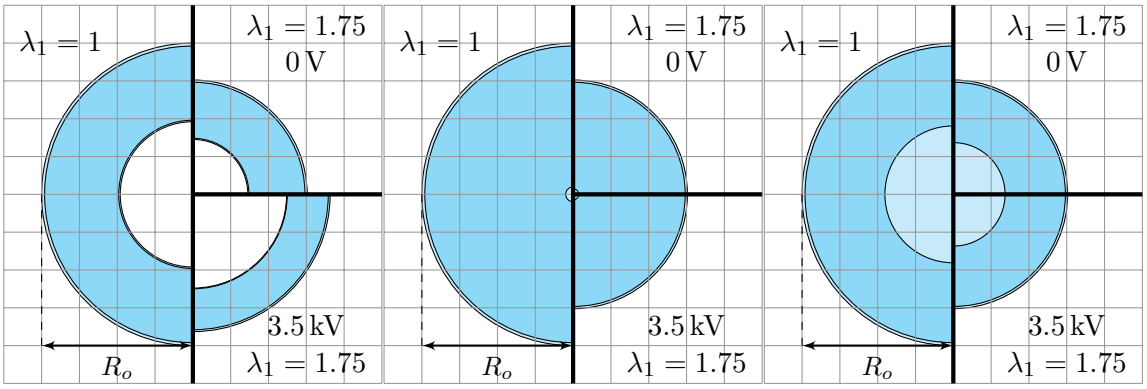

(a) Hollow core. (b) Active core. (c) Passive core.

Figure 3.4.: Comparison of cross-sections for different geometries in loaded/unloaded configurations and at different voltages according to the 3R model. For this comparison, the radii are chosen as follows: hollow core (a) corresponds to $R_i = 0.86\,\text{mm}$, $R_{ie} = 0.88\,\text{mm}$, $R_{oe} = 1.76\,\text{mm}$, and $R_o = 1.8\,\text{mm}$; active core (b) corresponds to $R_i = 0\,\text{mm}$, $R_{ie} = 0.088\,\text{mm}$, $R_{oe} = 1.76\,\text{mm}$, and $R_o = 1.8\,\text{mm}$; passive core (c) corresponds to $R_i = 0\,\text{mm}$, $R_{ie} = 0.81\,\text{mm}$, $R_{oe} = 1.76\,\text{mm}$, and $R_o = 1.8\,\text{mm}$ (Prechtl et al. 2021a).

leads to a reduction in both inner and outer radii, while the application of an electric field causes both of them to expand again. This behavior is somehow expected, and also similar to the one of conventional strip-shaped DE membranes.

When we consider a RDEA whose active part covers almost the entirety of the material volume, as in Figure 3.4b, some differences with respect to the previous case are visible. When stretching the RDEA, the outer radius contracts significantly. However, when an electric field is also applied, the RDEA geometry remains practically unchanged. In this scenario, as both R_i and R_{ie} tend to 0, circumferential and radial stretches λ_2 and λ_3 are equal in each portion of the RDEA, as a consequence of constraints (3.24) and (3.25), and the roll behaves as a single solid uniaxial cylinder. A similar behavior is also observed in case of the RDEA with passive core, reported in Figure 3.4c. Based on such analysis, we understand that the parameter which determines the RDEA deformation kinematics upon electrical activation is mostly the inner radius R_i, rather than the size of inner passive region $R_{ie} - R_i$. In particular, the closer R_i to 0, the less the RDEA is free to undergo an unconstrained deformation when subject to an electric field.

A quantitative comparison between 3R and the two simplified models is then performed, in order to understand the domain of validity of the additional assumptions which are introduced. The numerical comparison is shown in Figure 3.5 for the hollow core case (corresponding to Figure 3.4a), in Figure 3.6 for the active core case (corresponding to Figure 3.4b), and in Figure 3.7 for the passive core case (corresponding to Figure 3.4c), respectively. Each plot shows the circumferential stretches λ_2 (upper part) and the axial stresses σ_1 (center part) computed as a function of λ_1 for the three models, together with the stress errors e_{σ_1} between the simplified and 3R model (lower part), for both $v = 0$ V (left-hand side) and $v = 3.5\,\text{kV}$ (right hand-side) cases. In all the cases, the 3R

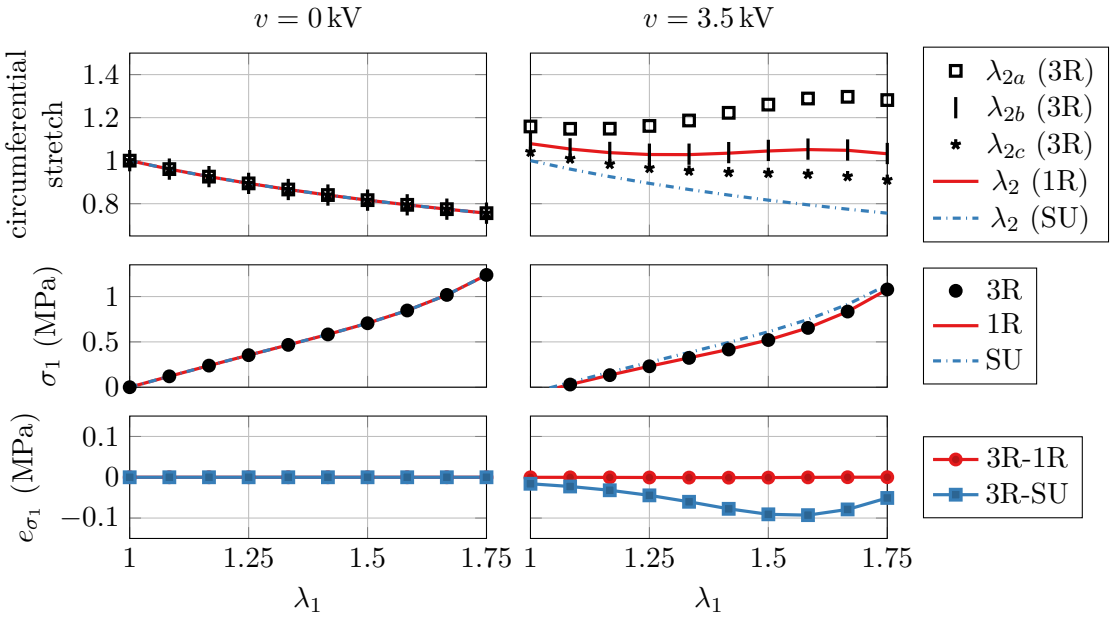

Figure 3.5.: Model comparison, hollow core (Prechtl et al. 2021a).

model results are represented in black, while the 1R and SU are depicted in blue and red, respectively.

First, we analyze the results corresponding to the hollow core case, shown in Figure 3.5. For the $v = 0$ V case, all models have coincident circumferential stretches. This result is somehow expected, since uniaxiality is assumed to hold for a pure tensile test conducted on a thin and slender roll. As a result, also the stresses predicted by the three models are practically identical. When comparing the curves computed for $v = 3.5\,\mathrm{kV}$, on the other hand, a remarkable difference is observed among the three models. First, one can note how the circumferential stretches deviate remarkably. The 1R model provides an accurate approximation of the circumferential stretch of the active region of the 3R model, i.e., λ_{2b}, reasonably due to the small thickness of the passive regions. The stretch predictions of the SU model, on the other hand, significantly deviate from the 3R model. As a direct result, the stress predicted by the 1R model approximates much more tightly the stress of the 3R, while the SU model is affected by a maximum error of 0.1 MPa over a range of 1 MPa. The situation appears remarkably different if we analyze the results for the RDEA with active core, shown in Figure 3.6. The plots for the case $v = 0$ V appear identical to Figure 3.5, thus implying that uniaxiality still holds true. Quite remarkably, the results obtained for $v = 3.5\,\mathrm{kV}$ suggest a strong agreement between 3R and SU models, both in terms of circumferential stretches and stress. As expected, the 1R model turns out to be inaccurate in this case. Note how this model predicts a circumferential expansion, which cannot occur in reality. If such an expansion occurred, the stretches in the central portion of the core would in fact tend to infinity. Such a misprediction of λ_2 leads to stress errors on the order of 0.1 MPa. Qualitatively similar results are also obtained for the RDEA with the passive core, shown in Figure 3.7. The only difference is given by the value of the stress error for the 1R model, which has now a peak value on the order of 0.055 MPa.

The conducted analysis confirms that parameter R_i plays a crucial role for determining

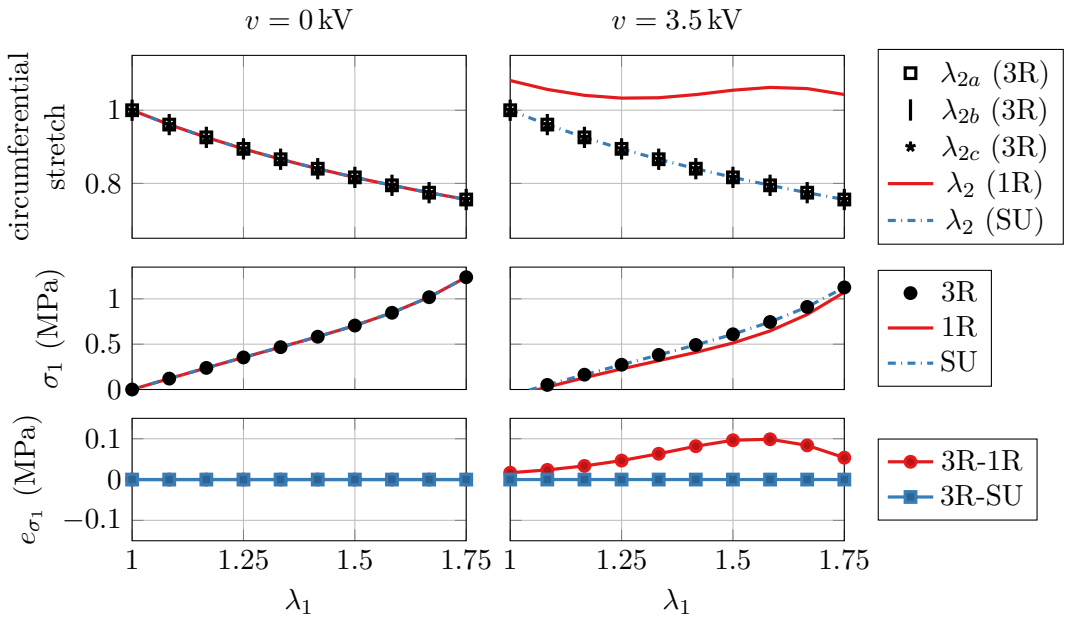

Figure 3.6.: Model comparison, active core (Prechtl et al. 2021a).

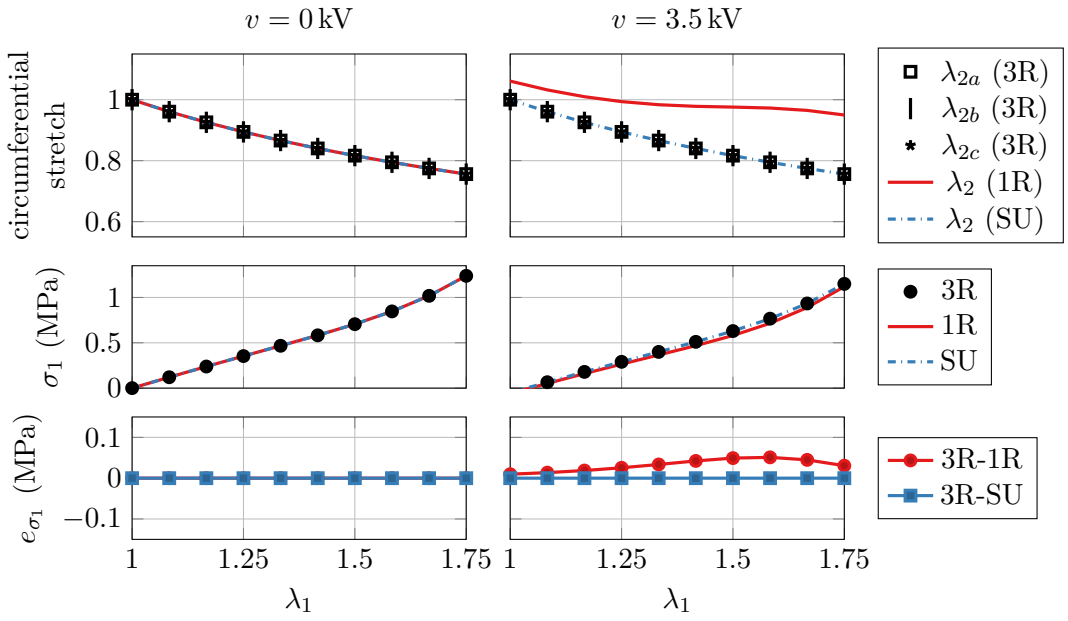

Figure 3.7.: Model comparison, passive core (Prechtl et al. 2021a).

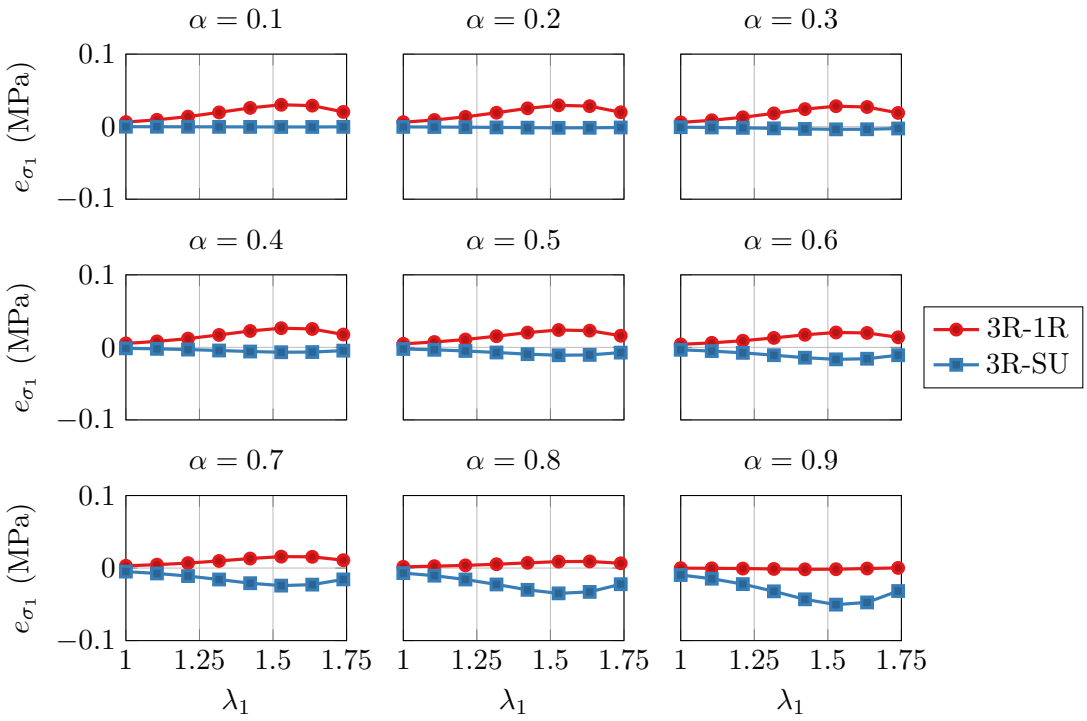

Figure 3.8.: Deviations of the predicted average stress σ_1 of the two simplified models (1R in red, SU in blue) in comparison to the 3R model, for a sweep of $R_i \in \{0.1, 0.2, \ldots, 0.9\} \cdot R_{ie}$ (Prechtl et al. 2021a).

whether the 3R model can or cannot be approximated by the 1R and SU models. For very small values of R_i, ideally close to 0, the SU behaves identically to the 3R. In this case, the SU model represents then the best trade-off between complexity and accuracy. For values of R_i closer to R_o, the 3R model is better approximated by the 1R one, which can then be considered as the optimal modeling choice. Furthermore, the value of R_{ie} seems not to play a relevant role in determining the stretch behavior, but has an effect on the absolute stress error. Naturally, the conducted analysis only covers extreme cases, and several intermediate situations could manifest for other geometries. As an example, Figure 3.8 shows the force error computed by choosing $R_i \in \{0.1, 0.2, \ldots, 0.9\} \cdot R_{ie}$, by considering $R_{ie} = 0.6\,\text{mm}$, $R_{oe} = 1.21\,\text{mm}$, and $R_o = 1.33\,\text{mm}$. As it can be seen, decreasing R_i induces a smooth transition from the 1R behavior to the SU one, with values in between for which none of the approximations accurately describe the 3R model.

As a final note, it is remarked that the proportions of the reference geometry used for the passive core case (i.e., the one shown in Figure 3.4c and Figure 3.7) closely resemble those of the real-life RDEA prototypes investigated in the evaluation section. Therefore, the SU model represents the most appropriate choice for the analysis of the prototypes under investigation.

3.1.6. Alternative Formulation using Coenergy

The above derivations of constitutive equations for the electromechanical behavior of RDEAs followed an approach of contrasting the Helmholtz free energy stored in the system to the work performed by external forces (mechanical and electrical) by using the principle of virtual works. According to (3.31), this free energy $\Psi(l_1, q)$ is given as

$$\Psi = \pi L_1 (R_o^2 - R_i^2)\psi, \tag{3.58}$$

where ψ is given according to the chosen model variant from the previous sections. By choosing the SU model, we substitute (3.54) and obtain

$$\begin{aligned}\Psi(l_1, q) &= \pi L_1 (R_o^2 - R_i^2) \left[\psi_m(\lambda_1, \lambda_2(\lambda_1)) + \alpha_{e1}\eta_b\psi_e(D)\right]_{\lambda_1 = \frac{l_1}{L_1}, D = \frac{q}{NA_{avg}}} \\ &= \pi (R_o^2 - R_i^2) \sum_{i=1}^{3} C_{i0} \left(\frac{l_1^2}{L_1} + 2\frac{L_1^2}{l_1} - 3\right)^i + \frac{q^2}{2\epsilon_0\epsilon_r\eta_b \frac{R_o^2 - R_i^2}{L_3^2}\alpha_{e1}\pi l_1}.\end{aligned} \tag{3.59}$$

This free energy considers the length l_1 and the charge q as independent variables. Generally, an energy-based formulation of the actuator dynamics offers several advantages, as it lends itself to complex system modeling using Lagrangian mechanics (cf. Section 4.1). Nevertheless, in practical scenarios usually the voltage v_{DE} instead of the charge q is controlled by means of an external high-voltage amplifier. Therefore, in order to use the model in an energy-based framework, we would like to consider the voltage v_{DE} as an independent variable instead of the charge.

Care has to be taken when performing this exchange of variables, since simply substituting $v_{DE} = \frac{\partial \Psi(l_1, q)}{\partial q} = \frac{q}{C}$ into Ψ and computing the actuator force as the gradient of the resulting term gives incorrect results. The formally correct way of performing this exchange of variables while preserving physically meaningful gradients is by constructing a coenergy using the Legendre transform (Zia et al. 2009).

In formal terms, the goal is to construct a new potential $\Psi_C(l_1, v_{DE})$, while ensuring that its gradient with respect to the unchanged variable l_1 remains unchanged (and equivalent to the actuator force F_{DE}):

$$\frac{\partial \Psi_C(l_1, v_{DE})}{\partial l_1} = \frac{\partial \Psi(l_1, q)}{\partial l_1} =: F_{DE}, \tag{3.60}$$

while considering that the new variable v_{DE} and the old variable q are related by

$$v_{DE} = \frac{\partial \Psi(l_1, q)}{\partial q} = \frac{q}{\epsilon_0 \epsilon_r \eta_b \frac{R_o^2 - R_i^2}{L_3^2} \alpha_{e1} \pi l_1} = \frac{q}{C(l_1)}. \tag{3.61}$$

This can be achieved by means of the Legendre transform:

$$\begin{aligned}
\Psi_C(l_1, v_{DE}) &\coloneqq \left[\Psi(l_1, q) - \frac{\partial \Psi(l_1, q)}{\partial q} q \right]_{q = C(l_1) v_{DE}} \\
&= \pi (R_o^2 - R_i^2) \sum_{i=1}^{3} C_{i0} \left(\frac{l_1^2}{L_1} + 2 \frac{L_1^2}{l_1} - 3 \right)^i - \left[\frac{q^2}{2 \epsilon_0 \epsilon_r \eta_b \frac{R_o^2 - R_i^2}{L_3^2} \alpha_{e1} \pi l_1} \right]_{q = C(l_1) v_{DE}} \\
&= \pi (R_o^2 - R_i^2) \sum_{i=1}^{3} C_{i0} \left(\frac{l_1^2}{L_1} + 2 \frac{L_1^2}{l_1} - 3 \right)^i - \epsilon_0 \epsilon_r \eta_b \frac{R_o^2 - R_i^2}{L_3^2} \alpha_{e1} \pi l_1 \frac{v_{DE}^2}{2}.
\end{aligned} \tag{3.62}$$

It can be readily verified that (3.62) satisfies (3.60). As will be shown in Section 3.2, the SU model is capable of accurately describing the actuation behavior of many practical RDEA specimens. Hence, Equation (3.62) can be seen as the quintessential summary of this RDEA modeling chapter. It describes a voltage-dependent (co-)energy, capturing all static contributions to the actuator force (being the gradient of the coenergy w.r.t. the actuator length), suitable for inclusion in a Lagrangian modeling framework.

3.1.7. Inclusion of Hysteretic Effects

All the modeling considerations in Sections 3.1.2-3.1.5 are based on the assumption that the DE behaves as a reversible transducer, i.e., no dissipations occur in the material. This reflects in the considered form (3.30) of the principle of virtual work, which states that all the work done on the DE is stored as free-energy. In reality, however, DE transducers exhibit irreversibilities due to friction occuring within the material. Depending on loading conditions, transducers can exhibit either static or dynamic hysteresis, or a combination of both.

To account for those effects in the material response, a modified version of the principle of virtual work for irreversible systems can be used, which is expressed through the following inequality:

$$\delta \Psi \leq \delta W = F \delta l_1 + v \delta q. \tag{3.63}$$

The inequality sign in (3.63) implies that only part of the work done on the RDEA is stored in the material as free-energy, while the rest is dissipated as heat.

As proven in Rizzello et al. 2020a, using the irreversible version of the principle of virtual work (3.63) as a starting point leads to an additive component $\sigma_{1,irr}$ in the stress σ_1. The

additional irreversible component of the stress $\sigma_{1,irr}$ must be chosen in such a way that inequality (3.63) is satisfied for every system trajectory. The equation for the stress hence takes the following general form:

$$\sigma_1 = \sigma_{1,rev} + \sigma_{1,irr}, \tag{3.64}$$

where the reversible component of the stress $\sigma_{1,rev}$ is given by the expressions for σ_1 in (3.43), (3.49), or (3.55), depending on the considered RDEA model.

In the following, the third case is (SU model according to (3.55)) discussed in detail. After normalizing and then considering (3.55), (3.63) is rewritten as follows:

$$\dot{\psi} \leq \frac{\sigma_1 + 0.5\alpha_{e1}\eta_b E D}{\lambda_1}\dot{\lambda}_1 + \alpha_{e1}\eta_b E \dot{D}. \tag{3.65}$$

The inequality sign in (3.65) reflects the fact that only a part of the work done on the system is stored as free-energy, while the rest is dissipated as heat, in agreement with the second law of thermodynamics. We further assume that in the irreversible case, the free-energy density function depends on some further internal variables $\xi_{p,j}, j = 1, \ldots, J$ and $\xi_{v,l}, l = 1, \ldots, L$:

$$\psi = \psi(\lambda_1, D, \xi_{p,1}, \ldots, \xi_{p,J}, \xi_{v,1}, \ldots, \xi_{v,L}). \tag{3.66}$$

In particular, internal variables $\xi_{p,j}$ and $\xi_{v,l}$ reflect the internal material dissipation due to rate-independent and rate-dependent hysteresis, respectively.

By computing $\dot{\psi}$ based on (3.66) and substituting into (3.65), we get

$$\left(\frac{\sigma_1 + 0.5\alpha_{e1}\eta_b E D}{\lambda_1} - \frac{\partial\psi}{\partial\lambda_1}\right)\dot{\lambda}_1 + \left(\alpha_{e1}\eta_b E - \frac{\partial\psi}{\partial D}\right)\dot{D} - \sum_{j=1}^{J}\frac{\partial\psi}{\partial\xi_{p,j}}\dot{\xi}_{p,j} - \sum_{l=1}^{L}\frac{\partial\psi}{\partial\xi_{v,l}}\dot{\xi}_{v,l} \geq 0. \tag{3.67}$$

One possible choice for a set of constitutive equations satisfying this inequality is

$$\begin{cases} \sigma_1 = \lambda_1\dfrac{\partial\psi}{\partial\lambda_1} - \dfrac{1}{2}\alpha_{e1}\eta_b E D + \eta_{v,0}\dot{\lambda}_1 & \\ E = \dfrac{1}{\epsilon_0\epsilon_r}D & \\ \dot{\xi}_{p,j} = \left|\dot{\lambda}_1\right|\dfrac{k_{p,j}}{\eta_{p,j}}(\lambda_1 - \xi_{p,j}) & , j = 1, \ldots, J \\ \dot{\xi}_{v,l} = \dfrac{k_{v,l}}{\eta_{v,l}}(\lambda_1 - \xi_{v,l}), & , l = 1, \ldots, L \end{cases}, \tag{3.68}$$

with ψ given as

$$\begin{aligned} \psi = \sum_{i=1}^{3} C_{i0}\left(\lambda_1^2 + \frac{2}{\lambda_1} - 3\right)^i + \alpha_{e1}\eta_b\frac{D^2}{2\epsilon_0\epsilon_r} \\ + \sum_{j=1}^{J} k_{p,j}\left[\lambda_1 - \xi_{p,j}\left(1 + \log\frac{\lambda_1}{\xi_{p,j}}\right)\right] + \sum_{l=1}^{L} k_{v,l}\left[\lambda_1 - \xi_{v,l}\left(1 + \log\frac{\lambda_1}{\xi_{v,l}}\right)\right]. \end{aligned} \tag{3.69}$$

If we select the free parameters as $k_{p,j} \geq 0$, $k_{v,l} \geq 0$, $\eta_{p,j} > 0$, $\eta_{v,l} > 0$, and $\eta_{v,0} \geq 0$, it can readily be shown that (3.68)-(3.69) satisfy (3.67) for any system trajectory. We start by computing partial derivatives of ψ:

$$\frac{\partial \psi}{\partial D} = \alpha_{e1}\eta_b \frac{D}{\epsilon_0 \epsilon_r}, \tag{3.70a}$$

$$\frac{\partial \psi}{\partial \xi_{p,j}} = -\sum_{j=1}^{J} k_{p,j} \log \frac{\lambda_1}{\xi_{p,j}}, \tag{3.70b}$$

$$\frac{\partial \psi}{\partial \xi_{v,j}} = -\sum_{l=1}^{L} k_{v,l} \log \frac{\lambda_1}{\xi_{v,l}}. \tag{3.70c}$$

Substituting equations (3.70) and (3.68) into (3.67), we obtain:

$$\sum_{j=1}^{J} \left|\dot{\lambda}_1\right| \frac{k_{p,j}^2}{\eta_{p,j}} (\lambda_1 - \xi_{p,j}) \log \frac{\lambda_1}{\xi_{p,j}} + \sum_{l=1}^{L} \frac{k_{v,l}^2}{\eta_{v,l}} (\lambda_1 - \xi_{v,l}) \log \frac{\lambda_1}{\xi_{v,l}} \geq 0. \tag{3.71}$$

Equation (3.71) is true for non-negative $\eta_{p,j}, \eta_{v,l}$ and positive λ_1, $\xi_{p,j}$ and $\xi_{v,l}$. The logarithmic terms can become negative only if $\lambda_1 < \xi_{p,j}$ or $\lambda_1 < \xi_{v,l}$, and in that case the corresponding pre-multiplier is negative as well, therefore the result stays non-negative.

The numbers J and L are freely chosen non-negative integers specifying the desired model order, i.e., the number of Lion and Maxwell branches, respectively. The number of those elements can be tuned in order to replicate hysteresis shapes of various complexity. In the sequel, we focus on the special case of (3.68)-(3.69) in which $J = L = 1$, resulting in the following constitutive equations:

$$\begin{cases} \sigma_1 = \underbrace{2\left(\lambda_1^2 - \frac{1}{\lambda_1}\right) \sum_{i=1}^{3} i C_{i0} \left(\lambda_1^2 + \frac{2}{\lambda_1} - 3\right)^{i-1}}_{\sigma_m} \\ \qquad\qquad \underbrace{-\frac{1}{2}\alpha_{e1}\eta_b \epsilon_0 \epsilon_r E^2}_{\sigma_e} \\ \qquad\qquad + \underbrace{k_p(\lambda_1 - \xi_p)}_{\sigma_p} + \underbrace{k_v(\lambda_1 - \xi_v)}_{\sigma_v} + \underbrace{\eta_{v,0}\dot{\lambda}_1}_{\sigma_{v0}} \\ \dot{\xi}_p = \left|\dot{\lambda}_1\right| \frac{k_p}{\eta_p} (\lambda_1 - \xi_p) \\ \dot{\xi}_v = \frac{k_v}{\eta_v} (\lambda_1 - \xi_v) \end{cases}. \tag{3.72}$$

Figure 3.9 shows a representation of Equation (3.72) as a mechanical circuit. The hyperelastic behavior $\sigma_m(\lambda_1)$ is accounted for by a nonlinear spring. An adjustable spring represents the dependence on the applied electric field $\sigma_e(E)$. The rate-independent hysteresis contribution $\sigma_p(\lambda_1, \xi_p)$ is modeled using a nonlinear dashpot in series with a linear spring (as proposed in Lion 1997), while the viscoelastic contributions $\sigma_v(\lambda_1, \xi_v)$ (Maxwell model) and $\sigma_{v0}(\dot{\lambda}_1)$ (linear dashpot) describe the rate-dependent part of the hysteresis. The newly introduced parameters $k_{p,j}, k_{v,l}$ can then be interpreted as spring stiffness, while $\eta_{p,j}$, $\eta_{v,l}$ and $\eta_{v,0}$ denote the damping coefficients of the dashpot elements.

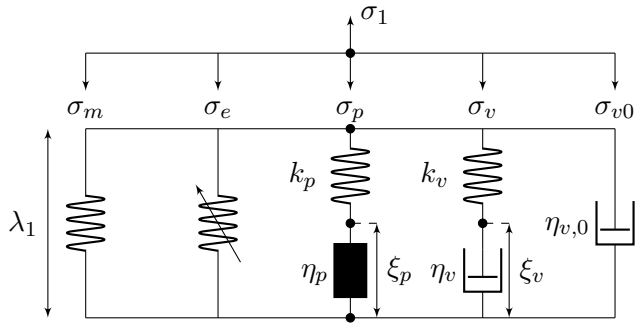

Figure 3.9.: Equivalent mechanical circuit of the proposed model, shown in the configuration $J = L = 1$ (Prechtl et al. 2023).

In order to better understand the hysteretic behavior of the three different elements, in Figure 3.10 the stress response for different stretch profiles is visualized over time and over the stretch, for the configuration $J = L = 1$ depicted in Figure 3.9. On the one hand, both the rate-independent Lion element (shown in blue) and the Maxwell element (shown in red) exhibit an initial loading curve, and they show a similar asymptotic stress response during loading and unloading. On the other hand, the response of the Maxwell element decays to zero as soon as the stretch rate goes to zero, while the Lion element maintains a constant stress. Furthermore, the stress amplitude of the Lion element stays constant, while the Maxwell elements' response scales with the stretch rate. As expected, the linear damping element exhibits a response proportional to the stretch rate.

3.2. Experimental Validation

The proposed model of RDEAs has been evaluated in several experimental campaigns. The first campaign focused on validating the model at quasistatic conditions, aiming to confirm the prediction capabilities across different specimen geometries and at different voltages. A second round of experiments was conducted in order to extend the model validation towards a broader frequency range, focusing on hysteretic behavior at very low (0.1 Hz) and low frequencies (2.5 Hz). Both campaigns were conducted on similar test setups with RDEA specimens at different stages of development regarding the manufacturing process. Therefore, the specimen properties and test setup details are introduced separately at the start of each section.

3.2.1. Blocking Forces, Tensile Tests and Capacitance Measurements

Experimental Setup

A picture of the experimental setup used to characterize the electromechanical response of the RDEA specimens is shown in Figure 3.11. One end of the RDEA is attached to an Aerotech ACT165DL Linear Actuator, whose displacement can be directly controlled by the user, while its other end is connected to a FUTEK LSB303 Load cell (25 lb) which allows recording the force during deformation. At the same time, a TREK 5/80 High Voltage Amplifier permits to supply an arbitrary high voltage to the RDEA electrodes. Only for the experiments in which no voltage is applied, an additional electrical capacitance

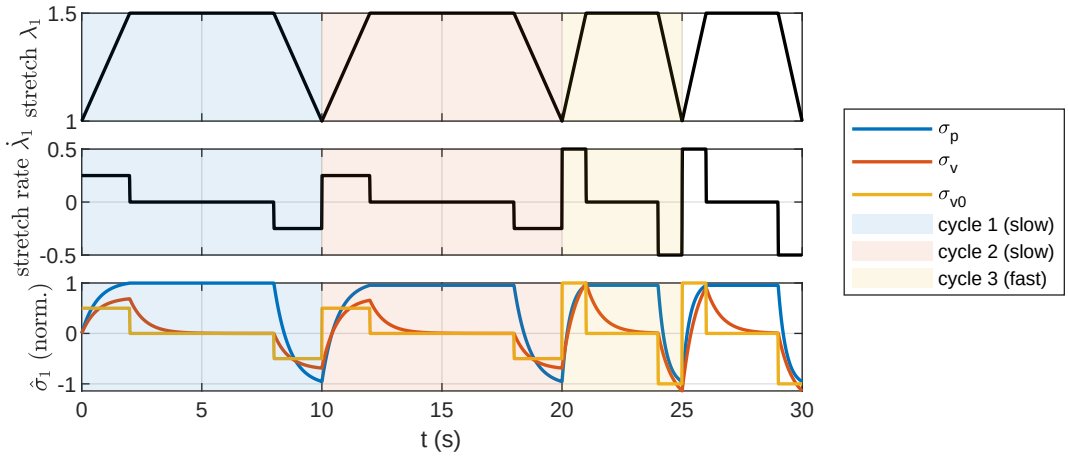

(a) Stretch, stretch rate and normalized stress response over time.

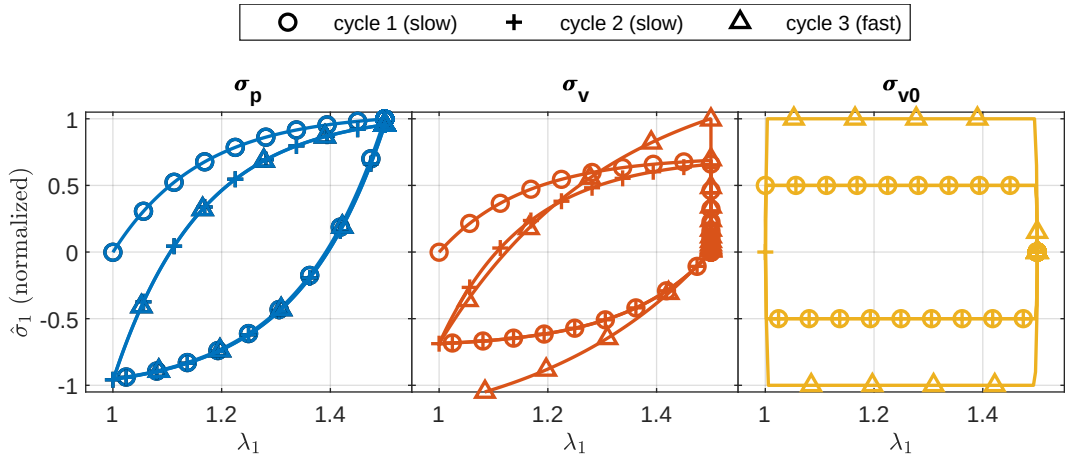

(b) Normalized stress over stretch response.

Figure 3.10.: Typical dynamic stress contributions for a stretch profile with piecewise-constant stretch rates.

measurement is also performed by means of a Rohde & Schwarz HAMEG HM8118 LCR Bridge. Real-time DAQ is implemented via a NI-9149 CompactRIO FPGA chassis with appropriate IO-modules, while data post-processing is performed in LabView and Matlab on a Windows Computer.

The experimental setup described above permits to implement different types of characterization experiments, i.e., force-displacement evaluation with different constant voltage values applied, blocking force tests under cycling voltage input, and capacitance-displacement behavior characterization. All the experiments will be conducted by considering typical ranges of displacement, voltage, and frequency which are relevant for our intended soft robotic application.

Results and Discussion

For model validation purpose, three silicone-based RDEA samples are designed and manufactured. The corresponding geometric data are reported in Table 3.1, and consist of

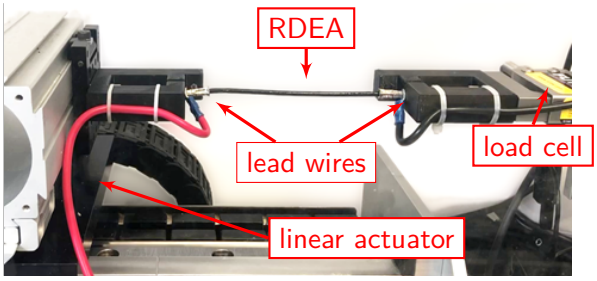

Figure 3.11.: Experimental setup used to characterize the RDEA specimens (adapted from Prechtl et al. 2021a).

Table 3.1.: Physical specimen properties and fixed model parameters.

	Specimen				
	1	2	3		
L_1	34	34	91	mm	initial length in actuation direction
L_2	58	99	58	mm	initial length in rolling direction (pre-roll)
L_3	48	48	48	µm	single-membrane initial thickness
L_{1e}	29	29	86	mm	length of membrane region with applied electrode along the actuation direction
L_{p1}	10	10	10	mm	electrode-free membrane length at the start of rolling
L_{2e}	38	76	38	mm	length of membrane region with applied electrode along the rolling direction
ϵ_r		2.8			material relative permittivity
ϵ_0		8.854		$\mathrm{pF\,m^{-1}}$	vacuum permittivity

a short and thin roll (specimen 1), a short and thick roll (specimen 2), and a long and thin roll (specimen 3). The meaning of the goemetric parameters reported in Table 3.1 is further clarified in Figure 3.12. Since our aim is to predict the behavior of all the specimens by means of a unique set of material parameters, the full spectrum of considered geometries provides a challenging validation platform for our model.

Next, we need to choose one of the three models among the ones discussed in Section 3.1. To this end, we use the procedure outlined in Appendix A to estimate the rolls radii on the basis of the unwound membrane geometries reported in Table 3.1. The computed values are reported in Table 3.2. By inspecting the obtained values for the radii, and recalling the comparative analysis presented in Section 3.1.5, we conclude that the considered specimens can be consistently and conveniently described by the SU model.

The geometric parameters are all assumed to be measurable, and thus their nominal design values will be used in the following. The material parameters consist of the Yeoh coefficients C_{i0}, $i \in \{1,2,3\}$, the permittivity ϵ_r, the viscoelastic model order L and parameters k_{vl}, η_{vl} and η_{v0}, with $l \in \{1,\dots,L\}$. For the given silicone, the permittivity is assumed to be known and equal to the datasheet value (Wacker 2023), i.e., $\epsilon_r = 2.8$. The

Table 3.2.: Geometric model parameters calculated from unwound membrane dimensions.

	Specimen				
	1	2	3		
R_i	0.000	0.000	0.000	mm	inner radius of region a
R_{ie}	0.600	0.600	0.600	mm	inner radius of region b
R_{oe}	1.206	1.615	1.206	mm	inner radius of region c
R_o	1.326	1.732	1.326	mm	outer radius of region c

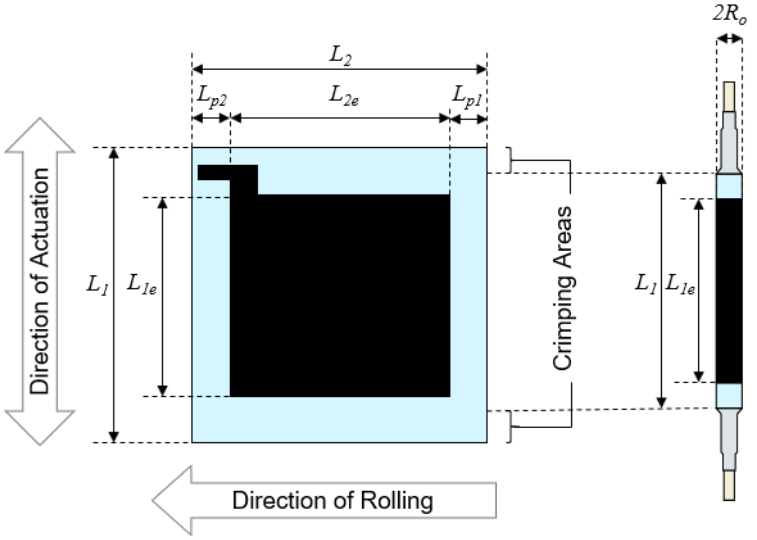

Figure 3.12.: Geometric parameters of the RDEA, before rolling (left-hand side) and after rolling (right-hand side) (Prechtl et al. 2021a).

Table 3.3.: Calibrated model parameters (RDEA model).

	242		
C_{i0}	−69	kPa	Yeoh model parameters
	47		
J	0		Lion model order
L	1		viscoelastic model order
k_{v1}	8271	kPa	viscoelastic model spring stiffness
η_{v1}	86	kPa s	viscoelastic model serial damping
η_{v0}	0	kPa s	viscoelastic model parallel damping

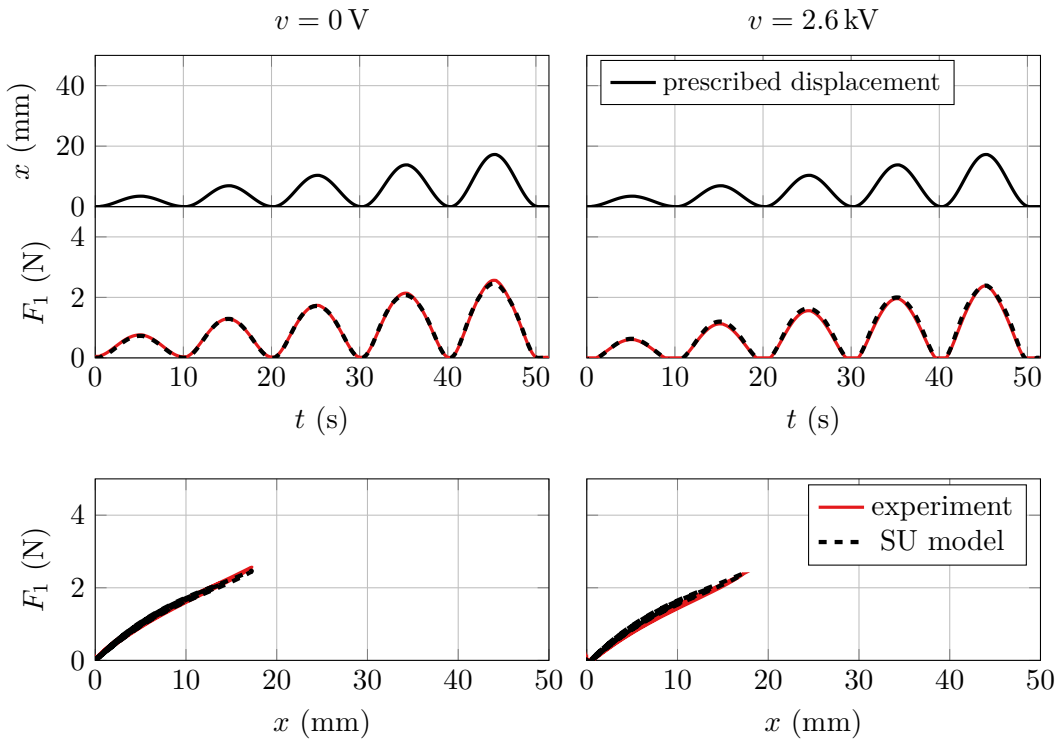

Figure 3.13.: Tensile test for measurements of specimen 1 (solid red line), and model prediction (dashed black line), validation based on SU model. Displacement waveform: sinewave with amplitude modulated by a ramp (solid black line), frequency of 0.1 Hz (Prechtl et al. 2021a).

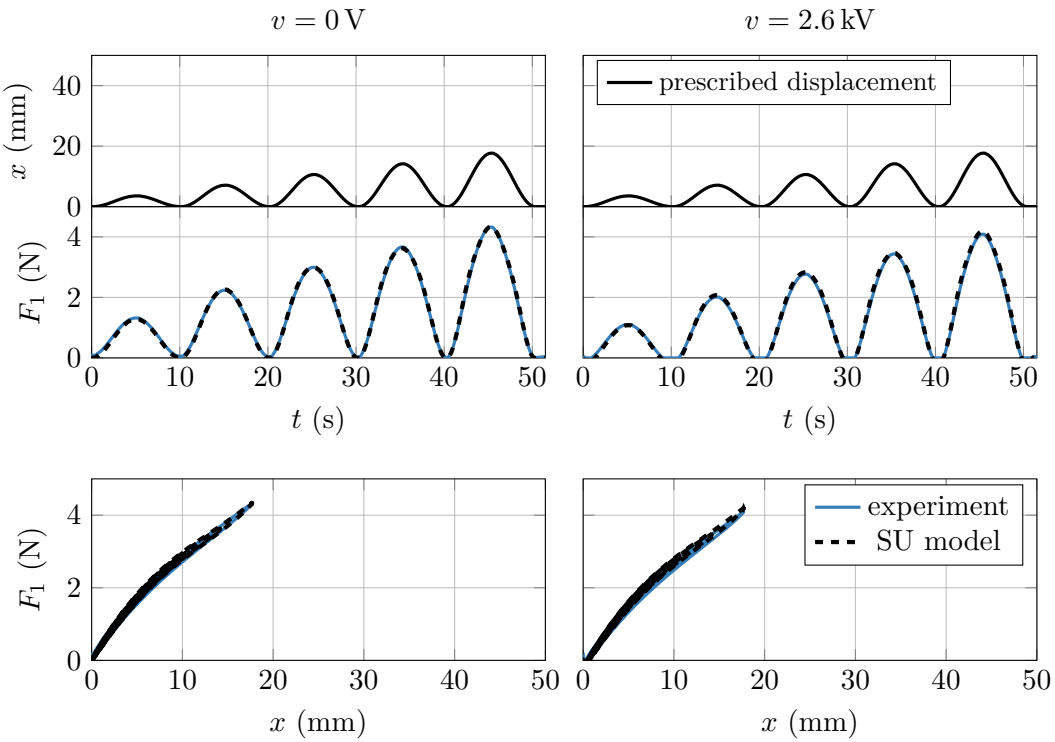

Figure 3.14.: Tensile test for measurements of specimen 2 (solid blue line), and model prediction (dashed black line), calibration based on SU model. Displacement waveform: sinewave with amplitude modulated by a ramp (solid black line), frequency of 0.1 Hz (Prechtl et al. 2021a).

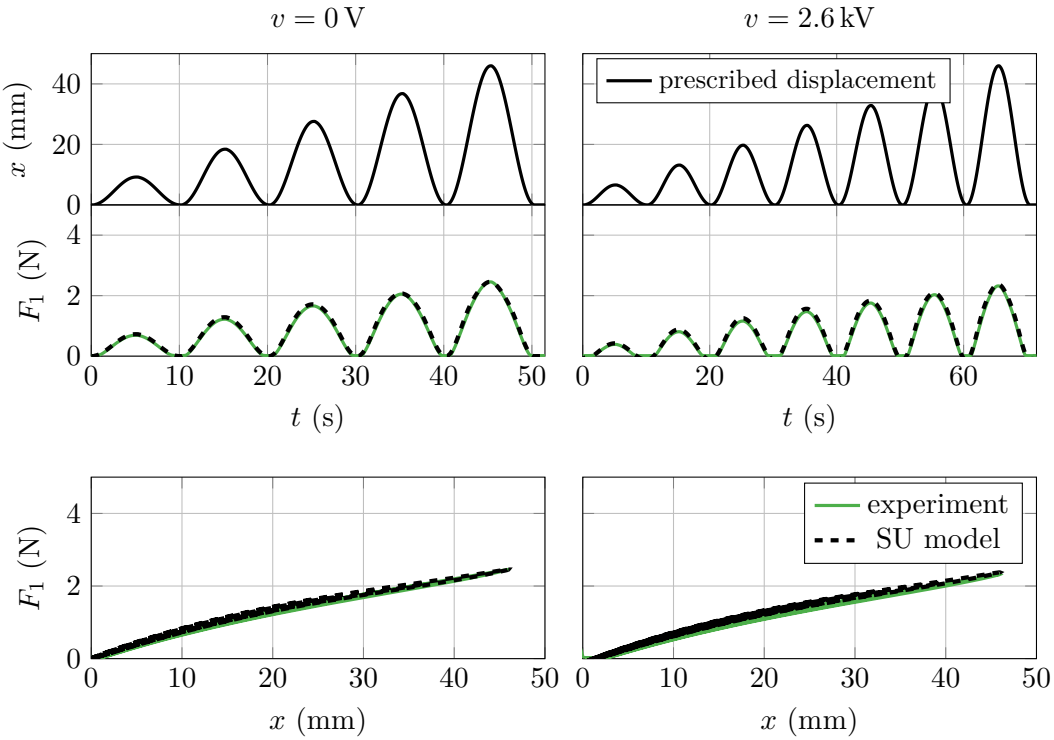

Figure 3.15.: Tensile test for measurements of specimen 3 (solid green line), and model prediction (dashed black line), validation based on SU model. Displacement waveform: sinewave with amplitude modulated by a ramp (solid black line), frequency of 0.1 Hz (Prechtl et al. 2021a).

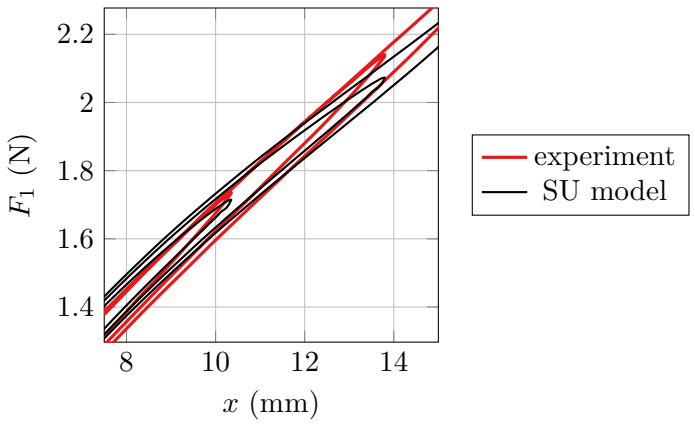

Figure 3.16.: Expanded view based on the force-displacement curve shown in Figure 3.13 (sample 1, $v = 0\,\mathrm{kV}$), to highlight the ability of the model in predicting viscoelastic hysteresis. For better visualization, the line style of the model prediction has been modified with respect to Figure 3.13 (Prechtl et al. 2021a).

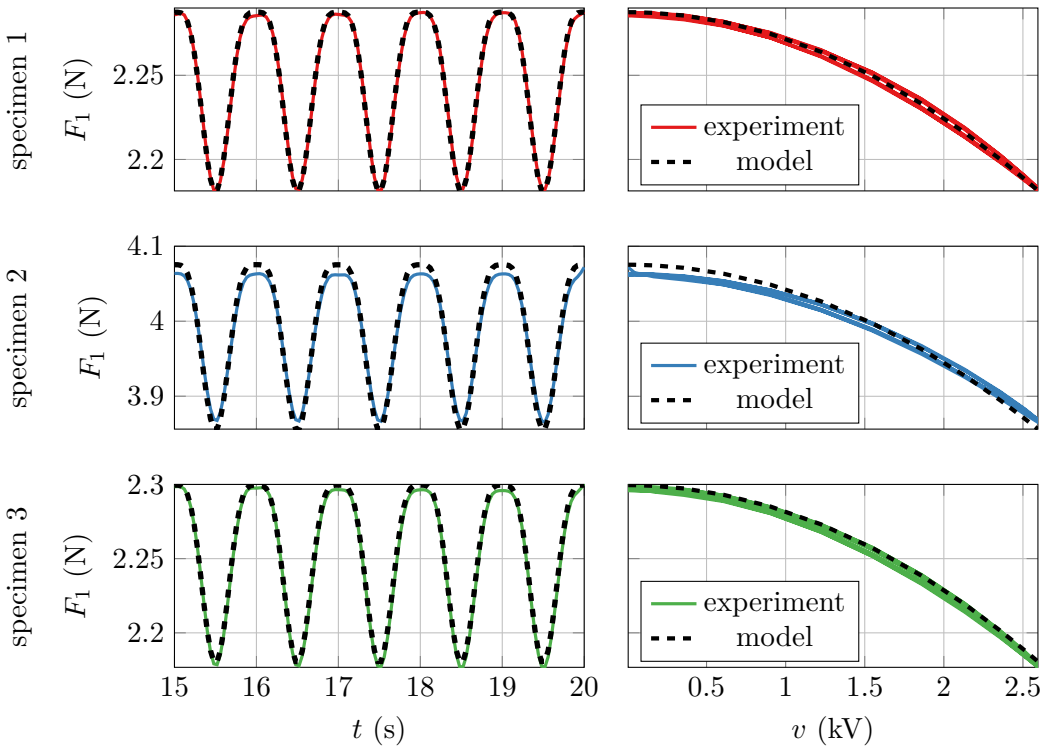

Figure 3.17.: Blocking force comparison, validation based on SU model (left-hand side: force over time, right-hand side: force over voltage). Voltage waveform: sinewave ranging from 0 kV to 2.6 kV, frequency of 1 Hz (Prechtl et al. 2021a).

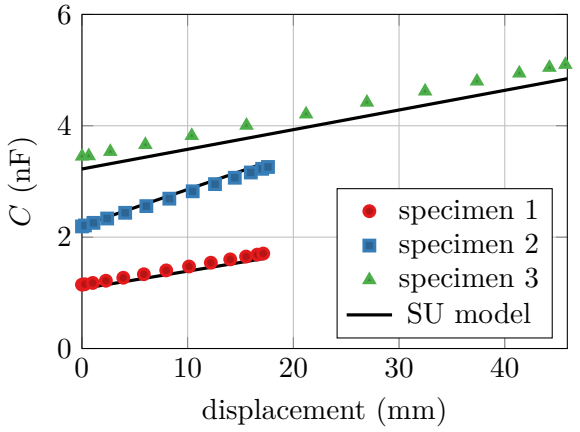

Figure 3.18.: Capacitance comparison, validation based on SU model. Displacement waveform: sinewave with amplitude modulated by a ramp (solid black line), frequency of 0.1 Hz (Prechtl et al. 2021a).

Table 3.4.: Numerical accuracy of the model predictions. The maximum relative errors are computed with respect to the maximum experimentally observed force or capacitance, respectively.

Type of experiment	Voltage	Spec.	Max. rel. error (%)
Tensile tests (predicted force) cf. Figures 3.13 to 3.15	0 V	1	3.20
		2	5.19
		3	4.81
	2.6 kV	1	6.13
		2	5.41
		3	6.53
Blocking Force cf. Figure 3.17	0 V to 2.6 kV	1	0.90
		2	0.99
		3	1.18
Capacitance cf. Figure 3.18	0 V	1	4.99
		2	0.78
		3	5.16

remaining Yeoh and viscoelastic parameters, on the other hand, need to be calibrated on the basis of the conducted experiments.

The first set of experiments is performed by deforming the three specimens at different stretch levels up to $\lambda_1 = 1.5$ with a frequency of 0.1 Hz. Each tensile experiment is repeated twice, by considering constant voltage values of $v = 0\,\text{kV}$ and $v = 2.6\,\text{kV}$. The results of such characterization experiments are reported in Figure 3.13 for specimen 1 (solid red line), in Figure 3.14 for specimen 2 (solid blue line), and in Figure 3.15 for specimen 3 (solid green line). Each plot shows the applied displacement profile and the corresponding membrane force signals over time (upper part), as well as the force-displacement characteristic curve (lower part), for both the $v = 0\,\text{kV}$ (left-hand side) and $v = 2.6\,\text{kV}$ (right-hand side) cases.

All the unknown model parameters are calibrated on the basis of the experimental data for specimen 2 (Figure 3.14), by means of a nonlinear optimization algorithm based on the Nelder-Mead search method (similarly to Rizzello et al. 2020a, details are omitted for conciseness). The resulting set of calibrated parameters is reported in Table 3.3. These parameters are then used to predict the behavior of the remaining experiments. The resulting model predictions are also shown in Figures 3.13-3.15 (dashed black lines). As it can be observed, the model allows reproducing the behavior with remarkable accuracy, for all the geometries and voltage. In addition to that, note how the hysteretic effects due to viscoelasticity are also well reproduced, as highlighted by the expanded view for sample 1 ($v = 0\,\text{kV}$), reported in Figure 3.16. For better visualization, the line style of the model prediction in Figure 3.16 has been modified with respect to Figure 3.13. Small deviations may be due to manufacturing tolerances, as well as unmodeled local effects, but nevertheless their effect is overall negligible. It is remarked that, due to the linear structure

of the purely viscoelastic stress model chosen for this round of experiments ($J = 0$, $L = 1$, cf. Table 3.3), we are not able to accurately describe the complex RDEA hysteresis in a wider frequency range. Nevertheless, the adopted model still provides a first order description of the hysteretic trend, while an in-depth investigation of hysteresis behavior at different frequencies is given in Section 3.2.2. Further investigations revealed how the SU model well predicts the RDEAs force-displacement response for higher voltage values as well, up to 4 kV. However, since the material tends to undergo frequent breakdowns if higher voltages are used, further results will be omitted. A quantitative evaluation of the deviation between experiments and model, expressed in terms of maximum relative error, is reported in Table 3.4. As it can be seen, the maximum error is always smaller or equal than 4.81% for $v = 0$ kV, and always smaller or equal than 6.53% for $v = 2.6$ kV, thus confirming the accuracy of our approach. The ability of the SU model in predicting the behavior of specimens with very different geometries confirms the validity of the modeling assumptions outlined in Section 3.1.

Next, three additional experiments are conducted in which the RDEA position is kept fixed at a stretch of $\lambda_1 = 1.5$, while the voltage is cycled sinusoidally from 0 kV to 2.6 kV at a frequency of 1 Hz, and the resulting blocking force is measured. The resulting data are shown in Figure 3.17 for all the three specimens (solid red line for specimen 1, solid blue line for specimen 2, solid green line for specimen 3). Based on the parameters calibrated in the previous step, corresponding model predictions are evaluated and plotted in Figure 3.17 (dashed black lines). Overall, the model is capable of reproducing the behavior of the three geometries with satisfactory accuracy. In particular, relative errors smaller or equal than 1.18% are computed for all those experiments, as reported in Table 3.4. The highest deviations are observed for specimen 2, but the accuracy still appears satisfactory.

Finally, the ability of the model in predicting the electrical capacitance is investigated. To this end, the capacitance-displacement curves of the three specimens are evaluated based on the same experiments conducted in Figure 3.13-3.15, and reported in Figure 3.18 (solid red line for specimen 1, solid blue line for specimen 2, solid green line for specimen 3). Due to technical limitations of the used LCR meter, the capacitance measurements can be only performed at $v = 0$ kV. The corresponding capacitance values predicted by the model are also reported on the same picture (dashed black lines). The capacitance estimations are solely based on known geometry and permittivity, thus no further parameter calibration is performed when generating the simulation results in Figure 3.18. A remarkable agreement is observed also in this case, both in terms of the initial capacitance and the resulting trend. Small deviations, visible especially for specimen 3, could be due to manufacturing inaccuracies as well as parasitic effects. The latter assumption is supported by the fact that the experimental curve for specimen 3 has the same slope as the simulated one, but is characterized by a higher offset, which could be well explained by an added constant parasitic capacitance. Nevertheless, the overall accuracy is high, with errors always smaller or equal than 5.16% for all the specimens, as reported in Table 3.4. The linear dependency between capacitance and displacement, which is both predicted theoretically (cf. (3.57)) and confirmed experimentally, suggests the possibility of effectively implementing self-sensing schemes in the future, which will allow developing a sensorless control architecture for RDEAs.

Based on the results reported in Figures 3.13-3.18, it can be concluded that the proposed SU model represents the optimal choice when dealing with the considered class of core-free RDEAs, as it accurately captures the experimental results while requiring minimum

Table 3.5.: Physical specimen properties and fixed model parameters.

L_1	68	mm	initial length in actuation direction
L_3	48	µm	single-membrane initial thickness
R_i	0	mm	radius of inner air gap
R_o	1.54	mm	outer actuator radius
α_{e1}	0.74		relative electrode coverage of the membrane material in actuation direction
η_b	0.72		relative electrode coverage of the membrane material in rolling direction
ϵ_r	2.8		material relative permittivity
ϵ_0	8.85	$\mathrm{pF\,m^{-1}}$	vacuum permittivity

Table 3.6.: Calibrated model parameters.

	Maxwell-Lion	Lion	Visco LF	Visco HF	Visco	
	210.66	210.52	210.86	210.86	−464.35	kPa
C_{i0}	−21.94	−21.67	−19.70	−19.70	6.80	
	14.78	14.71	13.63	13.63	13.43	
k_p	93.48	107.50	-	-	-	kPa
η_p	15.11	13.62	-	-	-	kPa s
k_v	$15.88 \cdot 10^{-6}$	-	$28.07 \cdot 10^{-9}$	82.96	$4.11 \cdot 10^{3}$	kPa
η_v	107.07	-	186.40	$7.75 \cdot 10^{-3}$	$15.43 \cdot 10^{3}$	MPa s
$\eta_{v,0}$	856.16	-	$53.53 \cdot 10^{3}$	$35.69 \cdot 10^{-3}$	$2.86 \cdot 10^{3}$	Pa s

computational cost.

3.2.2. Experiments at different Loading Frequencies

Experimental Setup

The experimental setup for this campaign has the same basic arrangement as shown in Figure 3.11 and is used to record tensile test data from the RDEA specimen under consideration. The setup consists of a linear motor (Aerotech ANT-25LA) following a prescribed displacement profile over time, and a load cell (ME-Systeme ME KD40s 10N/XP00) mounted in series to the specimen under test. Two wires, contacted to the electrically conductive clamps on both sides of the specimen, are used to apply high voltage, while care is taken to tie the wires to the test setup in such a way that any disturbance of the force measurement is minimized.

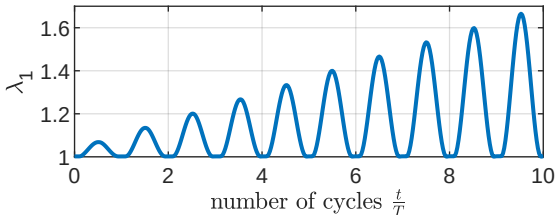

Figure 3.19.: Typical stretch profile during tensile test (Prechtl et al. 2023).

Results and Discussion

For this work, a specimen was selected for evaluation with the geometrical dimensions and physical properties listed in Table 3.5. Tensile tests using a sinusoidal displacement profile with increasing amplitude were conducted at 0.1 Hz and 2.5 Hz, respectively, with 0 V, 2.5 kV and 3 kV of applied voltage. In postprocessing, the recorded displacements $l_1(t_k)$, forces $F(t_k)$, and voltages $v(t_k)$ are normalized to stretch λ_1, electric field strength E and mechanical stress σ_1 as follows(Prechtl et al. 2021a):

$$\lambda_1 = \frac{l_1}{L_1}, \qquad E = \sqrt{\lambda}_1 \frac{v}{L_3}, \qquad \sigma_{1,exp} = F \frac{\lambda_1}{\pi(R_o^2 - R_i^2)}. \tag{3.73}$$

The trajectory of the prescribed stretch is given in Figure 3.19 and the resulting stress trajectories σ_1 are depicted in Figure 3.20. The stated expression for the electric field strength accounts for the fact that the voltage is kept constant during deformation, and thus an increase of the electric field strength for increasing stretch is observed.

The raw force-displacement data was recorded at a sample rate of 1 kHz. In order to reduce measurement noise and speed up the calibration process, the raw measurement data was zero-phase filtered and the data rate was reduced such that approx. 33 samples per actuation cycle were preserved, resulting in a 292× reduction for the 0.1 Hz experiments and 12× reduction for the 2.5 Hz experiments. For the parameter identification procedure, a candidate set of parameters was evaluated by simulating the proposed model in MATLAB using `ode15s` solver and comparing the resulting mechanical stress $\sigma(\lambda_1, \dot{\lambda}_1)$ against the recorded values using MATLAB function `goodnessOfFit` with the NRMSE error metric (normalized root mean squared error).

Recall that in Section 3.1.7, we decided to choose a model of orders $J = L = 1$, i.e. one Lion and one Maxwell branch. The dataset is split into calibration and validation groups of equal size, as outlined in Figure 3.20. After identifying model parameters on the calibration set, the response is compared to both calibration and validation experiments. Figure 3.20 shows the predicted stress over time, while Figure 3.21 and Figure 3.22 compare the stress-over-stretch hysteresis between model and experiment (only last cycle shown for visual clarity). An initial observation is that the mechanical stress predicted by the calibrated model matches the experimental data very closely on an absolute scale.

Furthermore, it is interesting to compare solely the "non-reversible contributions" to the stress. This is achieved by computing $\sigma_{irr} = \sigma_1 - \sigma_m - \sigma_e$, where $\sigma_m(\lambda_1)$ and $\sigma_e(\lambda_1)$ are estimated using the model equations and σ_1 is either the experimentally measured stress, or the model predicted stress. The resulting quantities are plotted versus the stretch λ_1 in Figure 3.23, allowing us to visually evaluate to which extent the hysteretic behavior is matched by the model, including inner loops. We observe a good fit of the hysteresis

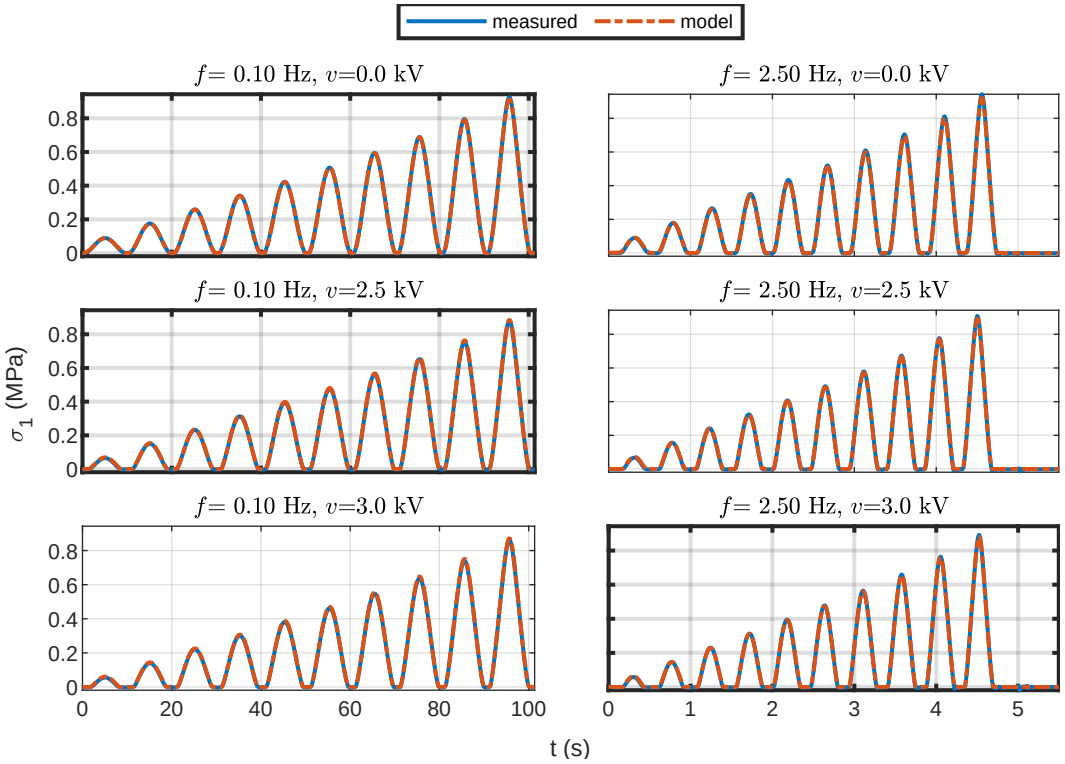

Figure 3.20.: Comparison of experimental measurements and model predictions (stress over time). The constant applied voltage varies between rows, while the actuation frequency varies between left and right columns. Bold outlines indicate calibration experiments, normal outlines indicate validation data (adapted from Prechtl et al. 2023).

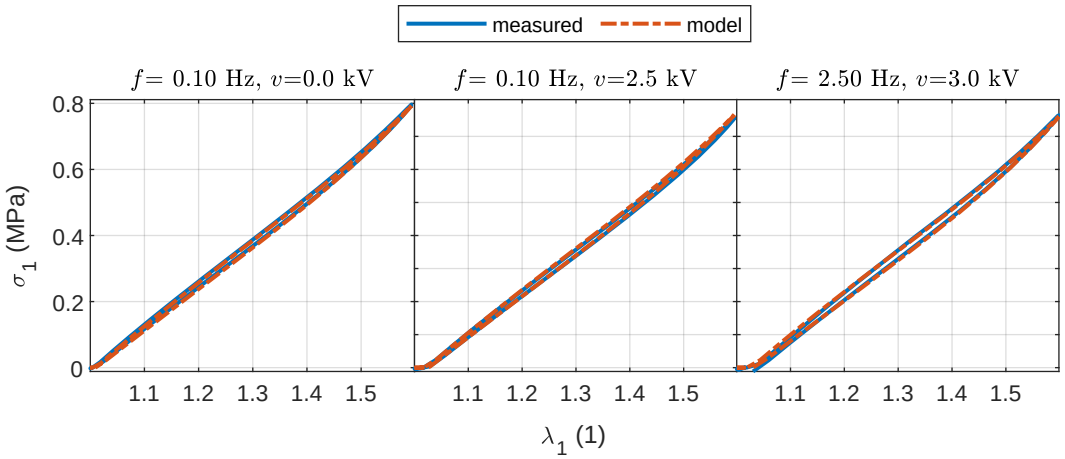

Figure 3.21.: Stress over stretch (last cycle, calibration dataset), comparison between calibrated model and experiment (adapted from Prechtl et al. 2023).

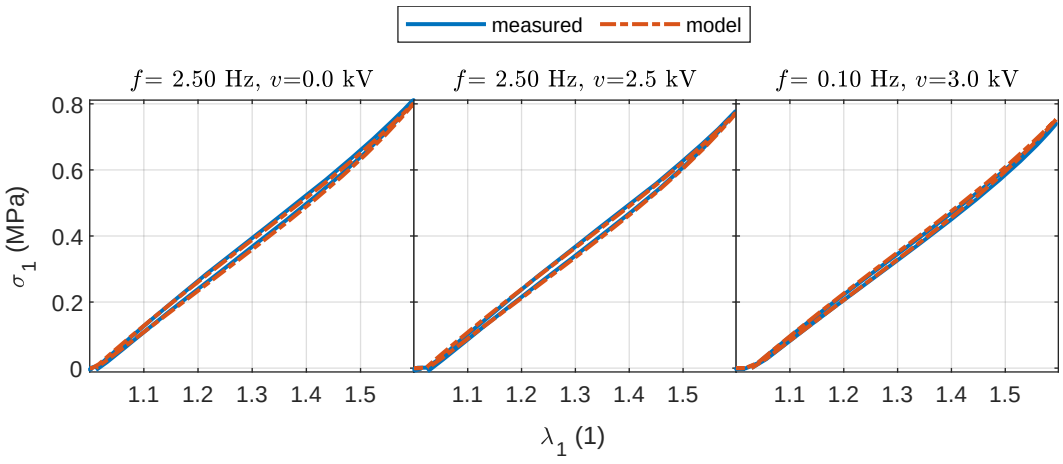

Figure 3.22.: Stress over stretch (last cycle, validation dataset), comparison between calibrated model and experiment (adapted from Prechtl et al. 2023).

shape, taking into account the low model order. It is expected that some of the remaining differences to the measured stress could be addressed by including more Lion branches in the model ($J \gg 1$).

In order to better assess the benefits of the combined Maxwell-Lion model, four other model configurations were calibrated, and the root mean square error (RMS) was calculated on the complete dataset, as listed in Table 3.7. "Maxwell-Lion" describes a hysteresis with both rate-independent and rate-dependent contributions, featuring both a Lion-Branch and a Maxwell-Branch ($J = L = 1$) as well as a linear dashpot in parallel. The model configuration "Lion" omits both the linear dashpot and Maxwell branch, and thus only accounts for rate-independent hysteresis. Finally, the "Visco" configuration omits the Lion branch and relies on the linear dashpot and Maxwell branch, and describes a rate-dependent hysteresis which vanishes in quasi-static conditions. In Table 3.7, three versions of the "Visco" configuration were calibrated with different datasets. While the "Visco" configuration used the same calibration dataset as the Maxwell-Lion and Lion models, "Visco LF" (low frequency) used only experiments at actuation frequencies of 0.1 Hz, and "Visco HF" (high frequency) was calibrated on 2.5 Hz. An unsurprising result is that the most general model version with 5 parameters also achieves the lowest error as measured by the RMS metric. Interestingly though, the second-best accurate model is the "Lion" version with just two parameters, followed by the "Visco" configuration and its two sister variants. Another interesting observation is that the "Visco LF" model produces very large errors compared to the other models, thus failing in adequately describing the full dataset.

These observations lead to the conclusion that the experimentally observed stress-stretch hysteresis is largely rate-independent at frequencies up to 2.5 Hz, and while a rate-dependent model can be calibrated to match the selected experiments, it fails at higher frequencies. Similar results would be expected for the "Visco HF" model if one would conduct tensile tests at larger frequencies. On the other hand, even one rate-independent Lion-branch is enough to capture the majority of the experimentally observed hysteresis, and a small rate-dependent contribution can be considered with the addition of the viscoelastic components (Maxwell-Lion). This conclusion is also supported by Figure 3.23,

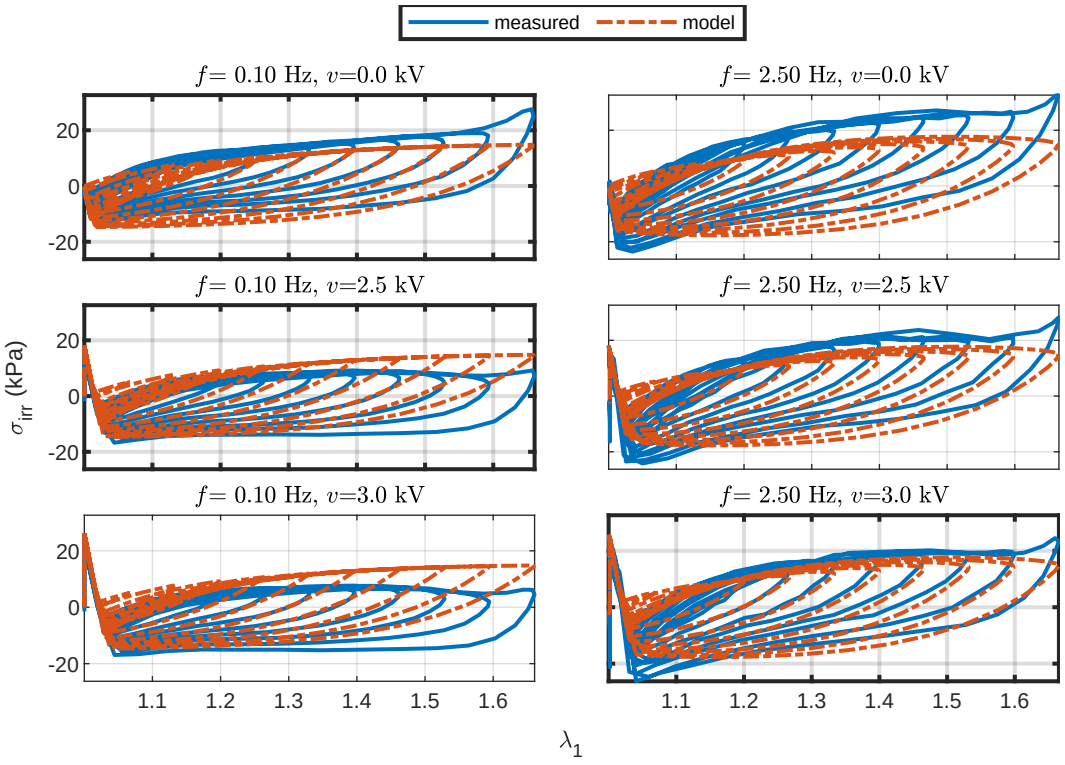

Figure 3.23.: Irreversible components of the stress after calibration. The constant applied voltage varies between rows, while the actuation frequency varies between left and right columns. Bold outlines indicate calibration experiments, normal outlines indicate validation data (adapted from Prechtl et al. 2023).

Table 3.7.: Performance comparison between different model configurations.

Model name	J	L	Number of parameters	RMS (kPa)
Maxwell-Lion	1	1	5	4.24
Lion	1	0	2	4.38
Visco LF	0	1	3	71.77
Visco HF	0	1	3	5.22
Visco	0	1	3	5.12

where the irreversible hysteretic component of the stress exhibits only small (although non-zero) changes with increasing actuation rate.

3.3. Summary: RDEA Modeling

In this chapter, a physics-based model of rolled dielectric elastomer actuators has been developed and validated on experimental data. The model covers the influence of actuator geometry, material properties and electromechanical coupling, and in addition is able to describe static as well as dynamic hysteresis while maintaining thermodynamic consistency. The results in regard to the hysteresis modeling indicate a structurally more accurate description of the material dynamics than a standard (i.e., Maxwell-based) viscoelastic model. In Rizzello 2024, a systematic, efficient and fast parameter identification algorithm has been developed for the here-presented SU model.

In addition, its computational efficiency allows using it for advanced real-time control algorithms both for the actuator itself and as a building block in models of more complex mechatronic and robotic structures. In fact, the SU model will be used in Section 4.1 to model the actuator behavior in a planar soft robotic structure. A recent work by Kunze et al. 2024 uses the here-presented results to model and analyze different operating modes of a three-dimensional soft robotic actuator composed of a circular battery of RDEAs.

4. Modeling of DE-actuated Soft Robotic Structures

In this chapter, a physics-based electromechanical model of the "T-Platform" soft robotic module is derived, describing the dynamic relationship between input voltages of the actuators and system pose over time. As for the rolled actuators, this model should enable physical insight into the operating principle and thus serve as a tool for design and performance optimization of physical prototypes. In contrast to phenomenological modeling approaches, it will therefore be essential to consider the internal forces of the structure and the physical principles governing them. Furthermore, the model will be essential to the development and analysis of real-time control and self-sensing algorithms, placing emphasis on computational efficiency while maintaining a high degree of accuracy compared to the real system.

Several iterations of this work have been published in (Prechtl et al. 2020, 2021c,b, 2024; Baltes et al. 2022b), with excerpts from those publications reproduced here with several adaptations. First, the derivations have been adapted to the most recent version of the system model, as presented in this dissertation. Second, the numerical examples, plots and parameter study have been reproduced using realistic parameters identified on experimental data from Gen. B prototypes. And finally, a brief discussion of asymmetries has been added to conclude the analysis.

4.1. Planar Soft Robotic Platform Model

The T-Platform consists of a flexible backbone and two pre-tensioned RDEAs which pull the pre-tensioned structure to either side depending on their respective actuation voltages. A more detailed description of the T-Platform operating principle has been given in Section 2.2. In the following, a kinematic model is established and system coordinates are defined, followed by the kinetic modeling section based on a Lagrangian approach. Several aspects of the model are analyzed in detail, such as the transition between mono- and bistable behavior, the occurrence of numerical stiffness and a physically motivated model order reduction to resolve it. The chapter is concluded by an experimental validation campaign.

4.1.1. Kinematics

The kinematic model defines the relationship between actuator lengths and the overall T-Platform pose described by its degrees of freedom. The relevant components from a modeling perspective are the left and right stretchable DE actuators (modeled as axially-expanding one-dimensional elements), a flexible bending element in the center, and a rigid support structure connecting those parts. The actuators consist of flexible polymeric material and will bend at the connecting points, which is modeled through revolute joints

at the actuator ends. The flexible bending element ("beam") in the center does not constrain the structure kinematically and will only play a role when considering the statics and dynamics later.

We start by defining a reference coordinate system for the T-Platform. After the previous abstraction steps, we are left with one rigid body (top plate). Since the configuration of the structure is uniquely determined once we fix the configuration of the rigid body describing the rigid top plate, it is reasonable to choose the parameters describing the in-plane configuration of such rigid body as system Lagrangian parameters. We consider the two reference frames shown in Figure 4.1a, i.e., a fixed one $\mathbf{0} - \boldsymbol{xy}$ (depicted in blue) and a moving one $\boldsymbol{p}_{com} - \boldsymbol{x'y'}$ attached to the rigid top-plate (depicted in red) and with origin coinciding with its center of mass. When the system is in its neutral configuration, the two reference frames coincide. Therefore, the position and orientation of $\boldsymbol{p}_{com} - \boldsymbol{x'y'}$ with respect to those of $\mathbf{0} - \boldsymbol{xy}$ can be used to naturally describe the system configuration. More specifically, the position of the top-plate center of mass (i.e., the origin of $\boldsymbol{p}_{com} - \boldsymbol{x'y'}$) is expressed with respect to the fixed from $\mathbf{0} - \boldsymbol{xy}$ frame as follows

$$\boldsymbol{p}_{com} = \begin{bmatrix} q_x & q_y \end{bmatrix}^T, \tag{4.1}$$

where q_x and q_y are illustrated in Fig. 4.1a. The orientation, instead, is specified through rotation matrix

$$R = \begin{bmatrix} \cos\alpha & -\sin\alpha \\ \sin\alpha & \cos\alpha \end{bmatrix}, \tag{4.2}$$

with α denoting the orientation of the upper structure in relation to the reference system, cf. Figure 4.1a. The degrees of freedom which uniquely define $\mathbf{0} - \boldsymbol{xy}$ and, in turn, the system configuration, are then collected into the following vector $\boldsymbol{q}$

$$\boldsymbol{q} = \begin{bmatrix} q_x & q_y & \alpha \end{bmatrix}^T. \tag{4.3}$$

Now, the goal is to define the coordinates of several important reference points on the structure as a function of $\boldsymbol{q}$, in order to finally express the actuator lengths as a function of $\boldsymbol{q}$ as well. The beam tip position $\boldsymbol{c}_0$ and the point $\boldsymbol{c}$ on the rigid top plate are given by (cf. Figure 4.1a)

$$\boldsymbol{c}_0 = \boldsymbol{p}_{com} + R \begin{bmatrix} 0 \\ -\frac{b_{top}}{2} \end{bmatrix}, \qquad \boldsymbol{c} = \boldsymbol{p}_{com} + R \begin{bmatrix} 0 \\ \frac{b_{top}}{2} \end{bmatrix}. \tag{4.4}$$

The rigid top plate connects the beam tip $\boldsymbol{c}_0$ to the RDEA pivoting points $\boldsymbol{p}_1$ and $\boldsymbol{p}_2$, and is characterized by an offset b_{top} along $\boldsymbol{y'}$ (connecting the beam tip $\boldsymbol{c}_0$ to point $\boldsymbol{c}$) as well as lateral offsets of w_1 and w_2 along $\boldsymbol{x'}$ towards the left and right pivots $\boldsymbol{p}_1$ and $\boldsymbol{p}_2$, respectively. In addition, vertical offsets v_1 and v_2 along $\boldsymbol{y'}$ are considered.

$$\boldsymbol{p}_1 = \boldsymbol{c} + R \begin{bmatrix} -w_1 \\ -v_1 \end{bmatrix}, \qquad \boldsymbol{p}_2 = \boldsymbol{c} + R \begin{bmatrix} w_2 \\ -v_2 \end{bmatrix}. \tag{4.5}$$

The lower pivot points $\boldsymbol{d}_1$ and $\boldsymbol{d}_2$ are considered fixed with respect to the lower clamping position of the beam, and are characterized by horizontal offsets a_1 and a_2 and vertical offsets b_1 and b_2:

$$\boldsymbol{d}_1 = \begin{bmatrix} -a_1 \\ b_1 - l_b - \frac{b_{top}}{2} \end{bmatrix}, \quad \boldsymbol{d}_2 = \begin{bmatrix} a_2 \\ b_2 - l_b - \frac{b_{top}}{2} \end{bmatrix}. \tag{4.6}$$

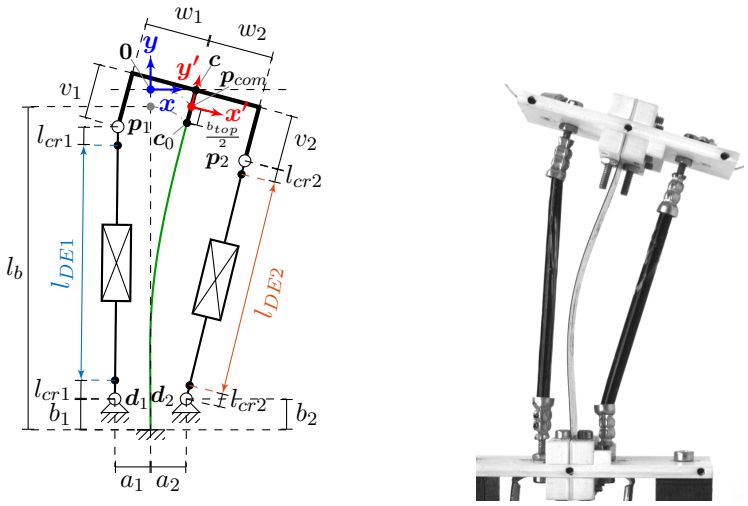

(a) Sketch of the kinematic structure. (b) Physical Prototype.

Figure 4.1.: Illustration of the kinematic model in comparison to the physical prototype of the flexible structure (Prechtl et al. 2024).

where l_b is the length of the undeformed beam. The actuator lengths can then be expressed as a function of the generalized coordinates as:

$$\boldsymbol{l}_{DE}(\boldsymbol{q}) = \begin{bmatrix} l_{DE1}(\boldsymbol{q}) \\ l_{DE2}(\boldsymbol{q}) \end{bmatrix} = \begin{bmatrix} \|\boldsymbol{p}_1 - \boldsymbol{d}_1\| - 2l_{cr1} \\ \|\boldsymbol{p}_2 - \boldsymbol{d}_2\| - 2l_{cr2} \end{bmatrix}, \tag{4.7}$$

with the geometric parameters l_{cr1} and l_{cr2} denoting passive regions, which don't contribute to the *effective* length of the flexible actuator material. By substituting Equations (4.5) and (4.6) into (4.7), we obtain the following relationships:

$$l_{DE1}(\boldsymbol{q}) = \left\| \begin{bmatrix} q_x + a_1 \\ q_y - b_1 + l_b + \frac{b_{top}}{2} \end{bmatrix} + R \begin{bmatrix} -w_1 \\ \frac{b_{top}}{2} - v_1 \end{bmatrix} \right\| - 2l_{cr1}, \tag{4.8}$$

$$l_{DE2}(\boldsymbol{q}) = \left\| \begin{bmatrix} q_x - a_2 \\ q_y - b_2 + l_b + \frac{b_{top}}{2} \end{bmatrix} + R \begin{bmatrix} w_2 \\ \frac{b_{top}}{2} - v_2 \end{bmatrix} \right\| - 2l_{cr2}. \tag{4.9}$$

4.1.2. Dynamic Model

The dynamic model is derived using a Lagrangian approach. The Lagrangian $\mathcal{L}$ of the system is given as the difference between kinetic and potential energies, as follows

$$\mathcal{L}(\boldsymbol{q}, \dot{\boldsymbol{q}}) = \frac{1}{2}\dot{\boldsymbol{q}}^\intercal M \dot{\boldsymbol{q}} - \mathcal{V}(\boldsymbol{q}), \tag{4.10}$$

with constant inertia matrix (due to the adopted choice of $\boldsymbol{q}$)

$$M = \begin{bmatrix} m_H & 0 & 0 \\ 0 & m_H & 0 \\ 0 & 0 & J_H \end{bmatrix}$$

and configuration-dependent potential energy given by

$$\mathcal{V}(\boldsymbol{q},\boldsymbol{u}) = m_H g q_y + \mathcal{V}_b(\boldsymbol{q}) + \mathcal{V}_{DE}(\boldsymbol{q},\boldsymbol{u}), \tag{4.11}$$

consisting of a gravitational contribution (with g denoting the gravitational acceleration) as well as elastic contributions from the flexible backbone $\mathcal{V}_b$ and the DEAs $\mathcal{V}_{DE}$. In (4.10) and (4.11), we assume that the system mass m_H is concentrated in the rigid top plate with the moment of inertia J_H. The flexible beam is modeled in a lumped fashion via the beam constraint model (Awtar et al. 2010). The potential energy is given as

$$\mathcal{V}_b(\boldsymbol{q}) = \frac{EI}{2l_b}\left(\boldsymbol{\nu}^\intercal G\boldsymbol{\nu} + \frac{\left(u_x + \frac{1}{2}\boldsymbol{\nu}^\intercal P\boldsymbol{\nu}\right)^2}{\frac{I}{Al_b^2} - \boldsymbol{\nu}^\intercal Q\boldsymbol{\nu}}\right) \tag{4.12}$$

with

$$u_x = \frac{b_{top}}{2l_b}(1-\cos\alpha) + \frac{q_y}{l_b}, \quad \boldsymbol{\nu} = \begin{bmatrix} -\frac{b_{top}}{2l_b}\sin\alpha - \frac{q_x}{l_b} \\ \alpha \end{bmatrix},$$

$$G = \begin{bmatrix} 12 & -6 \\ -6 & 4 \end{bmatrix}, P = \begin{bmatrix} \frac{6}{5} & -\frac{1}{10} \\ -\frac{1}{10} & \frac{2}{15} \end{bmatrix}, Q = \begin{bmatrix} -\frac{1}{700} & \frac{1}{1400} \\ \frac{1}{1400} & -\frac{11}{6300} \end{bmatrix},$$

where E is the Young's modulus of the beam material, while A and I refer to the cross-sectional area and second moment of area of the beam, respectively. Compared to more well-known models in soft robotics such as the Cosserat rod (Cosserat et al. 1909), the beam constraint model (BCM) offers a simple algebraic structure and closed-form expressions for the elastic energy as a function of the tip displacement. It should be noted that the BCM is spezialized to the case of a slender beam pinned on one end while subjected to an axial load at the tip, while moving in a planar space. For future works considering three-dimensional movement, suitable discretizations of modern beam models such as Harsch et al. 2023 should be considered.

Each DEA is modeled as a rolled actuator deforming in strongly uniaxial mode, as derived in Section 3.1.4. The corresponding potential energy (3.62) can be additively decomposed in a mechanical and an electrical contribution, as follows

$$\mathcal{V}_{DEj}(\boldsymbol{q},\boldsymbol{u}) = \sum_{j=1}^{2}\sum_{h=1}^{3}\pi\left(R_{oj}^2 - R_{ij}^2\right)\left[L_{1j}C_{jh}\left(\frac{2L_{1j}}{l_{DEj}(\boldsymbol{q})} + \frac{l_{DEj}(\boldsymbol{q})^2}{L_{1j}^2} - 3\right)^h - \frac{v_{DEj}^2}{2}\epsilon_0\epsilon_r\eta_B\alpha_{ej}\frac{l_{DEj}}{L_3^2}\right]. \tag{4.13}$$

In (4.13), v_{DEj} is the voltage applied to DEA j (collected in vector $\boldsymbol{u} = \begin{bmatrix} v_{DE1}^2 & v_{DE2}^2 \end{bmatrix}^T$), while l_{DEj} represents the length of the same membrane, expressed as a function of $\boldsymbol{q}$ via the kinematic model given in Equations (4.8) and (4.9).

Parameters L_{1j}, R_{oj}, and R_{ij} represent the undeformed axial length, outer radius, and inner radius of roll j, respectively, while C_{jh} are the Yeoh parameters describing the hyperelastic response of DE j. In addition, ϵ_0 is given as the vacuum permittivity while, for DEA j, L_{3j} represents the undeformed thickness of the polymeric membranes, α_{ej} and η_B denote the fraction of membrane surface covered by electrodes in axial and circumferential directions, respectively, and ϵ_{rj} denotes the material relative permittivity.

Note that, as discussed in Section 3.1.6, the first contribution in (4.13) represents a true mechanical potential energy, while the second one is formally an electrical potential co-energy, since it is expressed as a function of voltage rather than electric charge. Nevertheless, since our primary goal is to develop a mechanical energy expression which is useful for the Lagrangian formalism, the distinction between electric energy and co-energy is of no practical relevance. Therefore, we will simply refer at (4.13) as DEA potential energy. The equations of motion can now be expressed as follows

$$\frac{d}{dt}\left(\frac{\partial \mathcal{L}}{\partial \dot{\boldsymbol{q}}}\right)^{\intercal} - \left(\frac{\partial \mathcal{L}}{\partial \boldsymbol{q}}\right)^{\intercal} = M\ddot{\boldsymbol{q}} + \frac{\partial \mathcal{V}(\boldsymbol{q},\boldsymbol{u})}{\partial \boldsymbol{q}} = -D(\boldsymbol{q})\dot{\boldsymbol{q}}, \quad (4.14)$$

where the right hand side of (4.14) represents non-conservative external forces. The first term on the right-hand side of (4.14) describes dissipation forces, via positive definite matrix

$$D(\boldsymbol{q}) = \begin{bmatrix} d_x & 0 & 0 \\ 0 & d_y & 0 \\ 0 & 0 & d_\alpha \end{bmatrix} + J^{\intercal}(\boldsymbol{q}) \begin{bmatrix} \frac{\eta_1 \pi (R_{o1}^2 - R_{i1}^2)}{l_{DE1}(\boldsymbol{q})} & 0 \\ 0 & \frac{\eta_2 \pi (R_{o2}^2 - R_{i2}^2)}{l_{DE2}(\boldsymbol{q})} \end{bmatrix} J(\boldsymbol{q}) \quad (4.15)$$

is composed of linear damping d_x, d_y, d_α in the coordinate directions and a second term representing viscoelasticity of the DEAs through parameters η_1 and η_2. Note that, compared to the viscoelastic model discussed in Section 3.1.7, this choice represents a simpler damping model. It is generally possible to choose a DE hysteresis model containing additional Lion and Maxwell branches for higher fidelity dynamic models, although this increases the number of state components and complicates parameter identification of the overall structure. At the same time, friction in other parts of the soft robotic structure would be comparatively neglected. Tests carried out by the author suggest that the chosen trade-off is justified for the scope of this work, although different applications might choose a different solution.

The Jacobian matrix J is given by

$$J(\boldsymbol{q}) = \frac{\partial \boldsymbol{l}_{DE}(\boldsymbol{q})}{\partial \boldsymbol{q}}, \quad (4.16)$$

with $\boldsymbol{l}_{DE}(\boldsymbol{q})$ given by the kinematic model (4.7).

The forces exercised by the rolled DEAs decompose into a hyperelastic and an actuation-related contribution as follows:

$$\frac{\partial \mathcal{V}_{DE}(\boldsymbol{q},\boldsymbol{u})}{\partial \boldsymbol{q}} = \boldsymbol{J}^T \boldsymbol{F}_{DE}(\boldsymbol{q}) + \Gamma_e \boldsymbol{u} \quad (4.17)$$

with

$$\Gamma_e = \begin{bmatrix} \gamma_{e1} & 0 \\ 0 & \gamma_{e2} \end{bmatrix}, \quad \gamma_{ej} = \frac{\pi (R_{oj}^2 - R_{ij}^2) \alpha_{ej} \epsilon_0 \epsilon_{rj}}{2 L_{3j}^2}. \quad (4.18)$$

By collecting (4.10)-(4.18), the model can be formulated in state-space form. By defining state $\boldsymbol{x} = \begin{bmatrix} \boldsymbol{x}_1^{\intercal} & \boldsymbol{x}_2^{\intercal} \end{bmatrix}^{\intercal} = \begin{bmatrix} \boldsymbol{q}^{\intercal} & \dot{\boldsymbol{q}}^{\intercal} \end{bmatrix}^{\intercal}$, input $\boldsymbol{u}$, and measured output $\boldsymbol{y} = \boldsymbol{l}_{DE}$, from (4.14)

we obtain

$$\begin{aligned}\dot{\boldsymbol{x}} &= f_x(\boldsymbol{x}, \boldsymbol{u}) \\ &= \begin{bmatrix} \boldsymbol{x}_2 \\ -M^{-1}\left(\left(\frac{\partial \mathcal{V}_b(\boldsymbol{x_1})}{\partial \boldsymbol{x_1}}\right)^T + \boldsymbol{J}^T(\boldsymbol{x}_1)\boldsymbol{F}_{DE}(\boldsymbol{x}_1) + \begin{bmatrix} 0 \\ m_H g \\ 0 \end{bmatrix} + D(\boldsymbol{x_1})\boldsymbol{x}_2 - J^{\intercal}(\boldsymbol{x_1})\Gamma_e \boldsymbol{u}\right) \end{bmatrix}, \\ \boldsymbol{y} &= h_x(\boldsymbol{x}) = \boldsymbol{l}_{DE}(\boldsymbol{x}_1).\end{aligned} \tag{4.19}$$

4.1.3. Reduced Dynamic Model

The model presented so far results in a state-space description with six state components. The full model exhibits fast vertical dynamics compared to those along the horizontal and bending directions, which is related to the fact that long and slender beams possess a significantly larger compressive stiffness compared to the bending one. This leads to high numerical stiffness of the model when operating nearby the vertical configuration. Even though this does not cause issues when using advanced ODE discretization schemes for offline simulation, problems may arise when integrating the model into real-time applications (e.g. state observers). In order to minimize the real-time computation burden, it might be advantageous to reduce the size of the state by introducing additional constraints, while still approximating the full system dynamics as tight as possible.

The method of simplifying the dynamic of model (4.19) is grounded on the author's previous work Prechtl et al. 2021b. In here, it was shown how a kinematic constraint for the vertical tip displacement of the beam can be found by neglecting the contribution of the vertical force components. Such approach revealed to be effective when performing qualitative stability analysis on the T-Platform. In here, inspired by the original model order reduction idea Prechtl et al. 2021b, a more general approach is proposed. First, we define the vertical force acting on the beam:

$$\frac{\partial \mathcal{V}_b(\boldsymbol{q})}{\partial q_y} =: \tau_y. \tag{4.20}$$

By replacing (4.12) in (4.20) and solving for q_y, we arrive at

$$q_y(q_x, \alpha) = \boldsymbol{\nu}^{\intercal} \underbrace{\left(-\frac{l_b}{2}P - \frac{\tau_y l_b^3}{EI}Q\right)}_{:=\Gamma} \boldsymbol{\nu} + \underbrace{\frac{\tau_y l_b}{EA}}_{:=\gamma} - \frac{b_{top}}{2}(1 - \cos\alpha). \tag{4.21}$$

Note that q_y in (4.21) only depends on other kinematic variables q_x, α and on the vertical beam force τ_y. In the full order model (4.19), τ_y is the sum of dynamic forces such as inertia and damping as well as static forces, i.e., gravity and DEA pre-strain force. By assuming that the static force contributions dominate the dynamic ones, and also assuming that this static force remains approximately constant, we can approximate $\tau_y \approx$ constant. In this way, (4.21) becomes an algebraic relationship between q_y and the variables q_x, α, with constant parameter τ_y. This algebraic relationship between kinematic variables serves as the basis for a reduced order model with only two remaining DoF.

To formally derive the simplified order model, we define the reduced configuration vector in $\boldsymbol{r} = \begin{bmatrix} q_x & \alpha \end{bmatrix}^\intercal$, and use (4.21) to express the transformation between $\boldsymbol{r}$ and $\boldsymbol{q}$ through

$$\boldsymbol{q}(\boldsymbol{r}) = \begin{bmatrix} q_x \\ q_y(q_x, \alpha) \\ \alpha \end{bmatrix}, \; J_{qr}(\boldsymbol{r}) = \frac{\partial \boldsymbol{q}(\boldsymbol{r})}{\partial \boldsymbol{r}} = \begin{bmatrix} 1 & 0 \\ \frac{\partial q_y(q_x,\alpha)}{\partial q_x} & \frac{\partial q_y(q_x,\alpha)}{\partial \alpha} \\ 0 & 1 \end{bmatrix}. \tag{4.22}$$

We can then replace (4.22) into the Lagrangian (4.10), and derive new equations of motion with respect to coordinates $\boldsymbol{r}$, obtaining

$$\frac{d}{dt}\left(\frac{\partial \mathcal{L}}{\partial \dot{\boldsymbol{r}}}\right)^\intercal - \left(\frac{\partial \mathcal{L}}{\partial \boldsymbol{r}}\right)^\intercal = M_r(\boldsymbol{r})\ddot{\boldsymbol{r}} + C_r(\boldsymbol{r}, \dot{\boldsymbol{r}})\dot{\boldsymbol{r}} + \left(\frac{\partial \mathcal{V}(\boldsymbol{q}(\boldsymbol{r}), \boldsymbol{u})}{\partial \boldsymbol{r}}\right)^\intercal = -D_r(\boldsymbol{r})\dot{r} \tag{4.23}$$

with inertia and damping matrices given by

$$M_r(\boldsymbol{r}) = J_{qr}^\intercal(\boldsymbol{r}) M J_{qr}(\boldsymbol{r}), \tag{4.24}$$

$$D_r(\boldsymbol{r}) = J_{qr}^\intercal(\boldsymbol{r}) D(\boldsymbol{q}(\boldsymbol{r})) J_{qr}(\boldsymbol{r}), \tag{4.25}$$

while C_r is such that

$$C_r(\boldsymbol{r}, \dot{\boldsymbol{r}})\dot{\boldsymbol{r}} = \dot{M}_r(\boldsymbol{r})\dot{\boldsymbol{r}} - \frac{1}{2}\frac{\partial\left(\dot{\boldsymbol{r}}^\intercal M_r\left(\boldsymbol{r}\right)\dot{\boldsymbol{r}}\right)}{\partial \boldsymbol{r}}.$$

Finally, we introduce the reduced state $\boldsymbol{\xi} = \begin{bmatrix} \boldsymbol{\xi}_1^\intercal & \boldsymbol{\xi}_2^\intercal \end{bmatrix}^\intercal = \begin{bmatrix} \boldsymbol{r}^\intercal & \dot{\boldsymbol{r}}^\intercal \end{bmatrix}$ and obtain the state-space description of the reduced model with measured output $\boldsymbol{\zeta}$ (some explicit dependencies on $\boldsymbol{\xi}$ are omitted for the ease of conciseness)

$$\begin{aligned} \dot{\boldsymbol{\xi}} &= f_\xi(\boldsymbol{\xi}, \boldsymbol{u}) \\ &= \begin{bmatrix} \xi_2 \\ M_r^{-1}\left(-(C_r + D_r)\boldsymbol{\xi}_2 - \left(\frac{\partial \mathcal{V}_b}{\partial \boldsymbol{r}}\right)^\intercal - J_{qr}^T J^T F_{DE} - J_{qr}^T \begin{bmatrix} 0 \\ m_H g \\ 0 \end{bmatrix} + J_{qr}^\intercal J^\intercal \Gamma_e \boldsymbol{u}\right) \end{bmatrix}, \\ \boldsymbol{\zeta} &= h_\xi(\boldsymbol{\xi}) = \boldsymbol{l}_{DE}(\boldsymbol{q}(\boldsymbol{\xi}_1)). \end{aligned} \tag{4.26}$$

Model (4.26) offers a means to simplify the implementation of the system-level self-sensing without sacrificing the accuracy, as will be clarified in Section 5.2.3.

4.2. Multi-DoF bistable biasing concept

In this section, a model-based analysis aimed at maximizing the T-platform angular displacement is presented. In particular, the goal is to understand the physical mechanism which causes the T-platform to largely bend upon DEA actuation. Specifically, the developed model predicts a transition from monostable to bistable behavior depending on the compression of the flexible backbone. Based on this analysis, energy-based design conditions for large actuation stroke will be developed.

4.2.1. Energy-based Mechanism for Bistable Actuation

For the evaluation of the displacement performance, we consider system (4.14) at steady-state. Since at equilibrium all time derivatives must vanish, the resulting set of equations reduces to

$$\frac{\partial \mathcal{V}(\boldsymbol{q}, \boldsymbol{u} = \text{const.})}{\partial \boldsymbol{q}} = 0. \tag{4.27}$$

Once the DEA voltages are fixed to constant values, equation (4.27) can be solved for $\boldsymbol{q}$ to find the corresponding equilibrium state. Such equilibrium states will graphically correspond to the critical points of the potential energy $\mathcal{V}$. By comparing the equilibrium configurations computed for unactuated and actuated cases, we can estimate the resulting displacement that the platform undergoes due to the DEA activation. Clearly, the further apart those equilibrium configurations, the larger the resulting displacement. Understanding which parameters affect the distance between those states is crucial for the optimization of the T-platform displacement.

In order to simplify the following discussion, we assume a completely symmetric system, i.e. the system parameters $a_j, b_j, w_j, v_j, L_{1j}, L_{3j}, R_{oj}, R_{ij}, C_{jh}, \alpha_{ej}$ at $j = 1$ (left side) are equal to the respective parameters at $j = 2$ (right side).

Despite valid in principle, the energy-based approach discussed above presents limitations due to the fact that the T-platform is described by a 3-DoF model. This high dimensionality makes it difficult to visualize the critical points of $\mathcal{V}$ and, in turn, to gain intuition on the energy mechanism which ultimately governs the bistable DEA actuation. A possible way to address this issue could consist in approximating the full model with a lower order one, which still captures all its essential features. In this way, the resulting potential energy can be effectively plotted and visualized as a two-dimensional surface.

To this end, we employ the reduced dynamic model from Section 4.1.3. In this way, by solving the corresponding equations (4.23) at steady-state, the following equilibrium condition is obtained:

$$\frac{\partial \mathcal{V}(\boldsymbol{q}(\boldsymbol{r}), \boldsymbol{u} = \text{const.})}{\partial \boldsymbol{r}} = \frac{\partial \mathcal{V}(\boldsymbol{q}(\boldsymbol{r}), \boldsymbol{u} = \text{const.})}{\partial \boldsymbol{q}} \frac{\partial \boldsymbol{q}}{\partial \boldsymbol{r}} = 0. \tag{4.28}$$

Equation (4.28) permits to evaluate the equilibrium states of the system as the critical points of $\mathcal{V}$, when plotted as a two-dimensional surface with respect to $\boldsymbol{r} = \begin{bmatrix} q_x & \alpha \end{bmatrix}^T$. Compared to (4.27), the main advantage of condition (4.28) is that it lends itself better to analytical/graphical design methods, thanks to the reduced dimensionality. Of course, one must keep in mind that the obtained results will only represent an approximation of the true system behavior.

To understand the practical implications of (4.28), simulation results are presented in the following, based on realistic material and system parameters taken from Prechtl et al. 2024. Figure 4.2 shows a contour plot of $\mathcal{V}$ as a function of $\boldsymbol{r}$ at different DE voltages, for a specific combination of parameters as specified in Table B.2. To simplify the notation describing the DEAs activation, we define an equivalent scalar control signal Δv_{DE} as follows:

$$\begin{cases} \Delta v_{DE} > 0 \rightarrow v_{DE1} = |\Delta v_{DE}|\,,\ v_{DE2} = 0, \\ \Delta v_{DE} < 0 \rightarrow v_{DE1} = 0,\ v_{DE2} = |\Delta v_{DE}|\,, \\ \Delta v_{DE} = 0 \rightarrow v_{DE1} = 0,\ v_{DE2} = 0. \end{cases} \tag{4.29}$$

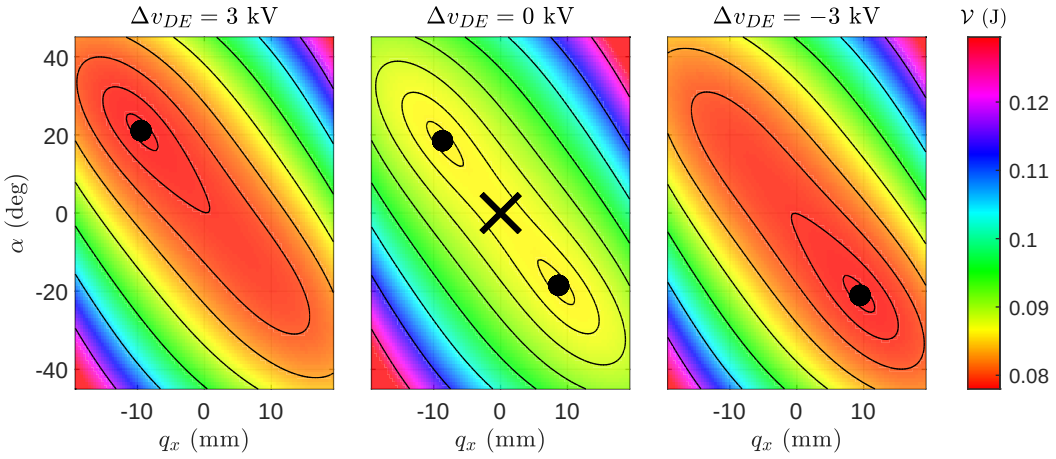

Figure 4.2.: Bistable system, note how it becomes monostable at high voltages.

For $\Delta v_{DE} = 0\,\mathrm{V}$, there are two minima (stable configurations) at approximately $\pm 20°$ and one maximum (unstable configuration) at the origin. If a voltage is applied to either DEA, the energy landscape is tilted towards the direction of the activated membrane. As a result, $\mathcal{V}$ changes into a monostable shape with minima at $-23°$ and $22°$, respectively. Conversely, Fig. 4.3 depicts the energy landscape for l_{cr1} increased by 25 %, with remaining parameters as given in the appendix. In this case, only one equilibrium exists independenty on the applied voltage. Compared to the previous case, the resulting bending angle is remarkably smaller, on the order of $\pm 11°$. In addition, the bistable design allows maintaining the deflected angle when the actuation voltage is removed, thus saving control energy. Conversely, the monostable actuator requires a continuous voltage to keep the angular displacement.

From this analysis, we conclude that the overall system energy can exhibit either a bistable or monostable behavior, depending on the choice of the design parameters. In the former case, the jump among the two stable states can be effectively triggered via activation of the roll DEAs, thus resulting into large angular displacements and low energy consumption, see Fig. 4.2. Comparably smaller angles and higher energy consumption are instead obtained in case a simple monostable robotic module is designed, as in Fig. 4.3.

To further analyze the relationship between energy and system performance, Fig. 4.4 plots the equilibrium horizontal displacement q_x and bending angle α with respect to Δv_{DE}, corresponding to the 2-DoF condition given by (4.28). Note that multiple equilibria may exist for a given Δv_{DE}, where filled dots are used to denote stable points while crosses indicate unstable equilibria. Additionally, the trajectory for a dynamic simulation of the system is drawn in solid blue lines, based on the full 3-DoF model developed in Section 4.1.2. From here, it can be clearly seen that the 2-DoF and the 3-DoF models are overall in good agreement, thus confirming the validity of the proposed approximation. Additionally, it can be observed how the bistable actuator exhibits a branch of unstable equilibria, which makes an input-output hysteresis appear in the simulated response. The situation observed for the bistable system reflects a typical saddle-node bifurcation, in which a pair of stable and unstable branches merge together and annihilate each other as the control voltage Δv_{DE} changes (Strogatz 1994). Conversely, the equilibrium map of the stable actuator is always monotonic.

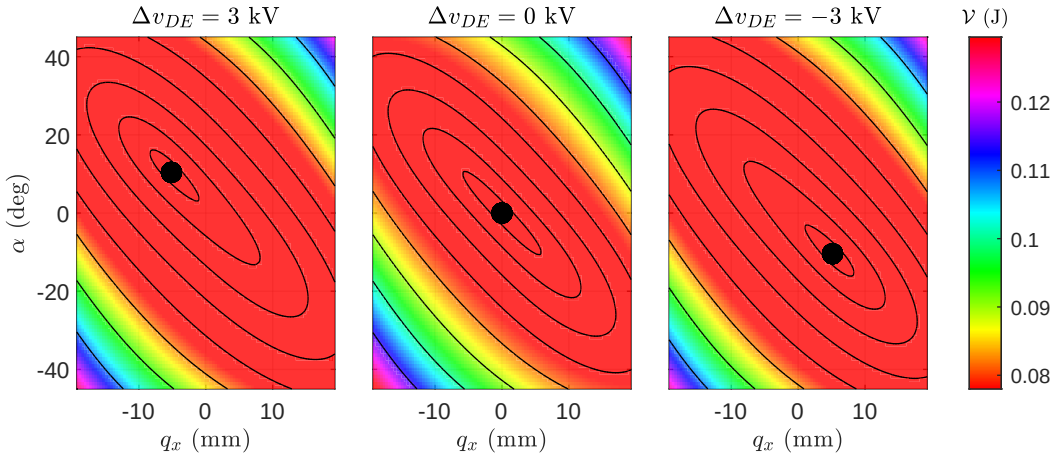

Figure 4.3.: Monostable system, note how it maintaints the monostable feature also at high voltages.

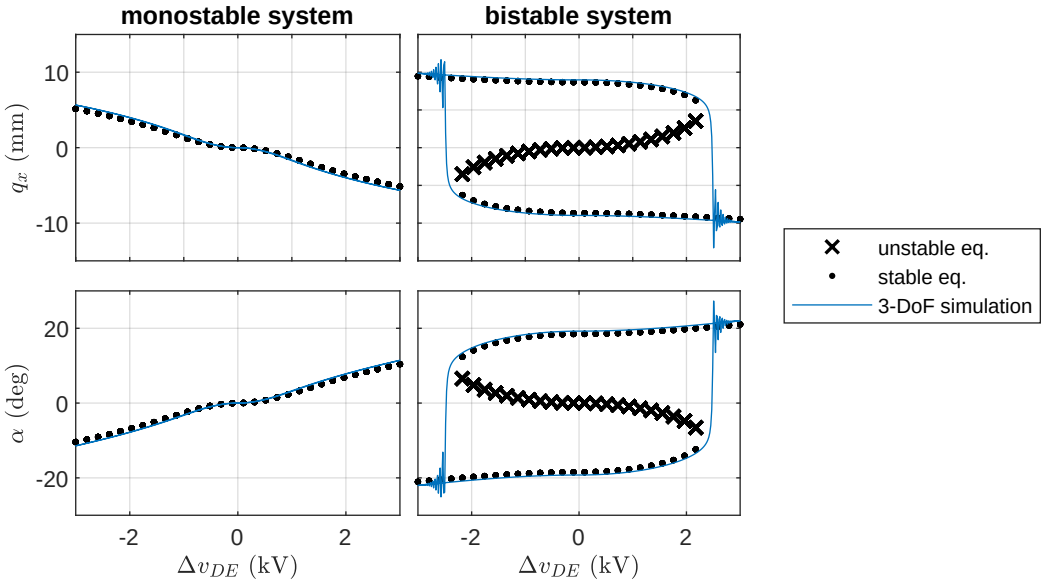

Figure 4.4.: Input-Output equilibrium maps for q_x and α with different system parameters. The solid blue line shows a 3-DoF simulation with slowly varying Δv_{DE}, indicating good agreement with the energy-based analysis.

4.2.2. Energy-based Stability Analysis

Based on the discussion of the previous section, we conclude that the mechanism which results into large bistable actuation of the T-platform is based on a saddle-node bifurcation. Note how the presence or not of a bistable behavior is tightly related to the existence of an unstable equilibrium branch passing through the point $\boldsymbol{r} = \begin{bmatrix} q_x & \alpha \end{bmatrix}^T = 0$. Despite the result has been graphically proven for the 2-DoF model, it is expected that the same instability would occur for the full 3-DoF model as well (although it might be harder to

visualize). Based on this result, we identify the existence of an unstable critical point of $\mathcal{V}$ which satisfies $\Delta v_{DE} = 0$ and $\boldsymbol{r} = 0$ as a suitable criterion for checking the occurrence of a bistable behavior. Mathematically, this condition can be formulated as follows:

$$\exists\ \bar{\boldsymbol{q}} = \begin{bmatrix} 0 \\ \bar{q}_y \\ 0 \end{bmatrix} : \begin{cases} \frac{\partial \mathcal{V}}{\partial \boldsymbol{q}}\Big|_{\boldsymbol{q}=\bar{\boldsymbol{q}},\Delta v_{DE}=0} = 0, \\ \min\left(\mathrm{eig}\left(\boldsymbol{H}_{\boldsymbol{\mathcal{V}}}|_{\boldsymbol{q}=\bar{\boldsymbol{q}},\Delta v_{DE}=0}\right)\right) < 0, \end{cases} \tag{4.30}$$

for an arbitrary $\bar{q}_y \in \mathbb{R}$, with $\boldsymbol{H}_{\boldsymbol{\mathcal{V}}}$ denoting the Hessian matrix of $\mathcal{V}$, i.e.,

$$\boldsymbol{H}_{\boldsymbol{\mathcal{V}}} = \frac{\partial^2 \mathcal{V}}{\partial \boldsymbol{q}^2}. \tag{4.31}$$

Note that (4.11) allows us to compute the total gradient as the sum of gradients of the individual energy contributions, i.e.,

$$\frac{\partial \mathcal{V}}{\partial \boldsymbol{q}} = \frac{\partial (m_H g q_y)}{\partial \boldsymbol{q}} + \frac{\partial \mathcal{V}_B}{\partial \boldsymbol{q}} + \frac{\partial \mathcal{V}_{DE}}{\partial \boldsymbol{q}}. \tag{4.32}$$

To check if the gradient condition in (4.30) holds true, we start by computing the gradient of the first term at equilibrium, i.e.,

$$\frac{\partial (m_H g q_y)}{\partial \boldsymbol{q}}\Big|_{\boldsymbol{q}=\bar{\boldsymbol{q}},\Delta v_{DE}=0} = \begin{bmatrix} 0 & m_H g & 0 \end{bmatrix}. \tag{4.33}$$

Similarly, the gradient of $\mathcal{V}_B$ at equilibrium is given by

$$\frac{\partial \mathcal{V}_B}{\partial \boldsymbol{q}}\Big|_{\boldsymbol{q}=\bar{\boldsymbol{q}},\Delta v_{DE}=0} = \begin{bmatrix} 0 & \frac{EA}{l_b}\bar{q}_y & 0 \end{bmatrix}, \tag{4.34}$$

The computation of the gradient contribution related to the DEAs is more involved, since it depends primarily on the actuator lengths $\boldsymbol{l_{DE}}$, thus it is necessary to rely on the chain rule. More specifically, the gradient is given by

$$\frac{\partial V_{DE}}{\partial \boldsymbol{q}}\Big|_{\boldsymbol{q}=\bar{\boldsymbol{q}},\Delta v_{DE}=0} = \frac{\partial V_{DE}}{\partial \boldsymbol{l_{DE}}}\boldsymbol{J}\Big|_{\boldsymbol{q}=\bar{\boldsymbol{q}},\Delta v_{DE}=0}. \tag{4.35}$$

To compute (4.35), we first define the following quantity

$$\begin{aligned} l_{DE0}(\bar{q}_y) :=& l_{DE1}(\bar{\boldsymbol{q}}) = l_{DE2}(\bar{\boldsymbol{q}}) \\ =& \sqrt{(a_1 - w_1)^2 + (\bar{q}_y - b_1 + l_b + b_{top} - v_1)^2} - 2l_{cr1}. \end{aligned} \tag{4.36}$$

Since we have $\Delta v_{DE} = 0$, it follows that the partial derivatives with respect to the DEA lengths are equal, i.e.,

$$\frac{\partial \mathcal{V}_{DE}}{\partial \boldsymbol{l_{DE}}}\Big|_{\boldsymbol{q}=\bar{\boldsymbol{q}},\Delta v_{DE}=0} = \begin{bmatrix} F_{DE0}(\bar{q}_y) & F_{DE0}(\bar{q}_y) \end{bmatrix}. \tag{4.37}$$

The Jacobian matrix for $\boldsymbol{q} = \bar{\boldsymbol{q}}$ can be computed based on (4.16), as follows

$$\boldsymbol{J}(\bar{\boldsymbol{q}}) = \frac{1}{l_{DE0}(\bar{q}_y)} \begin{bmatrix} a_1 - w_1 & b_{top} - b_1 + l_b + \bar{q}_y - v_1 & -\gamma(\bar{q}_y) \\ -a_1 + w_1 & b_{top} - b_1 + l_b + \bar{q}_y - v_1 & \gamma(\bar{q}_y) \end{bmatrix}, \tag{4.38}$$

where $\gamma(\bar{q}_y)$ abbreviates a term of no further significance, since it cancels out in the next step. The combination of (4.37) and (4.38) according to (4.35) leads to

$$\left.\frac{\partial \mathcal{V}_{DE}}{\partial \boldsymbol{q}}\right|_{\boldsymbol{q}=\bar{\boldsymbol{q}},\Delta v_{DE}=0} = \begin{bmatrix} 0 & \frac{2F_{DE0}(\bar{q}_y)}{l_{DE0}(\bar{q}_y)}(b_{top} - b_1 + l_b + \bar{q}_y - v_1) & 0 \end{bmatrix}. \tag{4.39}$$

By replacing (4.33), (4.34), and (4.39) in (4.32), it can be concluded that the gradient condition (4.30) is true if the following holds

$$m_H g + \frac{EA}{l_b}\bar{q}_y + \frac{2F_{DE0}(\bar{q}_y)}{l_{DE0}(\bar{q}_y)}(b_{top} - b_1 + l_b + \bar{q}_y - v_1) = 0. \tag{4.40}$$

It is generally possible to find a $\bar{q}_y$ which satisfies (4.40) for typical system parameters. Note that (4.40) can be simply interpreted as the force equilibrium equation along the vertical axis.

The evaluation of the Hessian condition in (4.30), on the other hand, is more involved, and thus it is omitted for conciseness. Its computation reveals that the sign of the minimum eigenvalue of $\boldsymbol{H}_{\boldsymbol{\mathcal{V}}}$ at $\boldsymbol{q} = \bar{\boldsymbol{q}}$ and $\Delta v_{DE} = 0$ is not uniquely defined, but instead it depends on multiple system parameters. More specifically, the parameters that explicitly affect the Hessian condition include the beam parameters E, A, and I, the T-platform geometrical parameters a_j, b_j, w_j, v_j, $l_{cr,j}$ and l_b, as well as on the DEA initial lengths l_{DE0}, which is also function of the geometry parameters, cf. Equation (4.36). Note that the corresponding DEA initial force F_{DE0} is also determined by l_{DE0} via the constitutive material model, as well as by the roll geometry defined by $L_1 j$, R_{oj}, R_{ij} and L_{3j}.

The discussion presented so far is restricted to symmetric system parameters. In general, an asymmetry leads to a shifted neutral (i.e. zero-voltage) equilibrium away from $\bar{q}_x = 0, \bar{\alpha} = 0$ and asymmetric equilibrium maps, as shown in Figure 4.5. The developed condition of bistability (4.30) stays the same, only the neutral equilibrium $\bar{\boldsymbol{q}}$ is shifted:

$$\exists\, \bar{\boldsymbol{q}} = \begin{bmatrix} \bar{q}_x \\ \bar{q}_y \\ \bar{\alpha} \end{bmatrix} : \begin{cases} \left.\frac{\partial \mathcal{V}}{\partial \boldsymbol{q}}\right|_{\boldsymbol{q}=\bar{\boldsymbol{q}},\Delta v_{DE}=0} = 0, \\ \min\left(\mathrm{eig}\left(\boldsymbol{H}_{\boldsymbol{\mathcal{V}}}|_{\boldsymbol{q}=\bar{\boldsymbol{q}},\Delta v_{DE}=0}\right)\right) < 0, \end{cases} \tag{4.41}$$

Since a further analytical development offers no additional insights, it is omitted from the discussion. In this case, it is preferable to evaluate Equation (4.41) numerically and study the resulting equilibrium map Figure 4.5. Compared to the symmetric system from Figure 4.4, we observe a shift and slight distortion of the system response. It is therefore intuitively clear that in case of extreme asymmetry, the region of unstable equilibria (bistable case) can be shifted in such a way that no unstable equilibria exist at zero-voltage. While theoretically possible to analyze, the practical relevance of such configurations is questionable.

4.2.3. Parameter Study

While the condition on bistability serves as a tool for understanding the occurence of bistability, it can also be useful for practical design. As an example, one can evaluate the minimum eigenvalue of the hessian $H_{\mathcal{V}}$ (evaluated at the neutral equilibrium) as a function of system parameters, as shown in Figure 4.6. The plots on the left side show the smallest hessian eigenvalue evaluated on slices of the design space of possible parameter

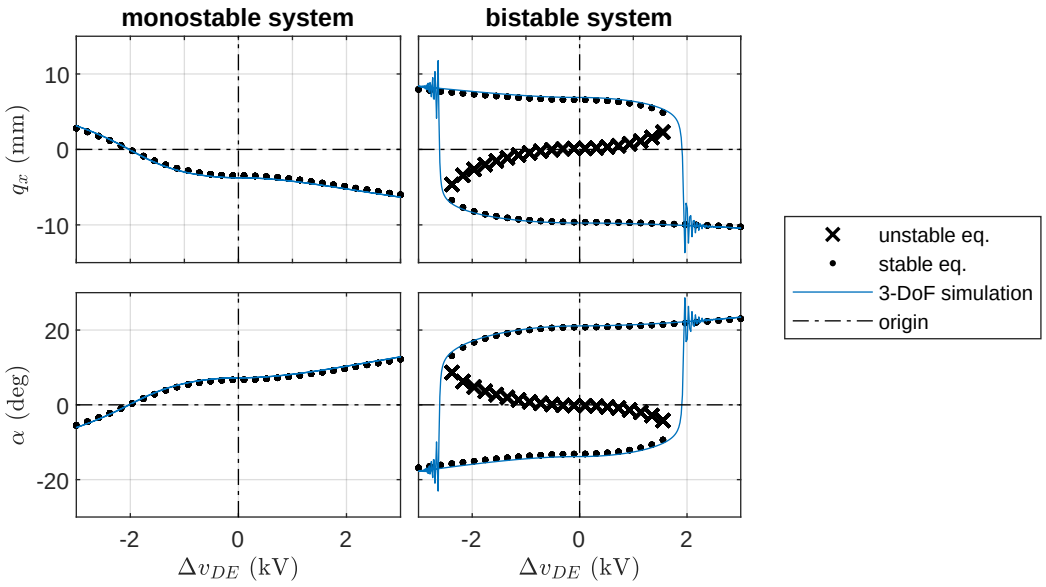

Figure 4.5.: Input-Output equilibrium maps for q_x and α for an asymmetric system tuned for monostable and bistable behaviour, respectively.

combinations (a_1, b_1), (b_1, I) and (a_1, I), respectively. Based on the previous discussion, we expect configurations with negative eigenvalues to present bistable behavior, and monostable configurations in the positive-eigenvalue case. This is confirmed when obtaining dynamic simulations of selected configurations from the parameter space. A color code has been established, where blue-colored configurations possess negative minimum eigenvalues in the left-hand plot and exhibit bistable behavior in the corresponding simulation on the right-hand side, while red-colored configurations possess positive minimum eigenvalues and, as expected, show monostable behavior in simulations. It is possible to apply this method to any desired combination of parameters, as shown in more detail in Prechtl et al. 2021b.

4.3. Experimental Validation

The developed T-Platform model has been experimentally validated in several published works, of which a selection is summarized in the following. During the practical evolution of the physical T-Platform prototypes, a diverse selection of materials (steel, 3D-printed plastic materials), geometries and mounting techniques (3D-printed rotating joints or fixing the actuator ends and force them to bend) has been put forward in order to test the model's capabilities.

In order to quantitatively compare experimental and simulation results, a custom and precise optical tracking setup was developed. Furthermore, as a result of the highly nonlinear system behavior and sizable number of parameters, it was necessary to establish a capable automated calibration procedure.

In this section, the results are presented in consolidated form based on the most recent formulation of the T-Platform model, as presented in Section 4.1. Compared to earlier

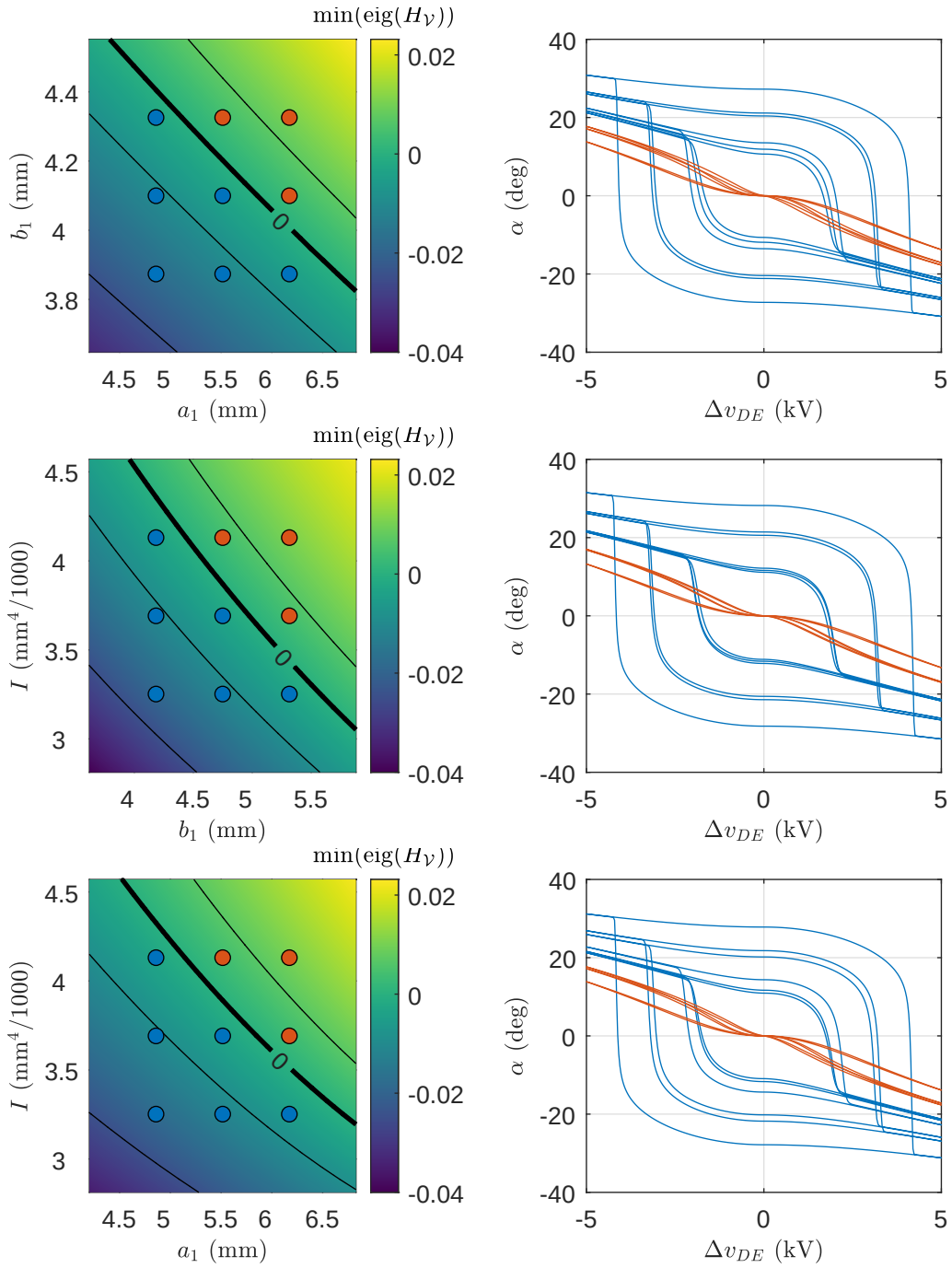

Figure 4.6.: Bistability criterion in the parameter planes (a_1, b_1) (top row), (b_1, I) (middle row) and (a_1, I) (bottom row), and corresponding 3-DoF simulations (right-hand side) in a 3×3 grid.

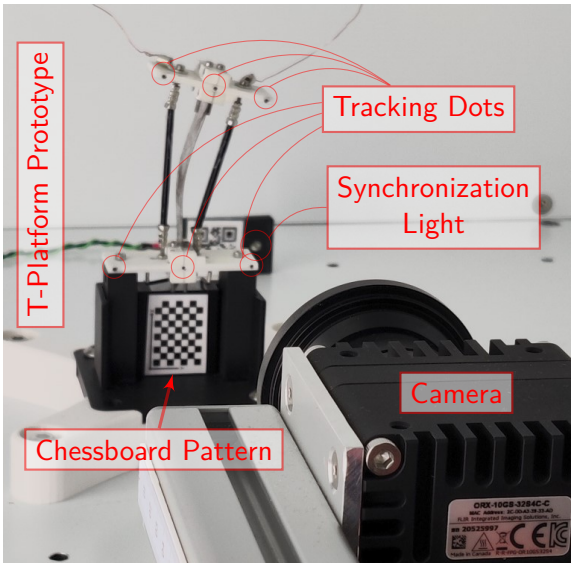

Figure 4.7.: Optical Tracking Setup.

publications, the model as shown here is the most general version and capable to match all tested experimental configurations. Nevertheless, some parameters may differ from publications as a result of the numerical optimization procedure.

In the remainder of this section, we will discuss first the experimental setup, followed by the calibration procedure and a summary of obtained results.

4.3.1. Overall Recording Setup

A schematic of the adopted experimental setup for experiments using Gen. B prototypes is shown in Figure 4.8. It consists of an optical measurement system (Camera: Oryx ORX-10GS-32S4C-C, Lens: Computar V2528-MPY) and two high-voltage amplifiers with integrated current sensing capabilities (Hivolt HA3B3-S ±3kV). The amplifiers are controlled by a Speedgoat Performance real-time target machine (Intel Core i7 4.2GHz CPU, 32GB RAM) with IO133 Analog I/O Module. The video data as well as the electrical measurements are collected on a Windows PC running MATLAB software. The setup allows us to collect video data at a rate of 120 frames per second, while the input voltages of the DEAs as well as the measured currents are sampled at 10 kHz ($T_s = 100\,\mu s$). After recording, a number of post-processing tasks are performed for camera calibration, temporal synchronization to electrical measurements, as well as extraction and tracking of points of interest over time, resulting in trajectories of optically measured T-Platform pose $\boldsymbol{q}[k]$ and DE lengths $\boldsymbol{l_{DE}}[k]$ as well as voltage $v_{DEj}[k]$ and current $i_{DEj}[k]$ signals acquired via electrical sensors.

An earlier version of the setup used for Gen. A prototypes had the same general structure, but used different amplifiers (HiVolt HA51U, Ultravolt 4HVA), a smartphone camera (Apple iPhone 8, 1920x1080 pixels, 30 frames per second) and a LabView-based recording system. This setup also lacks the capability to measure the electrical current at sufficient fidelity for self-sensing.

4.3.2. Optical Tracking Setup

The goal of the optical tracking setup is to measure the platform pose $\boldsymbol{q}$ over time while actuating the platform with high voltage, such that the measured pose can be related to the corresponding input voltages. While several systems are available commercially for optical motion tracking, many rely on placing physical objects, so-called targets, on the object to be tracked. This poses problems for our use case, since the added weight and space requirements interfere with the goal of a lightweight, soft and compact robot. Instead, a solution with minimal adaptations to the T-Platform was chosen, shown in Figure 4.7. Specifically, the tracking setup consists of a camera and black dots placed at defined locations on the 3D-printed prototype, to be identified and tracked using image recognition algorithms in software. In addition, a LED is placed in view of the camera. The pulsed signal used to control the LEDs is recorded together with the actuation voltages and simultaneously observed as light pulses by the camera, allowing a precise synchronization of system inputs $\boldsymbol{v}_{DE}$ to observed outputs $\boldsymbol{q}$.

After recording, the image recognition takes place in two stages. First, locations of tracking dots are initially specified manually and subsequently followed frame by frame using Kanade-Lucas-Tomasi (KLT) algorithm (Lucas et al. 1981; Tomasi et al. 1991), implemented in MATLAB by the `vision.PointTracker` class (*Track Points in Video Using Kanade-Lucas-Tomasi (KLT) Algorithm - MATLAB* 2024), resulting in sequences of points in sensor coordinates over time (pixel units). In the next step, the image-to-world conversion is performed, that is, pixel coordinates are transformed to real-world units in a cartesian coordinate system (units of mm). A calibrated mathematical model of the camera is required (Z. Zhang 2000; Heikkila et al. 1997), as well as the distance of tracked points to the camera in all three spatial directions. In some cases, this highly nonlinear transformation can be approximated as a so-called orthographic projection, resulting in a simple scaling factor (e.g. $1\,\mathrm{px} \mathrel{\hat{=}} 0.2\,\mathrm{mm}$). Usually, for best precision one should account for perspective distortion as well as lens distortion. This calibration is performed before an experiment by recording images of a printed out chessboard pattern with known dimensions in different orientations and using MATLAB function `estimateCameraParameters` (MathWorks 2024). The plane in which the T-Platform moves is defined for the camera by mounting another chessboard pattern in-plane, as shown in Figure 4.7. From the camera parameters, the tracked point locations in pixels as well as the position and orientation of the reference chessboard, we obtain the tracking dot locations in *world coordinates*, i.e. in a cartesian coordinate system defined by the reference chessboard. The platform pose $\boldsymbol{q}$

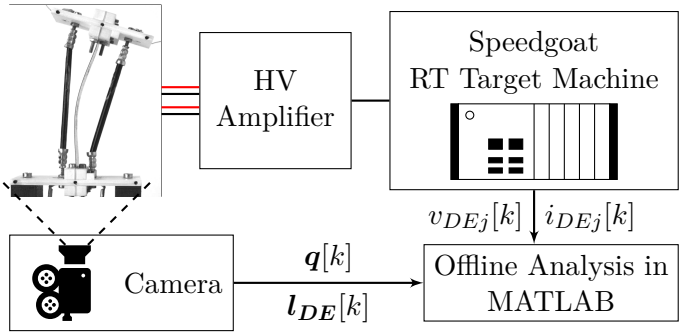

Figure 4.8.: Block diagram of the experimental setup (Prechtl et al. 2024).

can now be calculated without knowledge of kinematic parameters.

4.3.3. Automated Calibration Procedure

The goal of the automated calibration procedure is to obtain suitable values for all system parameters of the full-order dynamic T-Platform model (4.19) and the reduced-order model (4.26) based on measured trajectories of $\boldsymbol{q}$, $\boldsymbol{l}_{DE}$ and input voltages $\boldsymbol{v}_{DE}$. As a result of the highly nonlinear system behavior, simple approaches such as linear least squares fail to achieve satisfactory results, which is why a tailored multi-stage approach has been developed.

First, parameters $l_b, E, I, A, m_H, J_H, \epsilon_0, \epsilon_r, g, R_{ij}, R_{oj}, \alpha_{ej}$ are fixed to their known or directly measured values. All remaining values are obtained by formulating suitable nonlinear optimization problems (MATLAB `optimproblem/solve` and `fminsearch`) aimed at minimizing the deviation between model predictions and measurements. The kinematic parameters w_j, v_j, a_j and b_j are determined such that the integral squared error is minimized between measured DE lengths $\boldsymbol{l}_{DE}$ and those predicted by the kinematic model (4.7) through measured $\boldsymbol{q}$. During this step, the values of l_{crj} are assumed zero, since they cannot be determined optically. In the next step, the remaining parameters $b_{top}, l_{crj}, C_{jh}, \eta_j, d_x, d_y, d_\alpha$ are optimized by minimizing the integral squared error between the optically measured $\boldsymbol{q}$ and the value predicted by the full-order system model (4.19). For the reduced-order model (4.26), in an additional step the parameters $\tau_y, d_x, d_y, d_\alpha$ are tuned using the same optimization goal as in the previous step.

This multi-stage approach to parameter identification aims to produce physically reasonable results and minimize ambiguities resulting from the large number of parameters. Note that even the geometric parameters are identified through numerical optimization. The system is highly sensitive to small parameter variations and therefore does not tolerate even small errors resulting from manual measurements of geometric parameters. Thanks to the adopted procedure, a satisfactory agreement between model and experiments can be achieved, as will be discussed in the sequel.

4.3.4. Results

The predictive capabilities of the T-Platform model were examined in several experimental studies on many variations of physical prototypes. A first study (Baltes et al. 2022b) focused on the influence of design parameters on actuation performance, and compared model-predicted trends with experimental results. Later studies (Prechtl et al. 2022, 2024) focused on quantitatively predicting the trajectories of all DoFs during the experiment.

Static Validation

Figure 4.10 summarizes the results of Baltes et al. 2022b. The physical T-Platform prototype used was a "Generation A" (Gen. A) prototype, which differs from the later Gen. B prototypes in terms of general dimensions (Gen. A is significantly larger), size and manufacturing process of the rolled DE actuators, beam material as well as actuator mounting technique. Figure 4.9 highlights the different mounting techniques, showing the pivoting mechanism used in Gen. A as well as the bending mechanism used in Gen. B. The varied parameters include the thickness of the flexible backbone (corresponding to different second moments of area I) as well as the horizontal distance between actuator mounting

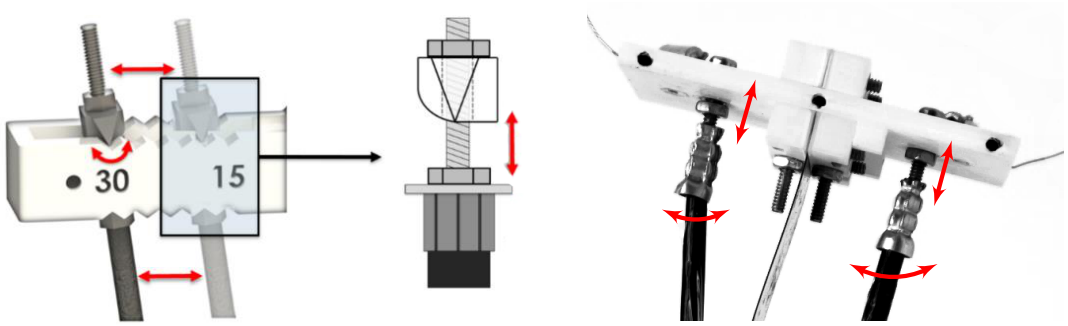

(a) Gen. A (Baltes et al. 2022b) (b) Gen. B

Figure 4.9.: Different mounting techniques on Gen. A and Gen. B prototypes.

points and backbone at upper and lower mounting positions (cf. Figure 4.10a). The system was actuated with alternating rectangular voltage signals varying between 0 kV and 3 kV, as shown in Figure 4.10b, and the deflection angle was recorded using the optical tracking setup described in Section 4.3.2, see Figure 4.10c. In the final step, the observed maximum deflection angles where compared to simulation results of the T-Platform model (4.19), achieving a remarkable agreement both in absolute values and prediction of trends, see Figure 4.10d. In addition, the study serves to confirm the analysis from Section 4.2.2 regarding the onset of bistability depending on various design parameters.

Dynamic Validation

In Prechtl et al. 2022, a similar Gen. A prototype was evaluated. Figure 4.11 shows calibration and validation results reproduced from the publication using the most recent T-Platform model as presented in this dissertation. The resulting parameters are listed in Table B.1. In order to avoid overfitting, separate calibration and validation experiments have been performed, using alternating rectangular and sinusoidal voltage signals, respectively (cf. Figure 4.11b). In row (c), the actuator lengths are compared between measured values and prediction of the kinematic model (4.7) based on the measured configuration $\boldsymbol{q}$. The upper half shows the absolute lengths, while the lower half displays the kinematic model error given as the difference between measured and predicted lengths. The results indicate a precise description of the system kinematics with errors in the sub-mm range. Finally, the response of the full system model Equation (4.19) is compared to the measured trajectories of $\boldsymbol{q}$ in row (d). Again, a precise description of the system behavior, albeit with minor deviations, is observed. These remaining differences can be justified through unmodeled effects (e.g. backbone material nonlinearities, simplified beam model) and external disturbances stemming from the electrical wires.

In Prechtl et al. 2024, the T-Platform model was calibrated on a Gen. B prototype (cf. Figure 4.12a), which differs significantly from the previous Gen. A specimens. The prototype is approximately half the size, uses backbones made from spring steel instead of PETG, and uses rigid actuator mounting with screws, relying on the bending of the soft actuator material in order to achieve motion (cf. Figure 4.9b). These differences pose an interesting challenge and justify a further evaluation of the T-Platform model. Since the model is physics-based, it is expected to also describe the dynamics of this

Table 4.1.: Dynamic Model Validation – Prediction errors (RMS)

	DoF	Calibration	Validation
Gen. A (Full Model)	q_x (mm)	3.28	4.32
	q_y (mm)	1.06	0.91
	α (°)	3.86	4.28
Gen. B (Full Model)	q_x (mm)	0.75	1.14
	q_y (mm)	0.15	0.21
	α (°)	2.01	2.32
Gen. B (Reduced Model)	q_x (mm)	0.64	1.09
	q_y (mm)	0.15	0.22
	α (°)	1.71	2.15

newer generation of T-Platform demonstrators, given a suitable calibration. Figure 4.12 shows calibration and validation results based on data from Prechtl et al. 2024, with corresponding parameters listed in Table B.2. In this study, a sinusoidal voltage signal was chosen for calibration, and a multi-modal sinusoidal signal was chosen for validation (cf. row (a)). Kinematic model performance is evaluated in row (b) and once again indicates a precise description of the system kinematics. Compared to the previous study (Prechtl et al. 2022), the lower absolute error magnitude results from an overall improved experimental setup. In row (d), both the full-order and reduced order models are evaluated and deliver a precise description of system behavior. The root-mean-square errors between predicted and actual poses are summarized in Table 4.1. Here, the reduced model offers slightly better performance, as it benefits from an additional calibration parameter τ_y. Further evaluations of model performance for different voltage inputs are presented in Section 5.2.3.

4.4. Summary: T-Platform Modeling

In this chapter, a physics-based and computationally efficient model of the planar T-Platform has been developed and validated on physical prototypes. It has been shown to possess predictive power regarding varying system parameters and input voltages. The onset of buckling has been analyzed in-depth, and it has been established as a generalization of negative-stiffness DE biasing in single-DoF actuators. Staying faithful to the concept of a modular soft robot, also the T-Platform model is modular in the sense that it can be easily used as a building block for models of stacked T-Platforms. The suitability for control applications is proven in publications by Massenio et al. 2022; Soleti et al. 2023, 2024, which explore control strategies for the T-Platform based on the modeling results of this chapter. Furthermore, the model presented in this chapter serves as the basis for the development of a realtime pose estimation algorithm, detailed in Chapter 5, as well as realtime control strategies for the T-Platform (Soleti et al. 2023, 2024). First steps towards a three-dimensional T-Platform and corresponding model have recently been published by Kunze et al. 2024, presently using a rigid backbone with a ball joint in place of a flexible beam.

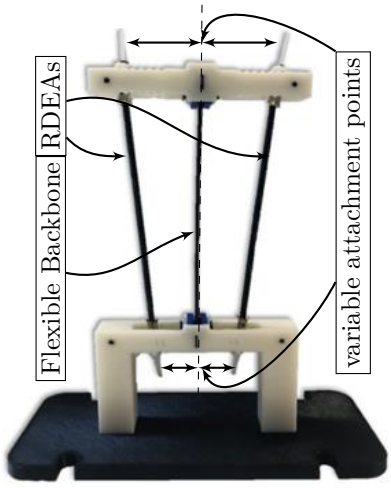

(a) Lab prototype of the T-Platform (Gen. A).

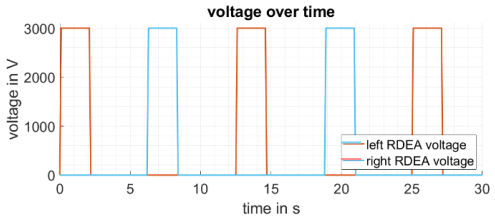

(b) Applied voltage signals.

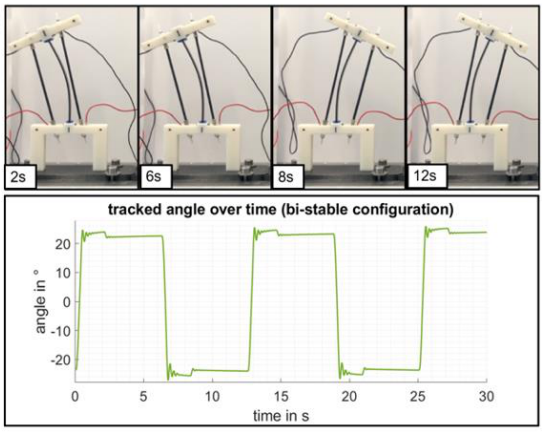

(c) Optically measured bending angle over time.

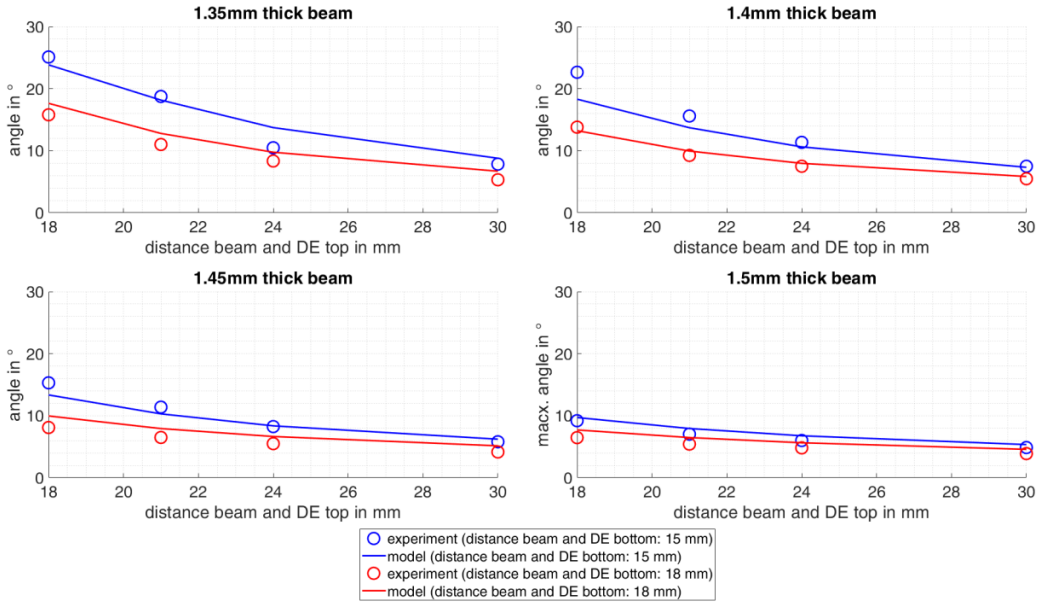

(d) Maximum deflection angle depending on attachment points.

Figure 4.10.: Experimental investigation of the deflection angle depending on the attachment points for different beams, and comparison with model data (Baltes et al. 2022b).

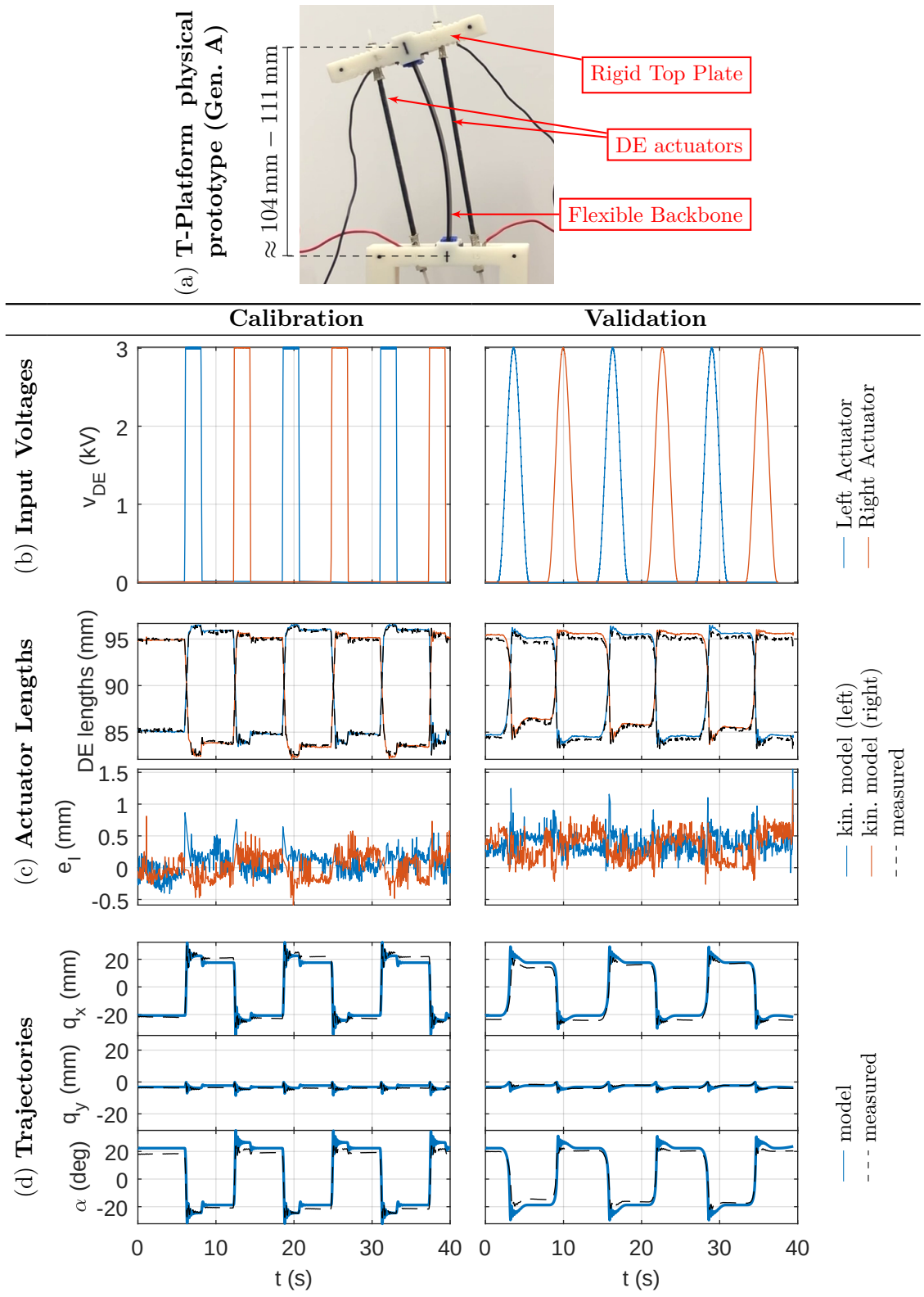

Figure 4.11.: Experimental validation of the dynamic T-Platform model on a Gen. A physical prototype, based on data first published in (Prechtl et al. 2022).

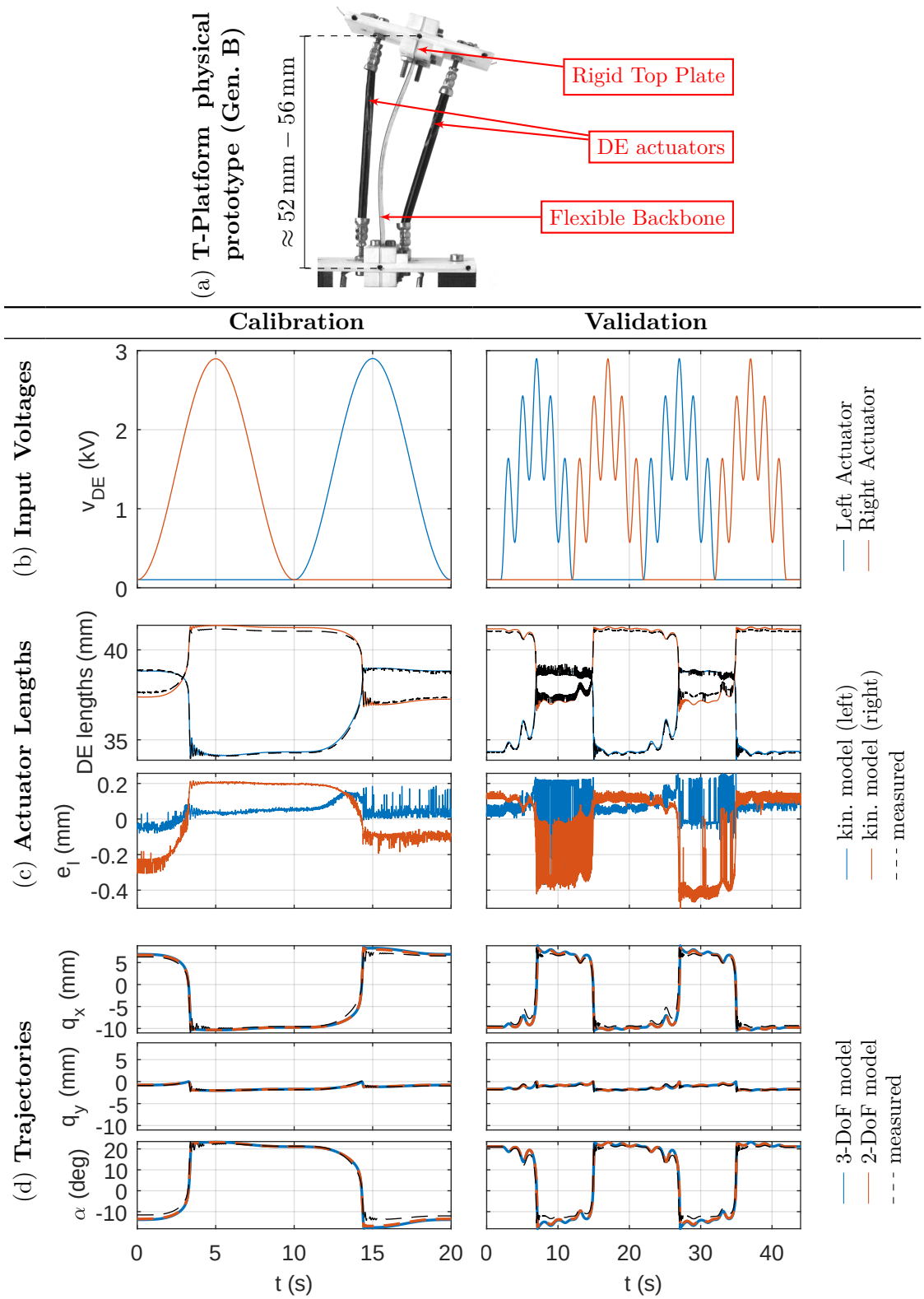

Figure 4.12.: Experimental validation of the dynamic T-Platform model on a Gen. B physical prototype, based on data first published in (Prechtl et al. 2024).

5. System-Level Self-Sensing for Underactuated Soft Robots

In this chapter, a system-level self-sensing scheme for a DE driven soft robotic system is introduced. As introduced in Section 2.2, the case study consists of a planar module driven by a pair of pre-tensioned rolled DEAs, capable of bending and translation motions. The proposed self-sensing architecture relies on the combination of two functional blocks, i.e., an actuator-level estimation scheme and a system-level state observer, based on the system model from Section 4.1. The former estimates in real time the electrical capacitance of the two actuators via recursive least squares, and uses this information to reconstruct their lengths, based on measurements of DEA voltage and current signals. Since the underactuated and nonlinear nature of our system makes it not possible to uniquely reconstruct the robot configuration solely via DEA lengths information, a second functional block consisting of an extended Kalman filter (EKF) is introduced. The EKF receives as inputs actuator lengths as well as the actuation voltages, and provides an estimation of the system mechanical configuration and generalized velocity while also accounting for model nonlinearities. After presenting the novel architecture, an extensive experimental validation campaign is conducted, in which the estimated configuration is compared with measurements acquired with a camera system. It is shown that the robot configuration can be estimated precisely for a variety of input trajectories with sub-mm / sub-degree accuracy. In addition, the system-level self-sensing scheme permits not only to estimate changes in the robot configuration which are caused by actuation voltage, but also by unmodeled external loads.

Previous iterations of the work presented in this chapter have been published at Prechtl et al. 2022, 2024. In this chapter, the overall architecture of the proposed algorithm is described. Subsequently, an extensive experimental campaign with various actuation signals and external mechanical loads is presented to validate the method. The real-time feasibility is investigated and a reduced-order estimator formulation lowering the real-time computational burden without compromising accuracy is introduced. In addition to the previously published results, also the findings related to practical actuator-level self-sensing are discussed.

5.1. System-Level Self-Sensing Architecture

The goal of the system-level self-sensing architecture is to estimate in real time the system state, consisting of the robot configuration $\boldsymbol{q}$ and corresponding velocity $\dot{\boldsymbol{q}}$, based on available measurements of the DEA voltages $\boldsymbol{u}$ and lengths $\boldsymbol{l_{DE}}$, as shown in Figure 5.1. The overall architecture is based on a two-level estimation process. At actuator level, the voltage and current measurements are used to estimate the individual actuator lengths $\boldsymbol{l_{DE}}$. At system level, those actuator lengths serve as measured outputs of a model-based observer for the system state. Both processes are described in this section.

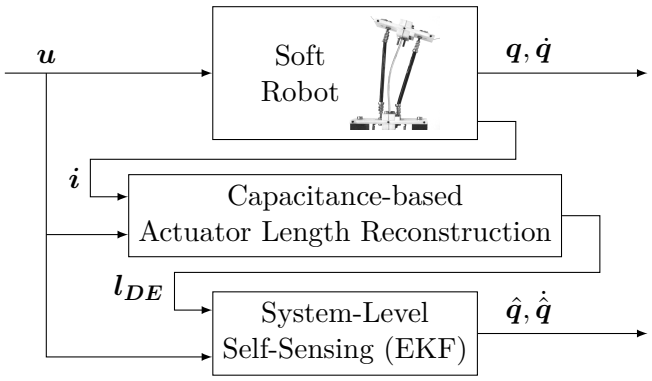

Figure 5.1.: Block diagram of the system-level self-sensing architecture (Prechtl et al. 2024).

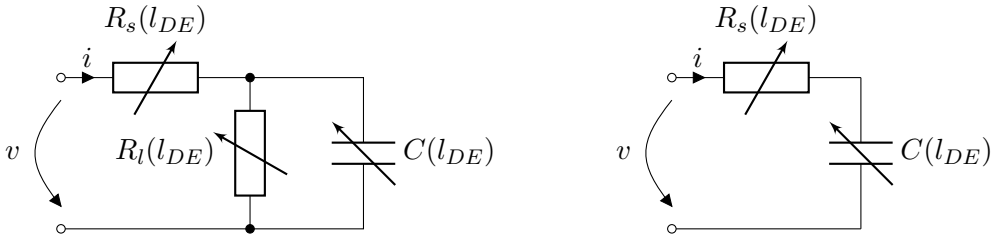

(a) Full Model (b) RC series model

Figure 5.2.: Electrical models of self-sensing DEAs.

5.1.1. Estimation of the DEA Lengths via Electrical Measurements

As mentioned in Section 1.2.1, the direct coupling between deformation and capacitance of a DEA can be exploited to measure the deformation by means of measuring the capacitance. In this section, details of the capacitance estimation are discussed, following the works of Rizzello et al. 2020b.

Figure 5.2a shows a lumped-parameter electrical model of DEA, consisting of a series resistance R_s, a capacitance C and a leakage resistance R_l. The series resistance combines the contributions of connection cables (independent of actuator deformation) and resistance of the flexible electrodes (deformation-dependent). The leakage resistance describes how much residual current flows through the insulating dielectric that separates the electrodes. Finally, C denotes the total capacitance of the actuator. All shown components depend on the DEA deformation l_{DE}, and can, in principle, be estimated through measurements of voltage v and current i. Nevertheless, only the capacitance C typically shows an invertible dependency on the actuator length.

The transfer function relating measured current i to input voltage v is given as the conductance

$$Y_1(s) = \frac{sC + \frac{1}{R_l}}{sCR_s + \frac{R_s}{R_l} + 1} \tag{5.1}$$

for the model shown in Figure 5.2a, while the simplified model for the model shown in

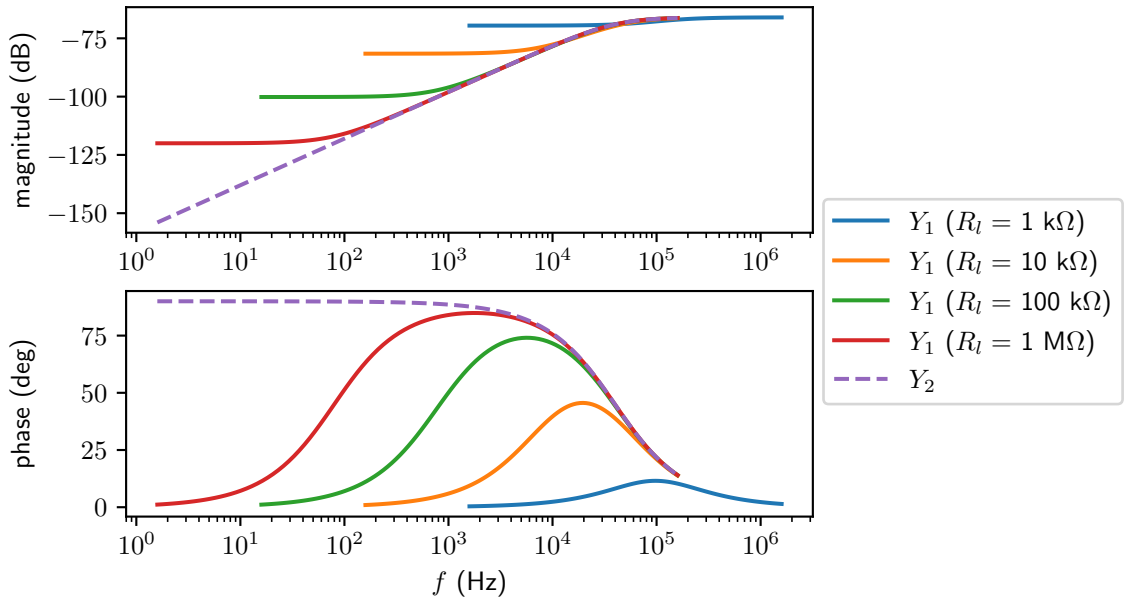

Figure 5.3.: Bode plot of Y_1 and Y_2 transfer functions for realistic component values ($R_s = 2\,\mathrm{k\Omega}$, $C = 2\,\mathrm{nF}$).

Figure 5.2b is described by

$$Y_2(s) = \frac{sC}{sCR_s + 1}. \tag{5.2}$$

Typical frequency responses of $Y_1(s)$ and $Y_2(s)$ assuming constant electrical parameters are shown in Figure 5.3. It is noted that both circuits possess a high-pass characteristic. In addition, increasing values of the leakage resistance R_l result in increasingly similar frequency responses. Since R_l is typically larger than $1\,\mathrm{M\Omega}$, the series model (cf. Figure 5.2b) is a sufficiently accurate approximation.

In order to estimate the electrical parameters during actuation, an additional voltage signal is added onto the actuation voltage. If the frequency of this additional signal is chosen large enough, the high-pass characteristics of the electrical circuit will result in a sufficiently large current signal. At the same time, the estimation strategy described in the following relies on the fact that the mechanical actuator bandwidth is limited to lower frequencies. Therefore, a high-frequency voltage injection will have a negligible effect on the mechanical deformation and thus allow us to assume constant deformation, and therefore constant electrical parameters in a limited time interval.

If we assume that each DEA can be modeled as an RC series circuit, discretization of the circuit equation $I(s) = Y_2(s)U(s)$ via pre-warped Tustin method leads to

$$\begin{aligned} v_{DEj}[k] - v_{DEj}[k-1] = \theta_{1j}[k]\,(i_{DEj}[k] - i_{DEj}[k-1]) \\ + \theta_{2j}[k]\,(i_{DEj}[k] + i_{DEj}[k-1])\,, \end{aligned} \tag{5.3}$$

$$R_{DEj}[k] = \theta_{1j}[k], \quad C_{DEj}[k] = \frac{\tan(\pi f_e T_s)}{2\pi f_e}\frac{1}{\theta_{2j}[k]}, \tag{5.4}$$

with i_{DEj}, R_{DEj}, and C_{DEj} denoting electric current, instantaneous series electrical resistance, and instantaneous electrical capacitance of actuator j, respectively, T_s is the

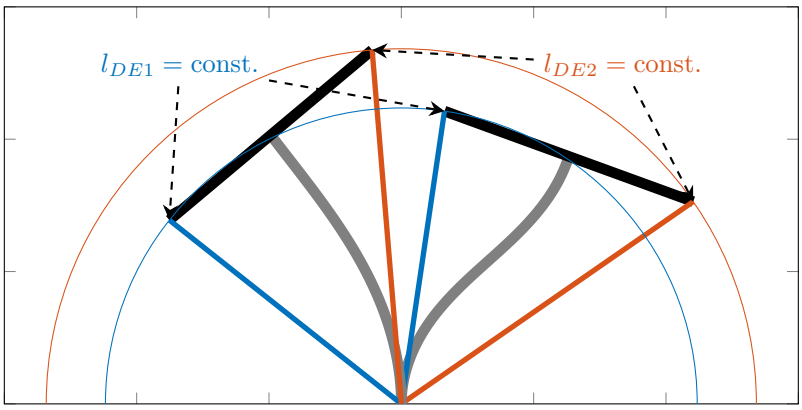

Figure 5.4.: Illustration of the ambiguous kinematic relationship between platform poses and actuator lengths.

sampling time, and k denotes a discrete-time index variable. The injected sensing frequency f_e appears due to the Tustin discretization, which is pre-warped at f_e to ensure that distortions due to the Tustin discretization are minimized around that frequency. In Figure 5.5a, an example of an actuation voltage superimposed with a sensing signal at f_e is shown. Since both R_{DEj} and C_{DEj} explicitly depend on the DEA deformation (Rizzello et al. 2016, 2020b), the $v_{DEj} - i_{DEj}$ relationship is directly affected by the actuator mechanical state. Equation (5.3) corresponds to a linear regression problem for the unknown (slowly time-varying) parameters θ_{1j} and θ_{2j} (related to R_{DEj} and C_{DEj}), which is solved in real time based on online measurements of voltage and current via recursive least squares techniques (Rizzello et al. 2020b; Nelles 2001). The estimated capacitance C_{DEj} can be used to reconstruct the corresponding DEA lengths l_{DEj}, as described in Section 5.2.1.

5.1.2. Estimation of the Robot Configuration via Self-Sensing Data

In this section, the goal of estimating the T-Platform configuration $\boldsymbol{q}$ based on available actuator lengths $\boldsymbol{l_{DE}}$ and squared voltages $\boldsymbol{u}$ is addressed. In principle, this objective, could be seen as an inverse kinematics problem, i.e., reconstruct $\boldsymbol{q}$ based on $\boldsymbol{l_{DE}}$ by inverting (4.7). Since the T-Platform represents a 3-DoF parallel kinematic structure, and only two independent measurements are available, equation $\boldsymbol{l_{DE}}(\boldsymbol{q})$ cannot be uniquely inverted solely on the basis of (4.7). Fig. 5.4 illustrates this kinematic ambiguity.

In the example given in Fig. 5.4, the end-points of the rigid top plate can move freely along two circular trajectories, while the actuator lengths stay constant (note: some geometric parameters have been set to zero for illustrative purposes). This results in an unavoidable ambiguity when one wants to predict the configuration of the top plate by only relying on the RDEAs lengths Equations (4.8) and (4.9), and is closely related to the fact that the T-platform is underactuated. This ambiguity can be practically solved by also considering that, alongside kinematic relationships, an equilibrium of forces and moments must also be attained between the flexible backbone and the actuators. It is therefore necessary to consider both kinematic and dynamic information of the soft robot in order to achieve the system-level self-sensing.

One possible solution to this underdetermined problem is to eliminate q_x via kinematic constraint (4.21), and solve (4.7) numerically for the two remaining DoFs. Despite seeming appealing, this approach fails in practice due to numerical issues (a more detailed discussion is postponed to Section 5.2.2). On the other hand, while the dynamic model from Section 4.1 well captures the open loop system response, it fails to reach the fidelity needed for closed-loop control, since it cannot anticipate unavoidable external disturbances or parameter uncertainties.

To overcome the above-mentioned shortcomings, we adopt a method that combines DEA length estimation with the dynamic model from Section 4.1, in such a way to have enough information to resolve the kinematic ambiguity while improving the precision and robustness. To this end, we recall both full-order (4.19) and reduced-order (4.26) models, which provide two nonlinear state-space description of the T-Platform by considering the squared voltage $\boldsymbol{u}$ as input and $\boldsymbol{l_{DE}}$ as measured output. The models expressed in this form offer a basis to use an observer-based approach, making use of the estimated actuator lengths $\boldsymbol{l_{DE}}$ from Section 5.1.1 as measured outputs. The EKF is a natural choice for this estimation task, due to its ability to perform state estimation in the presence of nonlinearities as well as its ease of implementation. For the EKF framework, we consider a scenario in which the system dynamics is expressed in continuous time while measurements are available in discrete time, given by

$$\begin{aligned} \dot{\boldsymbol{x}}(t) &= \boldsymbol{f}(\boldsymbol{x}(t), \boldsymbol{u}(t)) + \boldsymbol{w_f}(t) \\ \boldsymbol{z}[k] &\coloneqq \boldsymbol{h}(\boldsymbol{x}(kT_s)) + \boldsymbol{w_h}(kT_s) \end{aligned} \tag{5.5}$$

where time dependency of each variable has been made explicit for the ease of clarity, with round and squared brackets denoting continuous and discrete time, respectively. In (5.5), $\boldsymbol{f}$ and $\boldsymbol{h}$ can correspond to either the full system dynamics $\boldsymbol{f_x}$ and measurement model $\boldsymbol{h_x}$ (cf. (4.19)), or the reduced system dynamics $\boldsymbol{f_\xi}$ and measurement model $\boldsymbol{h_\xi}$ (cf. (4.26)), respectively. Normally distributed system noise $\boldsymbol{w_f} \sim \mathcal{N}(0, \boldsymbol{S_f})$ and measurement noise $\boldsymbol{w_h} \sim \mathcal{N}(0, \boldsymbol{S_h})$ is considered. Since the system dynamics are highly nonlinear and sensitive to discretization strategy, the so-called continuous-discrete EKF Lewis et al. 2008 is deemed the most suitable EKF variant for this estimation task, as it performs the prediction step by numerically integrating the continuous system dynamics until new measurements become available, and then computes a discrete update step. The *apriori* state $\hat{\boldsymbol{x}}^-[k]$ and covariance $\boldsymbol{P}^-[k]$ estimates are computed as the solution of

$$\dot{\hat{\boldsymbol{x}}} = \boldsymbol{f}(\hat{\boldsymbol{x}}, \boldsymbol{u}(t)), \tag{5.6a}$$

$$\dot{\boldsymbol{P}} = \boldsymbol{A}(\hat{\boldsymbol{x}}, t)\boldsymbol{P} + \boldsymbol{P}\boldsymbol{A}^\intercal(\hat{\boldsymbol{x}}, t) + \boldsymbol{S_f}, \tag{5.6b}$$

in the interval $t \in \Big[(k-1)T_s \quad kT_s\Big]$ starting from the last estimates of $\hat{\boldsymbol{x}}^+[k-1]$ and $\boldsymbol{P}^+[k-1]$, where $\boldsymbol{S_f}$ is the the system noise covariance and $\boldsymbol{A}(\hat{\boldsymbol{x}}, t)$ is defined as

$$\boldsymbol{A}(\hat{\boldsymbol{x}}, t) = \left.\frac{\partial \boldsymbol{f}(\boldsymbol{x}, \boldsymbol{u})}{\partial \boldsymbol{x}}\right|_{\boldsymbol{x}=\hat{\boldsymbol{x}}, \boldsymbol{u}=\boldsymbol{u}(t)}. \tag{5.7}$$

In this work, we will consider several possible methods to approximate the solution of (5.6) (cf. Section 5.2.4). The update step computes the Kalman gain matrix $\boldsymbol{K}[k]$ via the predicted state $\hat{\boldsymbol{x}}^-[k]$ and the covariance matrix $\boldsymbol{P}^-[k]$, and applies a correction to the

aposterioi estimates $\hat{\boldsymbol{x}}^+[k]$ based on the predicted error of the measurement model and $\boldsymbol{P}^+[k]$, i.e.,

$$\boldsymbol{K}[k] = \boldsymbol{P}^-[k]\boldsymbol{C}^\intercal[k]\left(\boldsymbol{C}[k]\boldsymbol{P}^-[k]\boldsymbol{C}^\intercal[k] + \boldsymbol{S_h}\right)^{-1}, \tag{5.8a}$$

$$\hat{\boldsymbol{x}}^+[k] = \hat{\boldsymbol{x}}^-[k] + \boldsymbol{K}[k]\left(\boldsymbol{z}[k] - \boldsymbol{h}(\hat{\boldsymbol{x}}^-[k])\right), \tag{5.8b}$$

$$\boldsymbol{P}^+[k] = \left(\boldsymbol{I} - \boldsymbol{K}[k]\boldsymbol{C}[k]\right)\boldsymbol{P}^-[k]\left(\boldsymbol{I} - \boldsymbol{K}[k]\boldsymbol{C}[k]\right)^\intercal + \boldsymbol{K}[k]\boldsymbol{S_h}\boldsymbol{K}^\intercal[k], \tag{5.8c}$$

with $\boldsymbol{C}[k]$ given by

$$\boldsymbol{C}[k] = \left.\frac{\partial \boldsymbol{h}(\boldsymbol{x})}{\partial \boldsymbol{x}}\right|_{\boldsymbol{x}=\hat{\boldsymbol{x}}^-(kT_s)}. \tag{5.9}$$

5.2. Experimental Validation

After calibration of model parameters, in this section the proposed self-sensing schemes are evaluated based on the recorded experimental data. It is first shown that a simple numerical inversion of the 2-DoF kinematic model is not feasible. Afterwards, the system-level self-sensing method is compared to the open-loop model response for a wide range of experiments. Finally, the realtime performance of different possible discretizations is evaluated in terms of computation speed and estimation quality.

The results shown here are based on experimental data published in Prechtl et al. 2024 and make use of the T-Platform model calibrated in Section 4.3, with parameters listed in Table B.2.

5.2.1. Results of Actuator-Level Self-Sensing

Figure 5.5 shows the results of actuator-level self-sensing. In Figure 5.5a, the actuator lengths are shown together with the input voltages and resulting capacitances estimated according to the scheme described in Section 5.1.1. As shown in the figure, the voltage signals include a high frequency component at $f_e = 1\,\mathrm{kHz}$ and an amplitude of $100\,\mathrm{V}$. The estimated capacitances generally follow the behavior of the corresponding actuator lengths. However, there is an apparent influence of the actuation voltage on the estimated capacitance as well. The areas where this effect is most pronounced have been highlighted in light blue and light red in the figure, showing a decrease of the capacitance together with a decline of the actuation voltage, while the actuator length varies only a negligible amount. Since this effect is systematic, it can be compensated using a phenomenological description of the actuator length Rizzello et al. 2020b. An accurate fit is obtained via function

$$l_{DEj}(C_{DEj}, v_{DEj}) = \sum_{m=0}^{1}\sum_{n=0}^{3} p_{jmn} C_{DEj}^m v_{DEj}^n, \tag{5.10}$$

with coefficients p_{jmn} calibrated on the experimental data based on a least squares fit. The resulting functions $l_{DEj}(C_{DEj}, v_{DEj})$ are shown in Figure 5.5b. Dashed black lines denote constant levels of the surface (i.e. constant actuator lengths), while solid black lines denote paths of constant voltage. After calibration, the estimated DEA lengths well reproduce the optical measurements, as shown in Figure 5.5c.

Since (5.10) implies a linear relationship between capacitance and actuator length, the equation can be rearranged to express the capacitance C_{DEj} as a function of l_{DEj} and v_{DEj}, resulting in an apparent cubic relationship between voltage and capacitance. This observation seems to contradict the physics-based actuator model from Section 3.1, which predicted a linear dependency between actuator capacitance and actuator length only, cf. (3.57). We can therefore conclude that the difference is due to non-ideal or unmodeled behavior of the RDEAs. Further investigations are necessary to resolve this disagreement, which occurs only at high voltage.

5.2.2. Results of Purely Kinematic System-Level Self-Sensing

As mentioned in Section 5.1.2, one conceivable solution of the estimation problem consists of numerically solving for $\boldsymbol{q}$ the nonlinear system of three equations given by (4.7) and (4.21), where $\boldsymbol{l_{DE}}$ is known through the capacitance while τ_y is calibrated to best fit the data. As shown in Figure 5.6, this approach fails in practice. These plots are obtained by solving (4.7) and (4.21) for the calibration experiment Figure 4.12 at each timestep using `fsolve()`, with initial guesses chosen based on either the measured reference trajectory at the current time (Figure 5.6a), or based on the previous estimate (Figure 5.6b). Further numerical investigations revealed the reasons for this inaccuracy, i.e., the Jacobian of the transformation from $\boldsymbol{r}$ to $\boldsymbol{l_{DE}}(\boldsymbol{q}(\boldsymbol{r}))$ exhibits a nearly-singular behavior in several points of the computed trajectory. This is illustrated in Figure 5.6c, where the determinant $\det\left(\frac{\partial \boldsymbol{l}_{DE}}{\partial \boldsymbol{r}}\right)$ of the Jacobian is shown as a function of the configuration $\boldsymbol{r}$. The intersection with the zero plane forms a curve on which the mapping is non-invertible. As a result, finding $\boldsymbol{r}$ from $\boldsymbol{l}_{DE}$ results in different trajectories in Figure 5.6 obtained for different initial guesses.

5.2.3. Results of EKF-based System-Level Self-Sensing

For a qualitative and quantitative evaluation of the system-level self-sensing scheme, experiments with different voltage trajectories were performed and the response of the underlying open-loop model as well as the proposed observer-based method was evaluated. Two different versions of the methods are considered, in which the estimation is performed either with the full model (4.19) or with its reduced version (4.26), denoted as EKF3 and EKF2 respectively. In both cases, the update frequency is fixed at 1 kHz, while matrices $\boldsymbol{S_f}$ and $\boldsymbol{S_h}$ are tuned via numerical optimization with the aim of minimizing the integral squared difference between measured and estimated $\boldsymbol{q}$.

Figure 5.7 evaluates the proposed self-sensing schemes for different experiments, and compares them to the open-loop model response. The input voltages in the first column represent the low-frequency component of the driving voltage, without considering the high-frequency injection needed for capacitance sensing for better visualization. In the second and third columns, the optically measured configuration over time (black dashed lines) is compared to the estimated trajectories (solid colored lines) according to the open-loop model (4.19) (center column) and according to the proposed self-sensing scheme (right column). Experiments (a)-(c) explore the system behavior for different voltage waveforms without any external disturbance, while in (d) the T-Platform was pushed by hand without applying any actuation voltage. The trend is generally well captured by the open-loop model in the undisturbed experiments (a)-(c), even though the precise post-

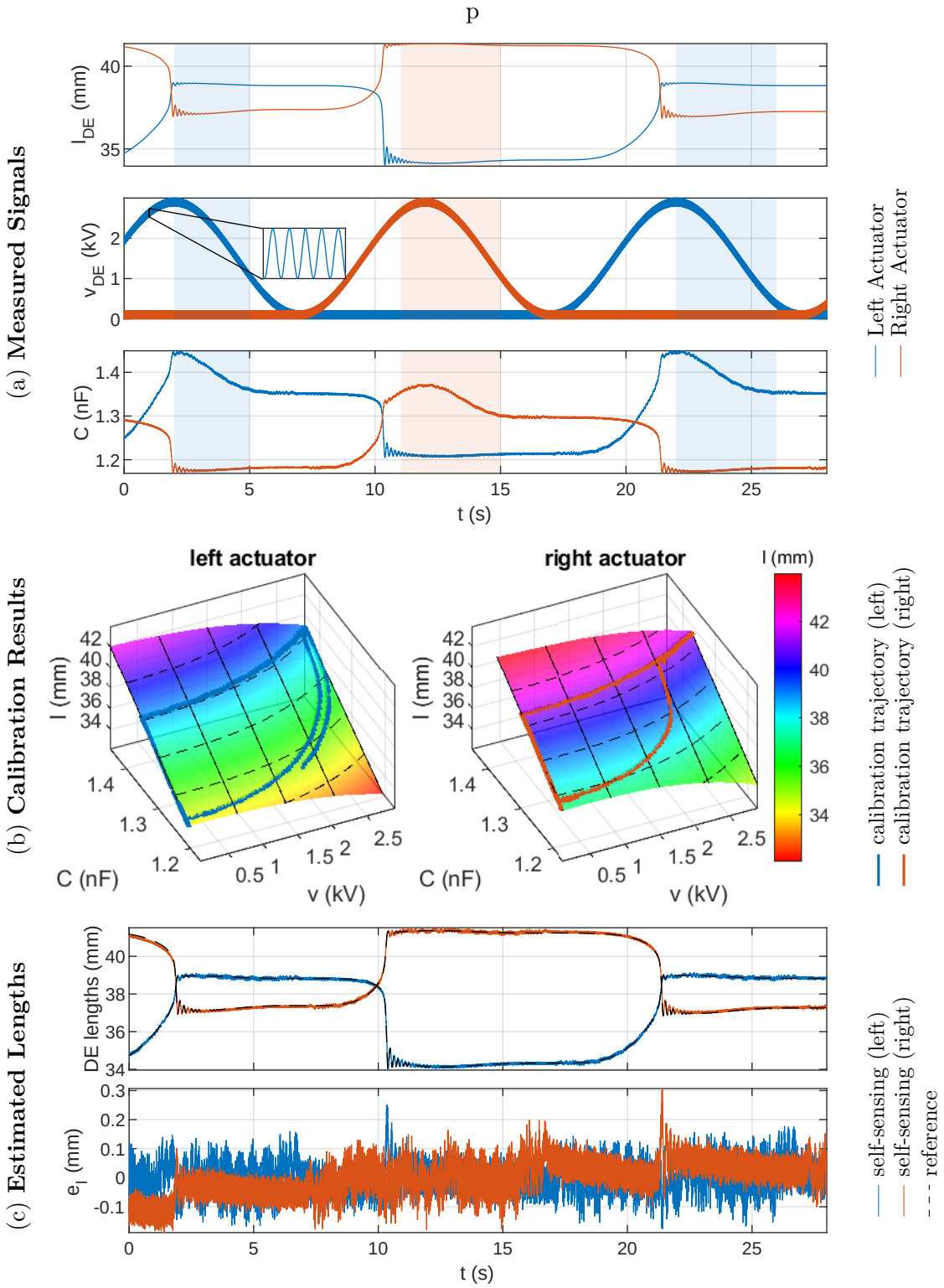

Figure 5.5.: Results of capacitance-based actuator length estimation (so-called actuator-level self-sensing).

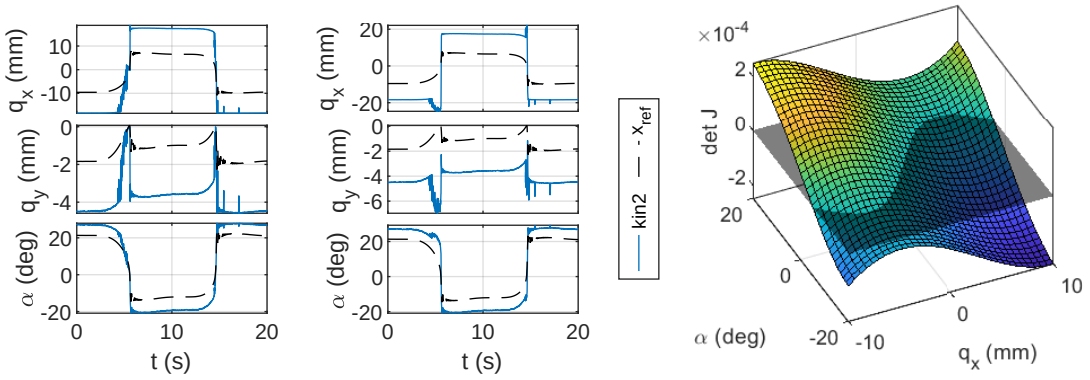

(a) (b) (c)

Figure 5.6.: Purely kinematic estimation scheme on the calibration dataset fails to provide useful estimates. Solutions shown for initial guesses at each timestep based on measured reference trajectory (a) and on previous estimate (b) (Prechtl et al. 2024). The mapping between lengths $\boldsymbol{l}_{DE}$ and reduced configuration $\boldsymbol{r}$ is non-invertible, as shown in (c).

buckling behavior is sometimes mispredicted. In addition, the open-loop model cannot account for external forces in (d), and therefore estimate no displacement over time, as expected. The proposed self-sensing schemes, on the other hand, follow the system motion at all times, while also providing more precise numerical estimations than the open-loop model. A high level of robustness is achieved, and it is difficult to visually distinguish the differences between EKF3 and EKF2 schemes. This aspect becomes more clear in Table 5.1, which lists the root mean squared (RMS) errors for all three degrees of freedom corresponding to the experiments in Figure 5.7, as well as the calibration experiment labeled *Sine*. The table confirms the visual observations, even though the EKF3 scheme generally performs slightly better than EKF2, as expected. The superior robustness of self-sensing compared to the open-loop model can be explained as follows. Thanks to the EKF, the configuration $\boldsymbol{q}$ estimated by the open-loop model is corrected in real time via output $\boldsymbol{l_{DE}}$, which in our case is accurately reconstructed through voltage and current measurements as shown in Figure 5.5. The $\boldsymbol{q}$ estimated by the EKF is thus heavily based on the kinematic model $\boldsymbol{l_{DE}}(\boldsymbol{q})$, while the dynamic model is mostly used to solve the kinematic ambiguity due to the underactuation. Therefore, we can expect the proposed self-sensing approach not to be highly sensitive to changes in the dynamic model parameters or to external disturbances, as long as $\boldsymbol{l_{DE}}$ is accurately estimated and provided that kinematic model $\boldsymbol{l_{DE}}(\boldsymbol{q})$ is calibrated with good precision.

5.2.4. Real-Time Considerations

Almost all operations required by the system-level self-sensing scheme in Section 5.1 are naturally formulated in discrete time, except for (5.6). To enable effective implementation of the estimation method on real-time digital architectures, efficient ways to numerically approximate the solution of (5.6) are required. In Figure 5.10, a study is conducted to compare different numerical integration methods at various update frequencies in terms

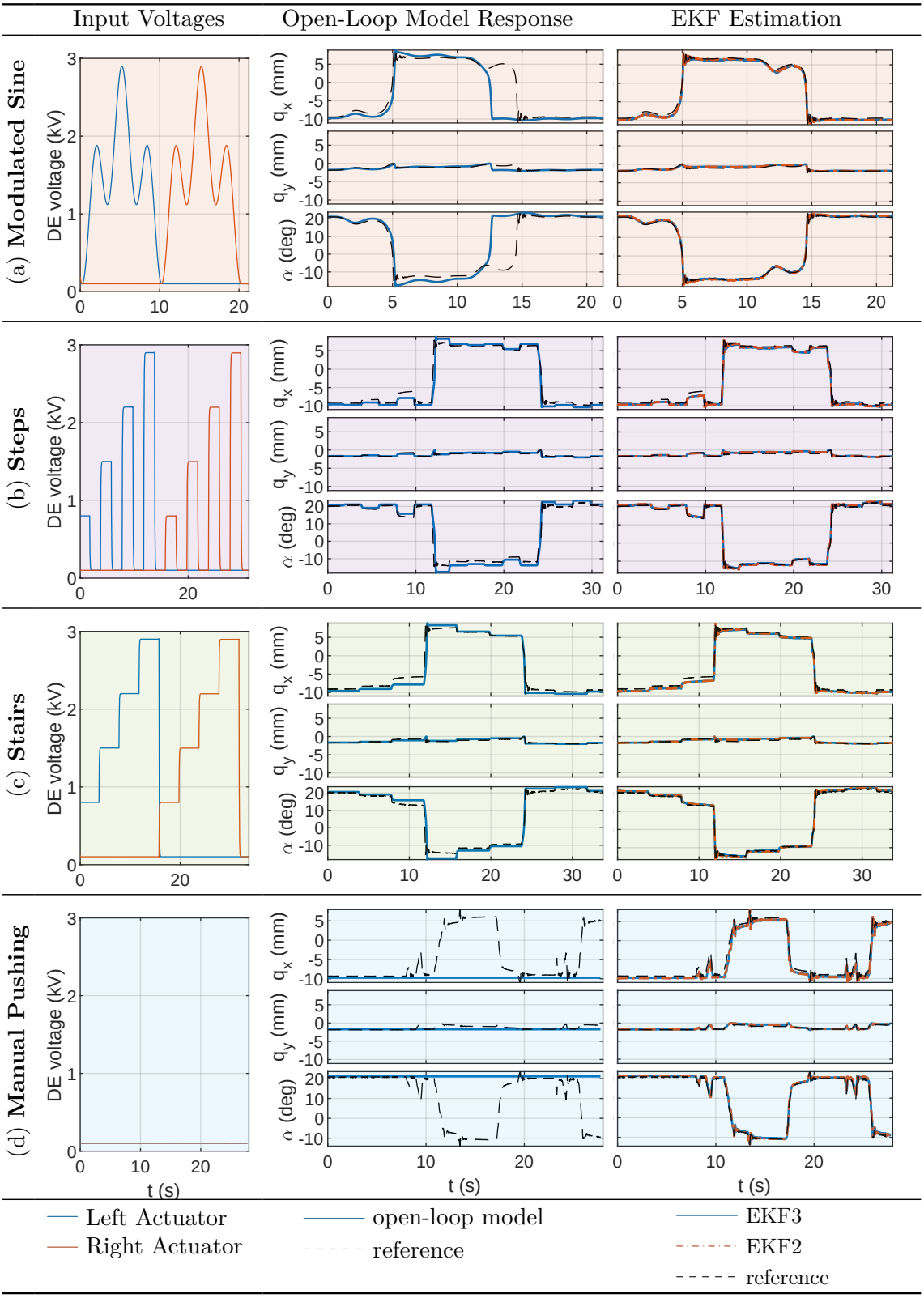

Figure 5.7.: Evaluation of the proposed self-sensing schemes (EKF3/EKF2) for different experiments (a)-(d) and comparison to the open-loop model predictions (Prechtl et al. 2024).

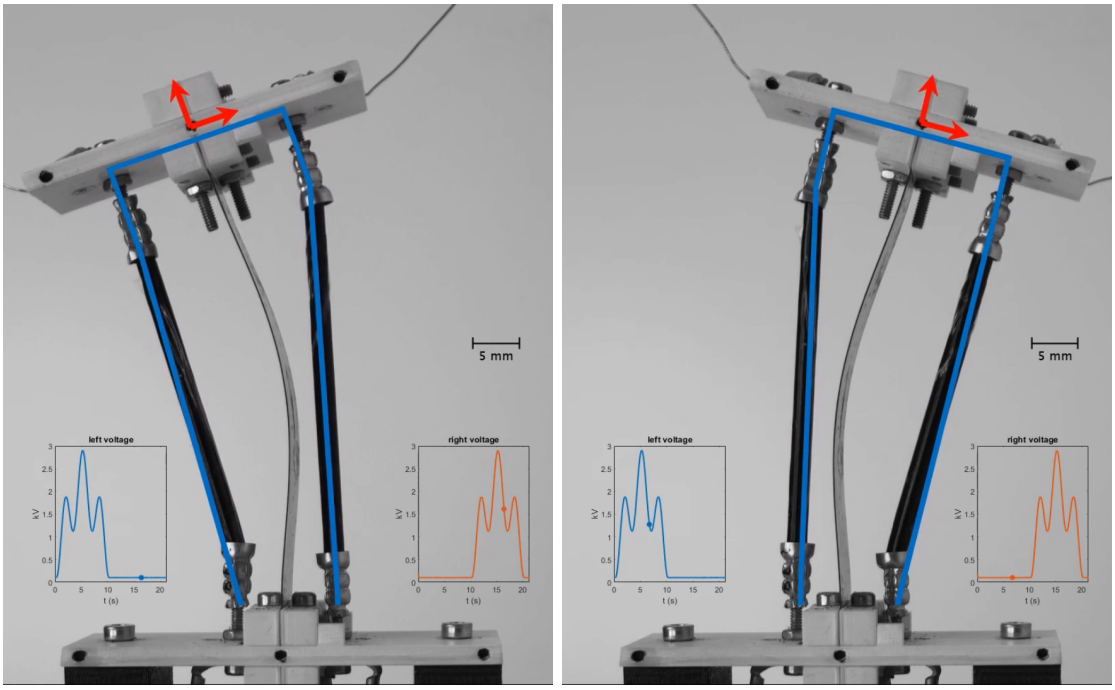

Figure 5.8.: Video frames from an experiment showing movement of the structure during high-voltage actuation (cf. Figure 5.7a; Prechtl et al. 2024).

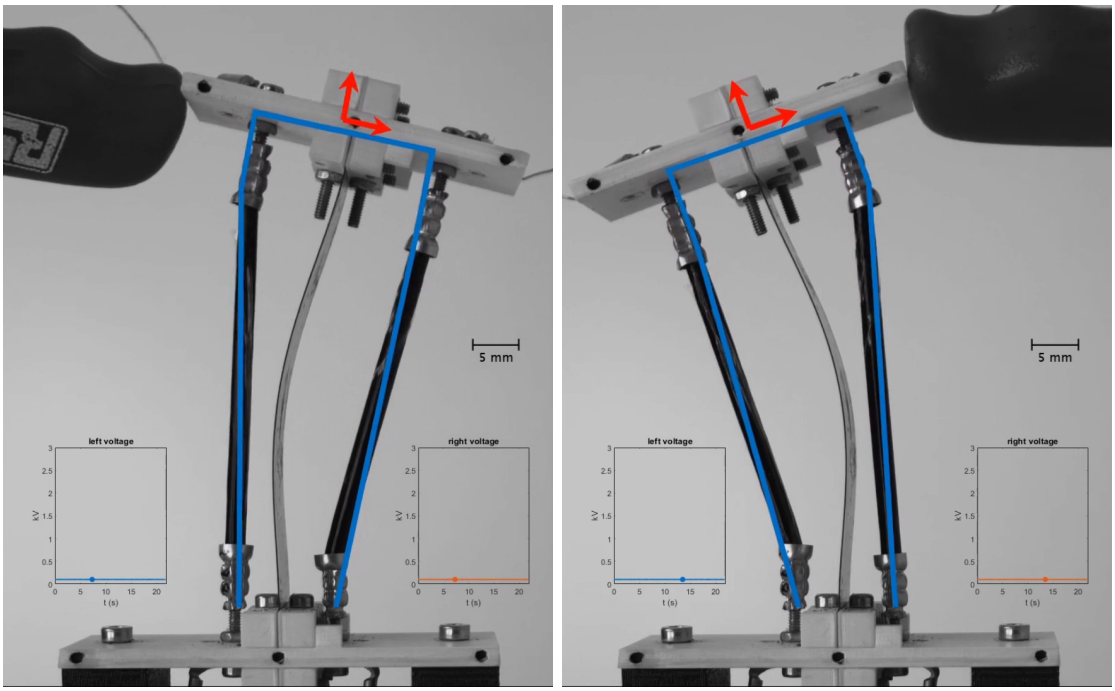

Figure 5.9.: Video frames from an experiment with forced movement caused by a pushing tool (cf. Figure 5.7d; Prechtl et al. 2024).

Table 5.1.: System-Level Self-Sensing – Prediction errors (RMS)

	DoF	Model	EKF3	EKF2
Sine	q_x (mm)	0.74	0.50	0.48
	q_y (mm)	0.15	0.22	0.20
	α (°)	1.82	0.44	0.63
Modulated Sine	q_x (mm)	4.49	0.60	0.55
	q_y (mm)	0.44	0.25	0.23
	α (°)	9.12	0.47	0.59
Steps	q_x (mm)	1.16	0.65	0.61
	q_y (mm)	0.20	0.28	0.26
	α (°)	2.31	0.50	0.60
Stairs	q_x (mm)	1.19	0.65	0.63
	q_y (mm)	0.23	0.27	0.25
	α (°)	2.24	0.47	0.58
Manual Pushing	q_x (mm)	8.13	0.98	0.97
	q_y (mm)	0.69	0.24	0.22
	α (°)	16.39	0.79	0.91

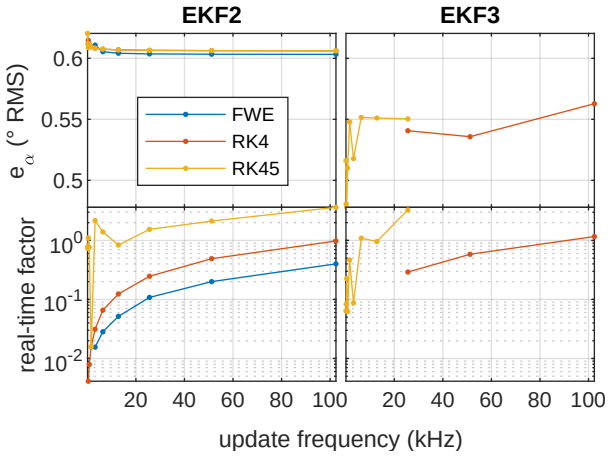

Figure 5.10.: Average angular error and real-time factor (ratio of computation time versus duration of the experiment) of the respective best-performing EKF2 and EKF3 operating at different sampling frequencies (Prechtl et al. 2024).

of estimation quality (measured in terms of the average error in the estimation of α, for simplicity) and computation speed (expressed as the ratio between computation time and duration of the experiment). We considered three numerical approximation methods, i.e., a forward Euler discretization (FWE), a 4th order Runge-Kutta method (RK4), and a 4th order Runge-Kutta method with adaptive step size regulation (RK45, allowed to take

substeps based on estimated local error) Leader 2022. Linear interpolation was used to generate the values of $\boldsymbol{l_{DE}}$ at intermediate points in time in which direct estimations were not available. For each fixed update frequency, the entries of diagonal matrices $\boldsymbol{S_f}$ and $\boldsymbol{S_h}$ were determined using numerical optimization to find the filter configuration that produces a minimal estimation error, as defined in Section 5.2.3 on the calibration dataset (*Sine*). Each optimized filter configuration was then evaluated on the full dataset (calibration data as well as the evaluation experiments, c.f. Figure 5.7). Diverging configurations and those with large average errors are omitted for visual clarity. In Figure 5.10, the upper plots show the average angular error and the bottom plots indicates the computation speed relative to the duration of the experiment, with values below one indicating performance suitable for real-time implementation.

For the EKF2 method (left-hand side of Figure 5.10), the RK4 scheme produced good estimates even at an update frequency of 400 Hz and slightly improves at larger frequencies. As expected, the FWE method starts to produce reasonable estimates only at 3.2 kHz and slightly improves with increasing frequency as well. Counterintuitively, it even outperforms the RK4 scheme. Possible explanations include compounding roundoff errors of the RK4 scheme manifesting at larger frequencies, or the appearance of non-optimal EKF configurations resulting from the nonlinear optimization procedure. Note that, for EKF2, both integration schemes are capable of producing fast (240× and 62× real-time speed for RK4 and FWE, respectively) and precise (average error of approximately 0.61°) estimates. The RK45 generally exhibits very similar quality of estimated states, but requires longer computation times as the RK4 scheme, due to the possibility of additional substeps. While this enables estimation at very low update frequencies, in a real-time setting one typically prefers a fixed step size scheme, owing to the fact that only a predetermined amount of time is available for state estimation.

In case of EKF3, the numerical optimization procedure did not produce a converging and reasonably precise FWE configuration. The main reason for this fact is the higher numerical stiffness due to the beam compression dynamics, which requires sufficiently small step sizes. In contrast, this issue is not present in EKF2 since (4.21) completely eliminates the stiff dynamics. This is illustrated by the stiffness ratio, which is computed as

$$s = \frac{\left|\overline{\lambda}\right|}{\left|\underline{\lambda}\right|}, \tag{5.11}$$

where $\overline{\lambda}$, $\underline{\lambda}$ are the largest and the smallest eigenvalues of $\boldsymbol{A}$ (cf. Equation (5.7)) according to the absolute value of their real components. As a result, the averaged stiffness ratio along a typical trajectory is improved from $s \approx 10600$ (EKF3) to $s \approx 70$ (EKF2). As a result, for EKF3 the RK4 scheme is usable starting from 25.6 kHz with a real-time factor of ≈ 0.29 (i.e. 3.4× faster than real time). At frequencies up to 25.6 kHz, the adaptive RK45 method can achieve stable and precise estimates with mixed results in terms of computation time and estimation quality, but fails at larger frequencies. Similarly to before, these results seem to reflect a trade-off between truncation error, favoring higher-order methods at low frequencies, and round-off errors, favoring methods with less arithmetic operations (i.e., lower-order methods) at higher frequencies. Generally, the performance of tuned configurations at different frequencies does not exhibit a discernible trend for the adaptive step size scheme. However, from an implementation perspective, we can simply pick the best performing configuration that still meets our constraints on computation

time (real-time factor smaller than one), such as the configuration tuned at an update frequency of 400 Hz with a real-time factor of 0.23.

Even though the presented evaluation was conducted on a powerful workstation (AMD Ryzen Threadripper PRO 5965WX 24C @3.8GHz, 256GB RAM), we expect actual performance requirements of a suitably chosen configuration to be lower in terms of working memory and computation speed (e.g., when the real-time factor is much smaller than one). Despite both EKF2 and EKF3 schemes appear similar in terms of accuracy (cf. Table 5.1), we conclude that the former is preferable for real-time implementation, since it works well with simpler, faster, and fixed-step discretization methods.

5.3. Summary: System-Level Self-Sensing

In this chapter, the feasibility of system-level self-sensing in a DEA-driven soft robot has been demonstrated. The resulting scheme is able to accurately estimate the configuration and generalized velocity of the underactuated T-Platform solely on the basis of voltage and current signals, measured during various actuation tasks. By comparing the self-sensing estimations with camera-based measurements, an average estimation error of 0.47° (EKF3), or 0.60° (EKF2), namely 1.6-2% of the actuation range, can be achieved. Remarkably, the algorithm is able to also reconstruct deformations caused by external loads, and not only high voltage actuation, with an accuracy of 0.79° (EKF3) and 0.91° (EKF2) respectively, thus proving its robustness. An in-depth investigation of discretization schemes and sampling times was conducted to optimize estimation performance and online computation times, proving that EKF2 is the most suitable scheme for real-time applications. To the author's knowledge, these results, which have been published in Prechtl et al. 2024, are the first practical demonstration of system-level self-sensing in multi-DoF DEA soft robots.

6. Summary and Future Work

This work aimed to bridge the gap between the fields of dielectric elastomer and soft robotics research. The two main research questions were:

1. Is it possible to build better soft robot models in a bottom-up sense, by starting at DE actuator models?

2. How can soft robots benefit from the DE self-sensing capability?

The pursuit of answers to these questions has led to fruitful research. In Chapter 3, a detailed model of rolled DE actuators was developed. The model considers actuator geometry and material properties while including descriptions of static and dynamic hysteresis that maintain thermodynamic consistency. In addition, its computational efficiency allows using it for advanced real-time control and sensing algorithms. The model proved effective not only for modeling, control and self-sensing of our T-Platform, but also saw adoption for modeling of various other RDEA mechanisms. Chapter 4 builds on these results to show that, indeed it is possible to leverage a good understanding of DE actuator physics for effective models of soft robots. The T-Platform model has been used to analyze and exploit the buckling operating mode of the structure, which represents a generalization of negative-stiffness DE biasing known from single-DoF DE actuators. Its physics-based derivation allows to understand the influence of design parameters, while it's efficient mathematical structure lets us design computationally efficient control and self-sensing algorithms. Finally, in Chapter 5 it was shown that by building on the previous chapters, it is possible to address a fundamental challenge in soft robotics: the problem of state estimation for non-rigid structures in the absence of traditional sensors. The derived system-level self-sensing scheme allows to accurately determine the position and orientation of the T-Platform even during external disturbances. Its real-time capability has been proven through numerical experiments.

In future works, it is planned to implement sensorless closed-loop control algorithms, which exploit the feedback from the proposed system-level self-sensing scheme to achieve closed-loop trajectory tracking. More extensive evaluation of the self-sensing method robustness, in particular its sensitivity to parameter variations and environmental effects, will also be systematically investigated. Furthermore, extending the results to three-dimensionsal DE-based robots will be a significant step towards practical implementations of this research.

Appendices

A. Calculation of the Hollow Cylinders Radii from the Unwound DE Membrane Dimensions

In order to accurately compare the RDEA model to the experiments, it is crucial to carefully calculate the model parameters based on the available measured dimensions and other known properties of the physical specimens. On the one hand, measuring the dimensions of the flat DE membranes prior to rolling is relatively simple. On the other hand, the model requires the knowledge of the radii of the different cylindrical regions, which might be hard, if not impossible, to measure exactly after the rolling process has been performed. This section provides a systematic procedure to estimate the radii of the RDEA, starting from the geometry of the unwound DE membrane. The key idea is based on accurately matching the volumes of active and inactive regions before and after the rolling.

The RDEA is manufactured by rolling a stack of two planar membranes with known dimensions (Kunze et al. 2021). Figure A.1 illustrates the resulting structure of a RDEA cross-section from a modeling perspective. The meaning of each parameter is reported in Table 3.1, and further visualized in Figure 3.12. Starting from the center and moving outwards radially, the spiral describing the wound DE membranes starts at a given inner radius R_i, and completes a certain amount of turns (described by the accumulated turning angle θ_{p1}) until the entire length L_{p1} of the inner electrode-free membrane is covered. Once this point is reached, the electrode-covered portion of the membrane stack begins. If a voltage is applied to the electrodes, an electric field will be induced in the region between them, as denoted by the arrows in Figure A.1a. Note that, in the first turn with electrodes, the electric field only appears in the outer half of the membrane stack, while in subsequent turns it also manifests itself in the inner half. This is due to the fact that the negative electrode of the current turn forms an additional pair with the positive electrode of the previous turn. This geometric feature produces a corresponding loss of active electrical volume, which is considered in the following calculations. In addition, the second passive layer of length L_{p2} produces a further electric field-free region on the outermost part of the roll, corresponding to angle θ_{p2} in Figure A.1a. Note how this figure does not depict the passive layers realistically (cf. Figure 3.3a), but solely serves to provide a geometric intuition for angles θ_{p1} and θ_{p2}.

A suitable kinematic model for describing the spiral geometry is the Archimedean spiral, which is characterized by having a constant separation between adjacent turns. The Archimedean spiral can be expressed in polar coordinates as

$$r(\theta) = r_0 + \frac{d}{2\pi}\theta \qquad \text{with} \quad r_0, d \in \mathbb{R}^+, \tag{A.1}$$

where the spiral radius r is given as a function of the turning angle θ, r_0 indicates the starting radius of the spiral, and d is the separation between adjacent turns. The circumference,

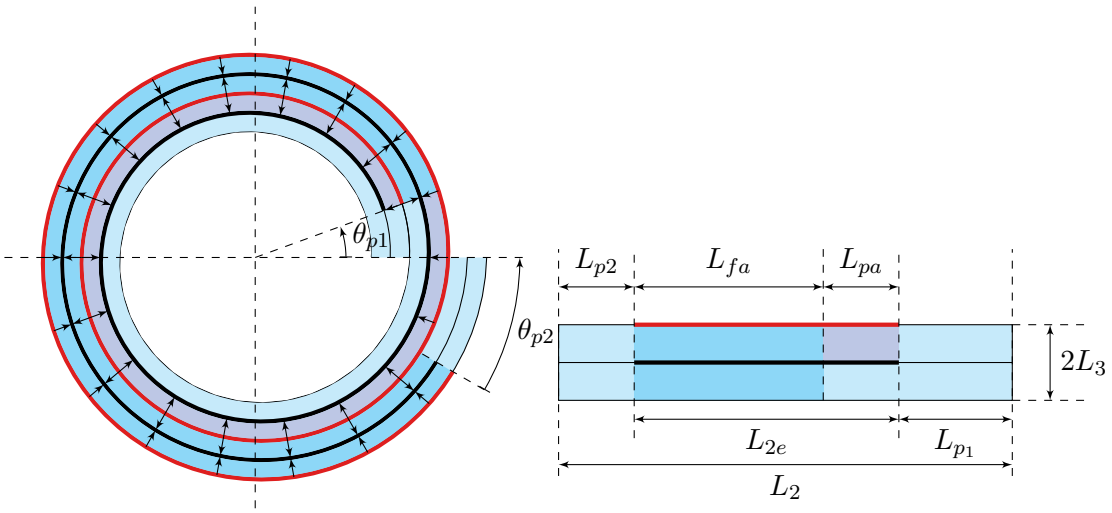

(a) Cross-Sectional view. (b) Virtually unrolled view.

Figure A.1.: Passive, partially active, and fully active regions of a RDEA (Prechtl et al. 2021a).

or length, of such a spiral is obtained by solving the following integral:

$$l_{\text{spiral}}(r_0, d, \theta) = \int_0^{\theta} \left\| \frac{d}{d\bar{\theta}} \left(r(\bar{\theta}) \begin{bmatrix} \cos\bar{\theta} \\ \sin\bar{\theta} \end{bmatrix} \right) \right\|^2 d\bar{\theta}. \tag{A.2}$$

Although an analytical solution is available for (A.2), in here it is omitted for conciseness. The total turning angle as a function of the spiral length is thus given as the inverse function of l_{spiral}:

$$\theta_{\text{spiral}}(r_0, d, l_{\text{spiral}}) = l^{-1}_{\text{spiral}}(r_0, d, l_{\text{spiral}}). \tag{A.3}$$

In practice, (A.3) is generally solved with numerical methods.

Based on equations (A.2)-(A.3), it is now possible to compute the geometric parameters appearing in Figure A.1b which are related to the losses in active volume caused by the passive regions (green areas in Figure A.1a). The turning angle θ_{p1} denotes the start of the electrically half-active region, consisting of the first turn with electrodes (purple area in Figure A.1a), and is computed as follows:

$$\theta_{p1} = \theta_{\text{spiral}}(R_i, 2L_3, L_{p1}). \tag{A.4}$$

To obtain (A.4), the following substitutions are made in (A.3): $r_0 = R_i$, $d = 2L_3$, and $l_{\text{spiral}} = L_{p1}$ (cf. Table 3.1). The electrically half-active region starts at θ_{p1} and ends after one full turn, which means at turning angle $\theta_{p1} + 2\pi$. We can thus calculate the length L_{pa} of the partially active region as:

$$L_{pa} = l_{spiral}(R_i, 2L_3, \theta_{p1} + 2\pi) - L_{p1}. \tag{A.5}$$

The remaining length L_{fa} of the fully active region (cyan area in Figure A.1a) is given as the difference between total electrode length and partially active length:

$$L_{fa} = L_{2e} - L_{pa}. \tag{A.6}$$

Finally, the length of the outer inactive region is given by:

$$L_{p2} = L_2 - L_{p1} - L_{2e}. \tag{A.7}$$

The above computed quantities can readily be used to compute the equivalent radii of the hollow cylinders describing the RDEA. The roll DEAs from Kunze et al. 2021 can be manufactured with a negligible inner hollow region, as confirmed by the microscope picture in Figure 3.3a, in which no meaningful inner hollow region can be seen. Based on this argument, we set

$$R_i = 0. \tag{A.8}$$

The three remaining radii are then computed by equating the volumes of the three hollow cylinders with the ones of the corresponding regions in the flat membrane state, according to Figure A.1:

$$\Omega_a = \pi(R_{ie}^2 - R_i^2)L_1 = L_1 L_3(2L_{p1} + L_{pa}), \tag{A.9}$$

$$\Omega_b = \pi(R_{oe}^2 - R_{ie}^2)L_1 = L_1 L_3(2L_{fa} + L_{pa}), \tag{A.10}$$

$$\Omega_c = \pi(R_o^2 - R_{oe}^2)L_1 = 2L_1 L_3 L_{p2}. \tag{A.11}$$

Note that the partially active volume is distributed equally between regions a and b. Solving (A.11) for the unknown radii, by considering positive solutions only, the following expressions are obtained:

$$R_{ie} = \sqrt{\frac{2L_3 L_{p1} + L_3 L_{pa}}{\pi}}, \tag{A.12}$$

$$R_{oe} = \sqrt{\frac{2L_3 L_{fa} + L_3 L_{pa}}{\pi} + R_{ie}^2}, \tag{A.13}$$

$$R_o = \sqrt{\frac{2L_3 L_{p2}}{\pi} + R_{oe}^2}. \tag{A.14}$$

B. T-Platform Identified Parameters

Table B.1.: System parameters for T-Platform Gen. A Prototype

a_1	15	mm	bottom-left horizontal mounting offset
a_2	15	mm	bottom-right horizontal mounting offset
b_1	−11.50	mm	bottom-left vertical mounting offset
b_2	−11.50	mm	bottom-right vertical mounting offset
v_1	0	mm	top-left vertical mounting offset
v_2	0	mm	top-right vertical mounting offset
w_1	18	mm	top-left horizontal mounting offset
w_2	18	mm	top-right horizontal mounting offset
l_b	92.64	mm	beam length
b_{top}	14.55	mm	beam upper mounting offset
l_{cr1}	13.54	mm	left DE length offset
l_{cr2}	13.71	mm	right DE length offset
A	14	mm^2	beam cross-sectional area
I	2.286 67	mm^4	beam second moment of area
E	1.34	GPa	beam Young's modulus
C_{1h}	220.14	kPa	left DE Yeoh coefficients
	−26.83		
	16.99		
C_{2h}	220.14	kPa	right DE Yeoh coefficients
	−26.83		
	16.99		
L_{1j}	68.20	mm	DE length
L_{3j}	47.62	µm	
R_{ij}	0	mm	DE inner radius
R_{oj}	1.54	mm	DE outer radius
α_{e1}	0.74		
η_b	0.72		
ϵ_0	8.85	$\mathrm{pF\,m^{-1}}$	vacuum permittivity
ϵ_r	2.80		DE relative permittivity
η_h	7.90	kPa s	DE damping coefficient
m_H	12	g	rigid top plate – mass
J_H	1.30	$\mathrm{kg\,mm^2}$	rigid top plate – moment of inertia
τ_y	−5	N	2-DoF model equivalent axial force
g	9.81	$\mathrm{N\,kg^{-1}}$	gravitational constant
d_x	0	$\mathrm{mN\,s\,m^{-1}}$	damping coefficient in x direction
d_y	0	$\mathrm{kN\,s\,m^{-1}}$	damping coefficient in y direction
d_α	0	$\mathrm{mN\,s\,rad^{-1}}$	damping coefficient in α direction

Table B.2.: System parameters for T-Platform Gen. B Prototype

a_1	5.25	mm	bottom-left horizontal mounting offset
a_2	5.25	mm	bottom-right horizontal mounting offset
b_1	7.02	mm	bottom-left vertical mounting offset
b_2	7.02	mm	bottom-right vertical mounting offset
v_1	8.16	mm	top-left vertical mounting offset
v_2	8.16	mm	top-right vertical mounting offset
w_1	9.65	mm	top-left horizontal mounting offset
w_2	9.65	mm	top-right horizontal mounting offset
l_b	53.32	mm	beam length
b_{top}	5	mm	beam upper mounting offset
l_{cr1}	2.74	mm	left DE length offset
l_{cr2}	2.05	mm	right DE length offset
A	1.88	mm^2	beam cross-sectional area
I	0.003 52	mm^4	beam second moment of area
E	210	GPa	beam Young's modulus
C_{1h}	380.43	kPa	left DE Yeoh coefficients
	84.16		
	−51.70		
C_{2h}	248.08	kPa	right DE Yeoh coefficients
	111.03		
	−0.02		
L_{1j}	25.61	mm	DE length
L_{3j}	50	µm	DE layer thickness
R_{ij}	0	mm	DE inner radius
R_{oj}	1.58	mm	DE outer radius
α_{e1}	0.78		
η_b	0.74		
ϵ_0	8.85	$pF\,m^{-1}$	vacuum permittivity
ϵ_r	2.80		DE relative permittivity
η_h	19.23	kPa s	DE damping coefficient
m_H	12	g	rigid top plate – mass
J_H	2.37	$kg\,mm^2$	rigid top plate – moment of inertia
τ_y	−13.37	N	2-DoF model equivalent axial force
g	9.81	$N\,kg^{-1}$	gravitational constant
d_x	0.10	$mN\,s\,m^{-1}$	damping coefficient in x direction
d_y	0.10	$kN\,s\,m^{-1}$	damping coefficient in y direction
d_α	0.10	$mN\,s\,rad^{-1}$	damping coefficient in α direction

Bibliography

Albu-Schaffer, A., O. Eiberger, M. Grebenstein, S. Haddadin, C. Ott, T. Wimbock, S. Wolf, and G. Hirzinger (Sept. 2008). "Soft Robotics". In: *IEEE Robotics & Automation Magazine* 15.3, pp. 20–30. ISSN: 1070-9932. DOI: 10.1109/MRA.2008.927979.

Arruda, E. M. and M. C. Boyce (Feb. 1993). "A Three-Dimensional Constitutive Model for the Large Stretch Behavior of Rubber Elastic Materials". In: *Journal of the Mechanics and Physics of Solids* 41.2, pp. 389–412. ISSN: 0022-5096. DOI: 10.1016/0022-5096(93)90013-6.

El-Atab, N., R. B. Mishra, F. Al-Modaf, L. Joharji, A. A. Alsharif, H. Alamoudi, M. Diaz, N. Qaiser, and M. M. Hussain (Oct. 2020). "Soft Actuators for Soft Robotic Applications: A Review". In: *Advanced Intelligent Systems* 2.10, p. 2000128. ISSN: 2640-4567, 2640-4567. DOI: 10.1002/aisy.202000128.

Awtar, S. and S. Sen (2010). "A Generalized Constraint Model for Two-Dimensional Beam Flexures: Nonlinear Strain Energy Formulation". In: *Journal of Mechanical Design* 132.8, p. 081009. ISSN: 10500472. DOI: 10.1115/1.4002006.

Baltes, M., J. Kunze, J. Prechtl, P. Motzki, and G. Rizzello (Apr. 2022a). "Soft Robotic Tentacle Arm Element Actuated by Rolled Dielectric Elastomer Artificial Muscles". In: *Electroactive Polymer Actuators and Devices (EAPAD) XXIV*. DOI: 10.1117/12.2612516.

Baltes, M., J. Kunze, J. Prechtl, S. Seelecke, and G. Rizzello (Sept. 2022b). "A Bi-Stable Soft Robotic Bendable Module Driven by Silicone Dielectric Elastomer Actuators: Design, Characterization, and Parameter Study". In: *Smart Materials and Structures* 31. © IOP Publishing. Reproduced with permission. All rights reserved. DOI: 10.1088/1361-665X/ac96df.

Berselli, G., R. Vertechy, G. Vassura, and V. Parenti-Castelli (2011). "Optimal Synthesis of Conically Shaped Dielectric Elastomer Linear Actuators: Design Methodology and Experimental Validation". In: 16.1, p. 13.

Böse, H. and J. Ehrlich (Mar. 2023). "Dielectric Elastomer Sensors with Advanced Designs and Their Applications". In: *Actuators* 12.3, p. 115. ISSN: 2076-0825. DOI: 10.3390/act12030115.

Burgner-Kahrs, J., D. C. Rucker, and H. Choset (Dec. 2015). "Continuum Robots for Medical Applications: A Survey". In: *IEEE Transactions on Robotics* 31.6, pp. 1261–1280. ISSN: 1552-3098, 1941-0468. DOI: 10.1109/TRO.2015.2489500.

Cao, J., W. Liang, J. Zhu, and Q. Ren (Oct. 2018). "Control of a Muscle-like Soft Actuator via a Bioinspired Approach". In: *Bioinspiration & Biomimetics* 13.6, p. 066005. ISSN: 1748-3190. DOI: 10.1088/1748-3190/aae1be.

Carpi, F. and D. De Rossi (June 2004). "Dielectric Elastomer Cylindrical Actuators: Electromechanical Modelling and Experimental Evaluation". In: *Materials Science and Engineering: C* 24.4, pp. 555–562. ISSN: 09284931. DOI: 10.1016/j.msec.2004.02.005.

Carpi, F., D. D. Rossi, R. Kornbluh, R. E. Pelrine, and P. Sommer-Larsen (Sept. 2011). *Dielectric Elastomers as Electromechanical Transducers: Fundamentals, Materials,*

Devices, Models and Applications of an Emerging Electroactive Polymer Technology. Elsevier. ISBN: 978-0-08-055772-4.

Chen, Y., H. Zhao, J. Mao, P. Chirarattananon, E. F. Helbling, N.-s. P. Hyun, D. R. Clarke, and R. J. Wood (Nov. 2019). "Controlled Flight of a Microrobot Powered by Soft Artificial Muscles". In: *Nature* 575.7782, pp. 324–329. ISSN: 1476-4687. DOI: 10.1038/s41586-019-1737-7.

Cianchetti, M., F. Renda, A. Licofonte, and C. Laschi (June 2012). "Sensorization of Continuum Soft Robots for Reconstructing Their Spatial Configuration". In: *2012 4th IEEE RAS & EMBS International Conference on Biomedical Robotics and Biomechatronics (BioRob)*. Rome, Italy: IEEE, pp. 634–639. ISBN: 978-1-4577-1200-5 978-1-4577-1199-2 978-1-4577-1198-5. DOI: 10.1109/BioRob.2012.6290788.

Cosserat, E. (and F. (Cosserat (1909). "Théorie des corps déformables". In: *Librairie Scientifique A. Hermann et Fils*.

De Tommasi, D., G. Puglisi, and G. Zurlo (Nov. 2014). "Hysteresis in Electroactive Polymers". In: *European Journal of Mechanics - A/Solids* 48, pp. 16–22. ISSN: 09977538. DOI: 10.1016/j.euromechsol.2014.05.011.

Della Santina, C., M. G. Catalano, and A. Bicchi (2020). "Soft Robots". In: *Encyclopedia of Robotics*. Ed. by M. H. Ang, O. Khatib, and B. Siciliano. Berlin, Heidelberg: Springer, pp. 1–15. ISBN: 978-3-642-41610-1. DOI: 10.1007/978-3-642-41610-1_146-2.

Della Santina, C., C. Duriez, and D. Rus (June 2023). "Model-Based Control of Soft Robots: A Survey of the State of the Art and Open Challenges". In: *IEEE Control Systems Magazine* 43.3, pp. 30–65. ISSN: 1941-000X. DOI: 10.1109/MCS.2023.3253419.

Dou, W., G. Zhong, J. Cao, Z. Shi, B. Peng, and L. Jiang (2021). "Soft Robotic Manipulators: Designs, Actuation, Stiffness Tuning, and Sensing". In: *Advanced Materials Technologies* 6.9, p. 2100018. ISSN: 2365-709X. DOI: 10.1002/admt.202100018.

Follador, M., A. T. Conn, and J. Rossiter (June 2015). "Bistable Minimum Energy Structures (BiMES) for Binary Robotics". In: *Smart Materials and Structures* 24.6, p. 065037. ISSN: 0964-1726, 1361-665X. DOI: 10.1088/0964-1726/24/6/065037.

Follador, M., A. T. Conn, B. Mazzolai, and J. Rossiter (Oct. 2014). "Active-Elastic Bistable Minimum Energy Structures". In: *Applied Physics Letters* 105.14, p. 141903. ISSN: 0003-6951. DOI: 10.1063/1.4898142.

Foo, K., S. Cai, A. Koh, S. Bauer, and Z. Suo (Feb. 2012). "Model of Dissipative Dielectric Elastomers". In: *Journal of Applied Physics* 111, p. 034102. DOI: 10.1063/1.3680878.

Gent, A. N. (Mar. 1996). "A New Constitutive Relation for Rubber". In: *Rubber Chemistry and Technology* 69.1, pp. 59–61. ISSN: 0035-9475. DOI: 10.5254/1.3538357.

Gisby, T. A., B. M. O'Brien, and I. A. Anderson (May 2013). "Self Sensing Feedback for Dielectric Elastomer Actuators". In: *Applied Physics Letters* 102.19, p. 193703. ISSN: 0003-6951. DOI: 10.1063/1.4805352.

Gratz-Kelly, S., M. Cerino, D. Philippi, D. Göttel, S. Nalbach, J. Hubertus, G. Schultes, J. Heppe, and P. Motzki (Dec. 2024). "Multifunctional Sensor Array for User Interaction Based on Dielectric Elastomers with Sputtered Metal Electrodes". In: *Materials* 17.23, p. 5993. DOI: 10.3390/ma17235993.

Gratz-Kelly, S., G. Rizzello, M. Fontana, S. Seelecke, and G. Moretti (Aug. 2022). "A Multi-Mode, Multi-Frequency Dielectric Elastomer Actuator". In: *Advanced Functional Materials* 32.34, p. 2201889. ISSN: 1616-301X, 1616-3028. DOI: 10.1002/adfm.202201889.

Guo, Y., L. Liu, Y. Liu, and J. Leng (2021). "Review of Dielectric Elastomer Actuators and Their Applications in Soft Robots". In: *Advanced Intelligent Systems* 3.10, p. 2000282. ISSN: 2640-4567. DOI: 10.1002/aisy.202000282.

Gupta, U., L. Qin, Y. Wang, H. Godaba, and J. Zhu (Oct. 2019). "Soft Robots Based on Dielectric Elastomer Actuators: A Review". In: *Smart Materials and Structures* 28.10, p. 103002. ISSN: 0964-1726, 1361-665X. DOI: 10.1088/1361-665X/ab3a77.

Harsch, J., S. Sailer, and S. R. Eugster (2023). "A Total Lagrangian, Objective and Intrinsically Locking-Free Petrov–Galerkin SE(3) Cosserat Rod Finite Element Formulation". In: *International Journal for Numerical Methods in Engineering* 124.13, pp. 2965–2994. ISSN: 1097-0207. DOI: 10.1002/nme.7236.

Hau, S., G. Rizzello, and S. Seelecke (Sept. 2018). "A Novel Dielectric Elastomer Membrane Actuator Concept for High-Force Applications". In: *Extreme Mechanics Letters* 23, pp. 24–28. ISSN: 2352-4316. DOI: 10.1016/j.eml.2018.07.002.

He, T., X. Zhao, and Z. Suo (Oct. 2009). "Dielectric Elastomer Membranes Undergoing Inhomogeneous Deformation". In: *Journal of Applied Physics* 106.8, p. 083522. ISSN: 0021-8979. DOI: 10.1063/1.3253322.

Heikkila, J. and O. Silven (1997). "A Four-Step Camera Calibration Procedure with Implicit Image Correction". In: *Proceedings of IEEE Computer Society Conference on Computer Vision and Pattern Recognition*. San Juan, Puerto Rico: IEEE Comput. Soc, pp. 1106–1112. ISBN: 978-0-8186-7822-6. DOI: 10.1109/CVPR.1997.609468.

Heim, J. R., I. Polyakov, A. Zarrabi, and O. Hui (Feb. 2009). "Electroactive Polymer Transducers Biased for Increased Output". US7492076B2.

Hodgins, M., A. York, and S. Seelecke (Aug. 2013). "Experimental Comparison of Bias Elements for Out-of-Plane DEAP Actuator System". In: *Smart Materials and Structures* 22.9, p. 094016. ISSN: 0964-1726. DOI: 10.1088/0964-1726/22/9/094016.

Hodgins, M. (2016). "Design of Diaphragm Dielectric Elastomer Actuators (DEAs) and Experimental Characterization Techniques". In: DOI: http://dx.doi.org/10.22028/D291-23206.

Hoffstadt, T., M. Griese, and J. Maas (Sept. 2014). "Online Identification Algorithms for Integrated Dielectric Electroactive Polymer Sensors and Self-Sensing Concepts". In: *Smart Materials and Structures* 23.10, p. 104007. ISSN: 0964-1726. DOI: 10.1088/0964-1726/23/10/104007.

Huang, P., J. Wu, P. Zhang, Y. Wang, and C.-Y. Su (Feb. 2022). "Dynamic Modeling and Tracking Control for Dielectric Elastomer Actuator With a Model Predictive Controller". In: *IEEE Transactions on Industrial Electronics* 69.2, pp. 1819–1828. ISSN: 1557-9948. DOI: 10.1109/TIE.2021.3063976.

Hubertus, J. (2022). "Metallische konforme Elektroden für dielektrische Elastomeraktoren und -sensoren". doctoralThesis. Saarländische Universitäts- und Landesbibliothek. DOI: 10.22028/D291-38533.

Imamura, H., K. Kadooka, and M. Taya (May 2017). "A Variable Stiffness Dielectric Elastomer Actuator Based on Electrostatic Chucking". In: *Soft Matter* 13.18, pp. 3440–3448. ISSN: 1744-6848. DOI: 10.1039/C7SM00546F.

Ivan, I. A., M. Rakotondrabe, P. Lutz, and N. Chaillet (Dec. 2009a). "Current Integration Force and Displacement Self-Sensing Method for Cantilevered Piezoelectric Actuators". In: *Review of Scientific Instruments* 80.12, p. 126103. ISSN: 0034-6748. DOI: 10.1063/1.3244040.

Ivan, I. A., M. Rakotondrabe, P. Lutz, and N. Chaillet (June 2009b). "Quasistatic Displacement Self-Sensing Method for Cantilevered Piezoelectric Actuators". In: *Review of Scientific Instruments* 80.6, p. 065102. ISSN: 0034-6748. DOI: 10.1063/1.3142486.

Jones, R. W. and R. Sarban (July 2012). "Inverse Grey-Box Model-Based Control of a Dielectric Elastomer Actuator". In: *Smart Materials and Structures* 21.7, p. 075019. ISSN: 0964-1726, 1361-665X. DOI: 10.1088/0964-1726/21/7/075019.

Jung, K., K. J. Kim, and H. R. Choi (May 2008). "A Self-Sensing Dielectric Elastomer Actuator". In: *Sensors and Actuators A: Physical* 143.2, pp. 343–351. ISSN: 0924-4247. DOI: 10.1016/j.sna.2007.10.076.

Kofod, G. and Forskningscenter Risø (2001). "Dielectric Elastomer Actuators: Ph. D. Thesis". PhD thesis. Roskilde: Risø National Laboratory : Available from: Risø National Laboratory, Information Service Department. ISBN: 9788755029248.

Kovacs, G., P. Lochmatter, and M. Wissler (Mar. 2007). "An Arm Wrestling Robot Driven by Dielectric Elastomer Actuators". In: *Smart Materials and Structures* 16.2, S306–S317. ISSN: 0964-1726. DOI: 10.1088/0964-1726/16/2/S16.

Kunze, J., G. Soleti, D. Bruch, P. Motzki, S. Nalbach, S. Seelecke, and G. Rizzello (May 2024). "Development and Experimental Evaluation of a Compact 3D Bending Module Actuated by Rolled Dielectric Elastomer Actuators". In: *Electroactive Polymer Actuators and Devices (EAPAD) XXVI*. Vol. 12945. SPIE, pp. 70–78. DOI: 10.1117/12.3010129.

Kunze, J., J. Prechtl, D. Bruch, B. Fasolt, S. Nalbach, P. Motzki, S. Seelecke, and G. Rizzello (Mar. 2021). "Design, Manufacturing, and Characterization of Thin, Core-Free, Rolled Dielectric Elastomer Actuators". In: *Actuators* 10, p. 69. DOI: 10.3390/act10040069.

Kunze, J., J. Prechtl, D. Bruch, S. Nalbach, P. Motzki, S. Seelecke, and G. Rizzello (Apr. 2020). "Design and Fabrication of Silicone-Based Dielectric Elastomer Rolled Actuators for Soft Robotic Applications". In: *Electroactive Polymer Actuators and Devices (EAPAD) XXII*. Vol. 11375. International Society for Optics and Photonics, p. 113752D. DOI: 10.1117/12.2558444.

Leader, J. J. (Apr. 2022). *Numerical Analysis and Scientific Computation*. 2nd ed. New York: Chapman and Hall/CRC. ISBN: 978-1-00-304227-3. DOI: 10.1201/9781003042273.

Lewis, F. L., L. Xie, and D. Popa (2008). *Optimal and Robust Estimation: With an Introduction to Stochastic Control Theory*. 2nd ed. Boca Raton: CRC Press. ISBN: 978-1-4200-0829-6.

Li, J., L. Liu, Y. Liu, and J. Leng (Feb. 2019). "Dielectric Elastomer Spring-Roll Bending Actuators: Applications in Soft Robotics and Design". In: *Soft Robotics* 6.1, pp. 69–81. ISSN: 2169-5172, 2169-5180. DOI: 10.1089/soro.2018.0037.

Li, Z., Z. Li, H. Xu, X. Zhang, and C.-Y. Su (Feb. 2023). "Development of a Butterfly Fractional-Order Backlash-Like Hysteresis Model for Dielectric Elastomer Actuators". In: *IEEE Transactions on Industrial Electronics* 70.2, pp. 1794–1801. ISSN: 1557-9948. DOI: 10.1109/TIE.2022.3163553.

Lin, Z., Z. Wang, W. Zhao, Y. Xu, X. Wang, T. Zhang, Z. Sun, L. Lin, and Z. Peng (2023). "Recent Advances in Perceptive Intelligence for Soft Robotics". In: *Advanced Intelligent Systems* 5.5, p. 2200329. ISSN: 2640-4567. DOI: 10.1002/aisy.202200329.

Lion, A. (Mar. 1997). "A Physically Based Method to Represent the Thermo-Mechanical Behaviour of Elastomers". In: *Acta Mechanica* 123.1-4, pp. 1–25. ISSN: 0001-5970, 1619-6937. DOI: 10.1007/BF01178397.

Liu, Z., Z. Cai, H. Peng, X. Zhang, and Z. Wu (Feb. 2023). "Morphology and Tension Perception of Cable-Driven Continuum Robots". In: *IEEE/ASME Transactions on Mechatronics* 28.1, pp. 314–325. ISSN: 1941-014X. DOI: 10.1109/TMECH.2022.3198093.

Loew, P., G. Rizzello, and S. Seelecke (Dec. 2018). "A Novel Biasing Mechanism for Circular Out-of-Plane Dielectric Actuators Based on Permanent Magnets". In: *Mechatronics* 56, pp. 48–57. ISSN: 09574158. DOI: 10.1016/j.mechatronics.2018.10.005.

Lu, T., C. Ma, and T. Wang (July 2020). "Mechanics of Dielectric Elastomer Structures: A Review". In: *Extreme Mechanics Letters* 38, p. 100752. ISSN: 2352-4316. DOI: 10.1016/j.eml.2020.100752.

Lucas, B. D. and T. Kanade (1981). "An Iterative Image Registration Technique with an Application to Stereo Vision". In: *International Joint Conference on Artificial Intelligence*. Vancouver, British Columbia, pp. 674–679.

Lunni, D., G. Giordano, E. Sinibaldi, M. Cianchetti, and B. Mazzolai (Apr. 2018). "Shape Estimation Based on Kalman Filtering: Towards Fully Soft Proprioception". In: *2018 IEEE International Conference on Soft Robotics (RoboSoft)*, pp. 541–546. DOI: 10.1109/ROBOSOFT.2018.8405382.

Marois, G., A. Bélanger, and W. Lutz (Apr. 2020). "Population Aging, Migration, and Productivity in Europe". In: *Proceedings of the National Academy of Sciences* 117.14, pp. 7690–7695. DOI: 10.1073/pnas.1918988117.

Masoud, A. E. and J. Maas (Mar. 2022). "Energy-Based Nonlinear Dynamical Modeling of Dielectric Elastomer Transducer Systems Suspended by Elastic Structures". In: *Acta Mechanica*. ISSN: 1619-6937. DOI: 10.1007/s00707-022-03151-4.

Massenio, P., J. Prechtl, D. Naso, and G. Rizzello (July 2022). "Nonlinear Optimal Control of a Soft Robotic Structure Actuated by Dielectric Elastomer Artificial Muscles". In: DOI: 10.1109/AIM52237.2022.9863262.

MathWorks (Feb. 2024). *Calibrate a Single or Stereo Camera - MATLAB*. (Visited on 02/20/2024).

Melly, S. K., L. Liu, Y. Liu, and J. Leng (Sept. 2021). "A Review on Material Models for Isotropic Hyperelasticity". In: *International Journal of Mechanical System Dynamics* 1.1, pp. 71–88. ISSN: 2767-1399, 2767-1402. DOI: 10.1002/msd2.12013.

Mertens, J., O. Cabuk, and J. Maas (Apr. 2022). "Modeling and Experimentally Parameterizing Approach of the Viscoelastic Material Behavior of DE-based Transducer Materials". In: *Electroactive Polymer Actuators and Devices (EAPAD) XXIV*. Ed. by J. D. Madden, I. A. Anderson, and H. R. Shea. Long Beach, United States: SPIE, p. 77. ISBN: 978-1-5106-4959-0 978-1-5106-4960-6. DOI: 10.1117/12.2613368.

Mooney, M. (Sept. 1940). "A Theory of Large Elastic Deformation". In: *Journal of Applied Physics* 11, pp. 582–592. ISSN: 0021-8979. DOI: 10.1063/1.1712836.

Nalbach, S., R. M. Banda, S. Croce, G. Rizzello, D. Naso, and S. Seelecke (2020). "Modeling and Design Optimization of a Rotational Soft Robotic System Driven by Double Cone Dielectric Elastomer Actuators". In: *Frontiers in Robotics and AI* 6. ISSN: 2296-9144. DOI: 10.3389/frobt.2019.00150.

Nelles, O. (2001). *Nonlinear System Identification*. Berlin, Heidelberg: Springer Berlin Heidelberg. ISBN: 978-3-642-08674-8 978-3-662-04323-3. DOI: 10.1007/978-3-662-04323-3.

Nguyen, C. T., H. Phung, P. T. Hoang, T. D. Nguyen, H. Jung, H. Moon, J. C. Koo, and H. R. Choi (Sept. 2017). "A Novel Bioinspired Hexapod Robot Developed by

Soft Dielectric Elastomer Actuators". In: *2017 IEEE/RSJ International Conference on Intelligent Robots and Systems (IROS)*, pp. 6233–6238. DOI: 10.1109/IROS.2017.8206526.

Nguyen, T., J. Li, L. Sun, D. Tran, and F. Xuan (July 2021). "Viscoelasticity Modeling of Dielectric Elastomers by Kelvin Voigt-Generalized Maxwell Model". In: *Polymers* 13.13, p. 2203. ISSN: 2073-4360. DOI: 10.3390/polym13132203.

Ni, N., L. Zhang, N. Ni, and L. Zhang (Aug. 2017). "Dielectric Elastomer Sensors". In: *Elastomers*. IntechOpen. ISBN: 978-953-51-3488-6. DOI: 10.5772/intechopen.68995.

O'Brien, B., J. Thode, I. Anderson, E. Calius, E. Haemmerle, and S. Xie (Apr. 2007). "Integrated Extension Sensor Based on Resistance and Voltage Measurement for a Dielectric Elastomer". In: *The 14th International Symposium on: Smart Structures and Materials & Nondestructive Evaluation and Health Monitoring*. Ed. by Y. Bar-Cohen. San Diego, California, p. 652415. DOI: 10.1117/12.715823.

Ogden, R. W. (Jan. 1997). *Non-Linear Elastic Deformations*. Courier Corporation. ISBN: 978-0-486-69648-5.

Pei, Q., M. Rosenthal, S. Stanford, H. Prahlad, and R. Pelrine (Sept. 2004). "Multiple-Degrees-of-Freedom Electroelastomer Roll Actuators". In: *Smart Materials and Structures* 13.5, N86–N92. ISSN: 0964-1726. DOI: 10.1088/0964-1726/13/5/N03.

Pelrine, R., J. Eckerle, and S. Chiba (Oct. 1992). "Review of Artificial Muscle Approaches". In: *Third International Symposium on Micro Machine and Human Science*. Nagoya, Japan, pp. 14–16.

Pelrine, R. E., R. D. Kornbluh, and J. P. Joseph (Jan. 1998). "Electrostriction of Polymer Dielectrics with Compliant Electrodes as a Means of Actuation". In: *Sensors and Actuators A: Physical* 64.1, pp. 77–85. ISSN: 09244247. DOI: 10.1016/S0924-4247(97)01657-9.

Prechtl, J., J. Kunze, G. Moretti, D. Bruch, S. Seelecke, and G. Rizzello (Nov. 2021a). "Modeling and Experimental Validation of Thin, Tightly Rolled Dielectric Elastomer Actuators". In: *Smart Materials and Structures* 31.1. © IOP Publishing. Reproduced with permission. All rights reserved., p. 015008. ISSN: 0964-1726. DOI: 10.1088/1361-665X/ac34be.

Prechtl, J., M. Baltes, K. Flaßkamp, and G. Rizzello (Mar. 2024). "Sensorless Proprioception in Multi-DoF Dielectric Elastomer Soft Robots via System-Level Self-Sensing". In: *IEEE/ASME Transactions on Mechatronics*. DOI: 10.1109/TMECH.2024.3375923.

Prechtl, J., M. Baltes, J. Kunze, S. Seelecke, and G. Rizzello (July 2022). "Towards Sensorless Configuration Estimation in Multi-DoF Soft Robotic Structures Driven by Rolled Dielectric Elastomer Actuators". In: *2022 IEEE/ASME International Conference on Advanced Intelligent Mechatronics (AIM)*. Sapporo, Japan: IEEE Press, pp. 1152–1158. DOI: 10.1109/AIM52237.2022.9863250.

Prechtl, J., J. Kunze, D. Bruch, S. Seelecke, and G. Rizzello (Apr. 2021b). "Bistable Actuation in Multi-DoF Soft Robotic Modules Driven by Rolled Dielectric Elastomer Actuators". In: *2021 IEEE 4th International Conference on Soft Robotics (RoboSoft)*, pp. 82–89. DOI: 10.1109/RoboSoft51838.2021.9479246.

Prechtl, J., J. Kunze, S. Nalbach, S. Seelecke, and G. Rizzello (Apr. 2020). "Soft Robotic Module Actuated by Silicone-Based Rolled Dielectric Elastomer Actuators: Modeling and Simulation". In: *Electroactive Polymer Actuators and Devices (EAPAD) XXII*. Vol. 11375. International Society for Optics and Photonics, p. 113752C. DOI: 10.1117/12.2557736.

Prechtl, J., J. Kunze, S. Seelecke, and G. Rizzello (Feb. 2021c). "Soft Robotic Module Actuated by Silicone-Based Rolled Dielectric Elastomer Actuators - Modeling and Simulation". In: *ACTUATOR; International Conference and Exhibition on New Actuator Systems and Applications 2021*, pp. 1–4.

Prechtl, J., F. Scherf, J. Kunze, K. Flaßkamp, and G. Rizzello (Mar. 2023). "An Energy-Based Model for Both Rate-Dependent and Rate-Independent Hysteretic Effects in Uniaxially-Loaded Dielectric Elastomer Actuators". In: *Electroactive Polymer Actuators and Devices (EAPAD) XXV*. DOI: 10.1117/12.2657685.

Preechayasomboon, P. and E. Rombokas (Feb. 2021). "Sensuator: A Hybrid Sensor–Actuator Approach to Soft Robotic Proprioception Using Recurrent Neural Networks". In: *Actuators* 10.2, p. 30. ISSN: 2076-0825. DOI: 10.3390/act10020030.

Pustina, P., C. Della Santina, F. Boyer, A. De Luca, and F. Renda (June 2023). *On the Collocated Form with Input Decoupling of Lagrangian Systems*. arXiv: 2306.07258 [physics].

Rajamani, A., M. D. Grissom, C. D. Rahn, and Q. Zhang (Feb. 2008). "Wound Roll Dielectric Elastomer Actuators: Fabrication, Analysis, and Experiments". In: *IEEE/ASME Transactions on Mechatronics* 13.1, pp. 117–124. ISSN: 1083-4435. DOI: 10.1109/TMECH.2008.915825.

Rakotondrabe, M. (June 2013). "Combining Self-Sensing with an Unkown-Input-Observer to Estimate the Displacement, the Force and the State in Piezoelectric Cantilevered Actuators". In: *2013 American Control Conference*. Washington, DC: IEEE, pp. 4516–4523. ISBN: 978-1-4799-0178-4 978-1-4799-0177-7 978-1-4799-0175-3. DOI: 10.1109/ACC.2013.6580535.

Rivlin, R. S. and E. K. Rideal (Oct. 1948a). "Large Elastic Deformations of Isotropic Materials IV. Further Developments of the General Theory". In: *Philosophical Transactions of the Royal Society of London. Series A, Mathematical and Physical Sciences* 241.835, pp. 379–397. DOI: 10.1098/rsta.1948.0024.

Rivlin, R. S. and G. I. Taylor (Jan. 1948b). "Large Elastic Deformations of Isotropic Materials. I. Fundamental Concepts". In: *Philosophical Transactions of the Royal Society of London. Series A, Mathematical and Physical Sciences* 240.822, pp. 459–490. DOI: 10.1098/rsta.1948.0002.

Rizzello, G. (Apr. 2016). "Modeling, Control and Self-Sensing of Dielectric Elastomer Actuators". PhD thesis.

— (May 2024). "Energy-Based Modeling of Rate-Independent Hysteresis and Viscoelastic Effects in Dielectric Elastomer Actuators". In: *Smart Materials and Structures* 33.5, p. 055027. ISSN: 0964-1726, 1361-665X. DOI: 10.1088/1361-665X/ad389f.

Rizzello, G., F. Fugaro, D. Naso, and S. Seelecke (Apr. 2018). "Simultaneous Self-Sensing of Displacement and Force for Soft Dielectric Elastomer Actuators". In: *IEEE Robotics and Automation Letters* 3, pp. 1230–1236. DOI: 10.1109/LRA.2018.2795016.

Rizzello, G., P. Loew, L. Agostini, M. Fontana, and S. Seelecke (2020a). "A Lumped Parameter Model for Strip-Shaped Dielectric Elastomer Membrane Transducers with Arbitrary Aspect Ratio". In: *Smart Materials and Structures*. ISSN: 0964-1726. DOI: 10.1088/1361-665X/abb09e.

Rizzello, G., D. Naso, A. York, and S. Seelecke (Feb. 2016). "Closed Loop Control of Dielectric Elastomer Actuators Based on Self-Sensing Displacement Feedback". In: *Smart Materials and Structures* 25, p. 035034. DOI: 10.1088/0964-1726/25/3/035034.

Rizzello, G., P. Serafino, D. Naso, and S. Seelecke (Feb. 2020b). "Towards Sensorless Soft Robotics: Self-Sensing Stiffness Control of Dielectric Elastomer Actuators". In: *IEEE Transactions on Robotics* 36.1, pp. 174–188. ISSN: 1941-0468. DOI: 10.1109/TRO.2019.2944592.

Röntgen, W. C. (1880). "Ueber Die Durch Electricität Bewirkten Form- Und Volumenänderungen von Dielectrischen Körpern". In: *Annalen der Physik* 247.13, pp. 771–786. ISSN: 1521-3889. DOI: 10.1002/andp.18802471304.

Rosset, S., B. M. O'Brien, T. Gisby, D. Xu, H. R. Shea, and I. A. Anderson (Sept. 2013). "Self-Sensing Dielectric Elastomer Actuators in Closed-Loop Operation". In: *Smart Materials and Structures* 22.10, p. 104018. ISSN: 0964-1726. DOI: 10.1088/0964-1726/22/10/104018.

Sause, R., K.-S. Lee, and J. Ricles (Nov. 2007). "Rate-Independent and Rate-Dependent Models for Hysteretic Behavior of Elastomers". In: *Journal of Engineering Mechanics-asce - J ENG MECH-ASCE* 133. DOI: 10.1061/(ASCE)0733-9399(2007)133:11(1162).

Shintake, J., V. Cacucciolo, H. Shea, and D. Floreano (June 2018). "Soft Biomimetic Fish Robot Made of Dielectric Elastomer Actuators". In: *Soft Robotics* 5.4, pp. 466–474. ISSN: 2169-5172. DOI: 10.1089/soro.2017.0062.

Shu, J., J. Wang, S. Lau, Y. Su, H. Heung, X. Shi, Z. Li, and R. K.-Y. Tong (Oct. 2022). "Soft Robots' Dynamic Posture Perception Using Kirigami-Inspired Flexible Sensors with Porous Structures and Long Short-Term Memory (LSTM) Neural Networks". In: *Sensors* 22, p. 7705. DOI: 10.3390/s22207705.

Soleti, G., P. R. Massenio, J. Kunze, and G. Rizzello (Apr. 2024). "Nonlinear Coordinate Transformation and Trajectory Tracking Control of an Underactuated Soft Robot Driven by Dielectric Elastomers". In: *2024 IEEE 7th International Conference on Soft Robotics (RoboSoft)*, pp. 228–234. DOI: 10.1109/RoboSoft60065.2024.10521952.

Soleti, G., J. Prechtl, P. R. Massenio, M. Baltes, and G. Rizzello (Jan. 2023). "Energy Based Control of a Bi-Stable and Underactuated Soft Robotic System Based on Dielectric Elastomer Actuators*". In: *IFAC-PapersOnLine*. 22nd IFAC World Congress 56.2, pp. 7796–7801. ISSN: 2405-8963. DOI: 10.1016/j.ifacol.2023.10.1153.

Strogatz, S. H. (1994). *Nonlinear Dynamics and Chaos: With Applications to Physics, Biology, Chemistry, and Engineering*. Studies in Nonlinearity. Reading, Mass: Addison-Wesley Pub. ISBN: 978-0-201-54344-5.

Suo, Z. (Dec. 2010). "Theory of Dielectric Elastomers". In: *Acta Mechanica Solida Sinica* 23.6, pp. 549–578. ISSN: 0894-9166. DOI: 10.1016/S0894-9166(11)60004-9.

Tomasi, C. and T. Kanade (Apr. 1991). *Detection and Tracking of Point Features*. Tech. rep. CMU-CS-91-132. Carnegie Mellon University.

Track Points in Video Using Kanade-Lucas-Tomasi (KLT) Algorithm - MATLAB (2024). https://www.mathworks.com/help/vision/ref/vision.pointtracker-system-object.html.

Verl, A., A. Albu-Schäffer, O. Brock, and A. Raatz, eds. (2015). *Soft Robotics: Transferring Theory to Application*. Berlin, Heidelberg: Springer Berlin Heidelberg. ISBN: 978-3-662-44505-1 978-3-662-44506-8. DOI: 10.1007/978-3-662-44506-8.

Wacker (2023). *Elastosil 2030 Films Catalogue*. https://www.wacker.com/h/medias/7091-EN.pdf.

Wang, H., M. Totaro, and L. Beccai (Sept. 2018). "Toward Perceptive Soft Robots: Progress and Challenges". In: *Advanced Science (Weinheim, Baden-Wurttemberg, Germany)* 5.9, p. 1800541. ISSN: 2198-3844. DOI: 10.1002/advs.201800541.

Wang, H.-m., J.-y. Zhu, and K.-b. Ye (Sept. 2009). "Simulation, Experimental Evaluation and Performance Improvement of a Cone Dielectric Elastomer Actuator". In: *Journal of Zhejiang University-SCIENCE A* 10.9, pp. 1296–1304. ISSN: 1862-1775. DOI: 10.1631/jzus.A0820666.

Wang, S. and Z. Sun (May 2023). "Hydrogel and Machine Learning for Soft Robots' Sensing and Signal Processing: A Review". In: *Journal of Bionic Engineering* 20.3, pp. 845–857. ISSN: 2543-2141. DOI: 10.1007/s42235-022-00320-y.

Wineman, A. S. and K. R. Rajagopal (June 2000). *Mechanical Response of Polymers: An Introduction*. Cambridge University Press. ISBN: 978-0-521-64409-9.

Wissler, M. and E. Mazza (Apr. 2005). "Modeling of a Pre-Strained Circular Actuator Made of Dielectric Elastomers". In: *Sensors and Actuators A: Physical* 120.1, pp. 184–192. ISSN: 0924-4247. DOI: 10.1016/j.sna.2004.11.015.

— (Aug. 2007). "Electromechanical Coupling in Dielectric Elastomer Actuators". In: *Sensors and Actuators A: Physical* 138.2, pp. 384–393. ISSN: 09244247. DOI: 10.1016/j.sna.2007.05.029.

Wissler, T. (2007). "Modeling Dielectric Elastomer Actuators". Doctoral Thesis. ETH Zurich. DOI: 10.3929/ethz-a-005406421.

Xing, Z., J. Zhang, D. McCoul, Y. Cui, L. Sun, and J. Zhao (Jan. 2020). "A Super-Lightweight and Soft Manipulator Driven by Dielectric Elastomers". In: *Soft Robotics*, soro.2018.0134. ISSN: 2169-5172, 2169-5180. DOI: 10.1089/soro.2018.0134.

Xu, H., Z. Li, Z. Li, and X. Zhang (Dec. 2021). "Modeling of Butterfly-Shaped Hysteresis in Dielectric Elastomer Actuators". In: *AIP Advances* 11.12, p. 125303. DOI: 10.1063/5.0069621.

Yang, Y., H. Zhu, J. Liu, H. Lu, Y. Ren, and M. Y. Wang (Jan. 2022). "A Proprioceptive Soft Robot Module Based on Supercoiled Polymer Artificial Muscle Strings". In: *Polymers* 14.11, p. 2265. ISSN: 2073-4360. DOI: 10.3390/polym14112265.

Yasa, O., Y. Toshimitsu, M. Y. Michelis, L. S. Jones, M. Filippi, T. Buchner, and R. K. Katzschmann (May 2023). "An Overview of Soft Robotics". In: *Annual Review of Control, Robotics, and Autonomous Systems* 6.1, pp. 1–29. ISSN: 2573-5144, 2573-5144. DOI: 10.1146/annurev-control-062322-100607.

Yeoh, O. H. (Nov. 1993). "Some Forms of the Strain Energy Function for Rubber". In: *Rubber Chemistry and Technology* 66.5, pp. 754–771. ISSN: 0035-9475. DOI: 10.5254/1.3538343.

Zhang, R., P. Lochmatter, A. Kunz, and G. Kovacs (Mar. 2006). "Spring Roll Dielectric Elastomer Actuators for a Portable Force Feedback Glove". In: *Smart Structures and Materials*. Ed. by Y. Bar-Cohen. San Diego, CA, 61681T. DOI: 10.1117/12.658524.

Zhang, Z. (Nov. 2000). "A Flexible New Technique for Camera Calibration". In: *IEEE Transactions on Pattern Analysis and Machine Intelligence* 22.11, pp. 1330–1334. ISSN: 01628828. DOI: 10.1109/34.888718.

Zhao, H., A. M. Hussain, M. Duduta, D. M. Vogt, R. J. Wood, and D. R. Clarke (Oct. 2018). "Compact Dielectric Elastomer Linear Actuators". In: *Advanced Functional Materials* 28.42, p. 1804328. ISSN: 1616301X. DOI: 10.1002/adfm.201804328.

Zhao, Q., J. Lai, K. Huang, X. Hu, and H. K. Chu (Oct. 2022). "Shape Estimation and Control of a Soft Continuum Robot Under External Payloads". In: *IEEE/ASME Transactions on Mechatronics* 27.5, pp. 2511–2522. ISSN: 1941-014X. DOI: 10.1109/TMECH.2021.3116970.

Zia, R. K. P., E. F. Redish, and S. R. McKay (July 2009). "Making Sense of the Legendre Transform". In: *American Journal of Physics* 77.7, pp. 614–622. ISSN: 0002-9505, 1943-2909. DOI: 10.1119/1.3119512.

Zou, J. and G. Gu (May 2018). "Modeling the Viscoelastic Hysteresis of Dielectric Elastomer Actuators with a Modified Rate-Dependent Prandtl–Ishlinskii Model". In: *Polymers* 10, p. 525. DOI: 10.3390/polym10050525.

List of Figures

List of Tables